Liquid crystalline structures of colloidal rods in mesoscopic droplets

Yunfei Jia

Liquid crystalline structures of colloidal rods in mesoscopic droplets

Inaugural–Dissertation

zur Erlangung des Doktorgrades
der Mathematisch–Naturwissenschaftlichen Fakultät
der Heinrich–Heine–Universität Düsseldorf

vorgelegt von

Yunfei Jia

aus Heilongjiang

Düsseldorf, Februar 2015

aus dem Institut für komplexe Systeme, weiche Materie (ICS-3)
des Forschungszentrums Jülich

Gedruckt mit der Genehmigung der
Mathematisch–Naturwissenschaftlichen Fakultät
der Heinrich–Heine–Universität Düsseldorf

Referent:	Prof. Dr. M.P.Lettinga
Koreferent:	Prof. Dr. S.U.Egelhaaf

Tag der mündlichen Prüfung: 5.2.2015

Abstract

The aim of this thesis is to investigate the effect of the confinement on the structure of the nematic director-field of colloidal liquid crystals. The experimental system we used in our study was a lyotropic liquid crystal consisting of rod-like viruses, the *fd* virus. Due to the length of the particle, which is of the order of 1 μm, individual particles can be imaged and confinements can be produced which approach the same length scale. We will use two approaches to produce the confinements: in chapter 4 we used fixed geometries made by soft lithography while in chapter 5 we produce deformable mesoscopic droplets with fixed volume. In the first part of the thesis we focus on producing stable droplets, which is a prerequisite for our final goal. In chapter 2, which is a technical chapter, we produced monodisperse mesoscopic water-in-oil droplets using microfluidic techniques. The kinetic stability of the emulsion droplets was quantitatively studied, which strongly relies on the effective molecular area occupied by a surfactant molecule. The mass transfer from the dispersed phase to the continuous phase takes place, in case of an excess of surfactant. We observed a budding phenomenon in which the small satellite droplets were formed at the droplet surface, thus further reducing the molecular area per surfactant. We selected the proper surfactant in combination with the carrier oil for later work in chapter 5. In chapter 3, we studied an alternative technique of stabilizing water-in-oil droplets using Pickering emulsions stabilized by fluorinated latex-core-shell particles. These particles, which are omniphobic, appeared to be extremely efficient in stabilizing water-in-oil droplets. We found that the efficiency of particle stabilization was due to a mechanism where only few particles were needed to form very stable bridges between two droplets, as we observed using confocal microscopy. An experimental phase diagram of three component emulsion system was presented, in which the transition of emulsion stability was mapped. Prior to the use of microfluidic droplets to study the three-dimensional structure of the nematic phase, we used in chapter 4 soft lithography to confine the nematic phase of *fd* virus in two-dimensional microchambers. The height of these chambers was a few microns, much smaller than the "cholesteric pitch" of the particles. We manufactured spindle-like chambers, mimicking in 2-D the shape of tactoids, the nematic droplets that form during isotropic-nematic phase separation. By systematically varying the size and the aspect ratio

of the chambers we found configurations predicted for 3-D tactoids as well as novel configurations. The transitions between the different states, as presented in diagram of states, were discussed in view of recent simulations. The director-field configuration of the chiral nematic liquid crystal (LC) phase in three-dimensional confinement was studied in chapter 5. We employed microfluidics to produce monodisperse droplets containing the nematic dispersions of *fd* virus surrounded by a carrier oil phase, and varied the size of the droplet as well as the concentration of the virus. We observed that the shape was always spherical in the size range studied, using polarization microscopy. We found a ring structure evolving in the polarization images with increasing size and concentration which we attribute to a cholesteric twist of the director-field. We confirm, using the single particle data, that indeed such a twist is present, however, in a non-trivial way. The twist is non-monotonous throughout the droplet and much less then observed in bulk. Thus, confinement suppresses the cholesteric twist. Chapter 6 is an exploratory chapter in which we demonstrate the potential of the *fd* droplets for future investigations. We show the reversible response of the droplets to the magnetic field and the distorted structure of merging droplets. Moreover, the droplet shrinkage due to the mass transfer can cause nematic-smectic phase transition as well as the deformation of the droplet.

Kurzfassung

Das Ziel dieser Arbeit ist es den Effekt räumlicher Begrenzung auf die Struktur des nematischen Direktor-Feldes kolloidaler Flüssigkristalle zu untersuchen. In unserer Arbeit haben wir einen lyotropischen Flüssigkristall, der aus Stäbchenartigen Viren, *fd*-Viren besteht, untersucht. Auf Grund der Länge der einzelnen Teilchen, die in der Größenordnung von $1\mu m$ liegt, können einzelne Teilchen visuell sichtbar gemacht und räumliche Begrenzungen erzeugt werden, die in der selben Größenordnung liegen. Wir benutzen zwei Ansätze, um die räumlichen Begrenzungen zu erzeugen: In Kapitel 4 verwenden wir feste Geometrien, die mit Hilfe von *soft litography* erzeugt werden. In Kapitel 5 hingegen erzeugen wir deformierbare mesoskopische Tröpfchen mit festem Volumen. Im ersten Teil dieser Arbeit fokussieren wir uns auf die Produktion stabiler Tröpfchen, welche eine Voraussetzung für unsere folgenden Untersuchungen sind. Im zweiten Kapitel, diskutieren wir die Technik, um monodisperse mesoskopische Wassertröpfchen in Öl mit Hilfe mikorofluidischer Geräte zu erzeugen. Die kinetische Stabilität der Emulsions-Tröpfchen, welche stark von der effektiven Ausdehnung des Moleküls abhängt, wurde quantitativ untersucht. Es findet ein Masse-Transfer von der dispersen-Phase zur kontinuierlichen statt, falls ein Übermaß an Tensid vorhanden ist. Wir beobachteten ein Knospungsphänomen bei dem die kleinen Satelliten-Tröpfchen an der Tröpfchenoberfläche gebildet werden, wodurch die Molekülfläche pro Tensid weiter reduziert wird. Schließlich haben wir das passende Tensid in Kombination mit dem Träger-Öl für die weitere Arbeit in Kapitel 5 ausgewählt. Im dritten Kapitel haben wir eine alternative Methode zur Stabilisierung von Wasser in Öl Tröpfchen untersucht. Dazu verwendeten wir Pickering-Emulsionen, die mit Hilfe von fluorierten Latex-Kern-Schale Teilchen stabilisiert wurden. Es hat sich herausgestellt, dass diese Teilchen, welche omniphob sind, extrem effizient darin sind, Wasser in Öl zu stabilisieren. Wir haben mit Hilfe konfokaler Mikroskopie herausgefunden, dass diese Effizienz in der Stabilisierung der Teilchen in einem Mechanismus begründet liegt, bei dem nur wenige Teilchen benötigt werden, um stabile Brücken zwischen den Tröpfchen zu bilden. Wir präsentieren ein experimentelles Phasendiagram einer drei-komponentigen Emulsion, bei dem der Übergang der Emulsions-Stabilität abgebildet wurde. Bevor wir zur Untersuchung der Struktur der nematischen Phase mikrofluidisch hergestellte Tröpfchen diskutieren, haben

wir in Kapitel 4 *soft litography* verwendet, um die nematische Phase von *fd*-Viren in zweidimensionalen Mikro-Kammern einzuschließen. Diese Kammern waren wenige Mikrometer hoch und dementsprechend sehr viel kleiner als die "cholesterische Neigung"der Teilchen. Wir haben spindelartige Kammern produziert, um im zweidimensionalen die Form von *Tactoids*, den nematischen Tröpfchen, die sich während einem isotropisch-nematischen Phasenübergang formen, zu imitieren. Durch eine sythematische Variation der Größe sowie des Aspektverälntnisses konnten wir für dreidimensionale *Tactoids* vorhergesagte, aber auch neue Konfigurationen finden. Der Übergang zwischen den Unterschieldichen Zuständen, wie im Phasendiagram vorgestellt, wird im Zusammenhang mit neueren Simulationen diskutiert. Die Konfiguration des Direktor-Feldes der chiral nematischen Flüssiggkristall-Phase (LC) in dreidimensionaler räumlicher Beschränkung wurde in Kapitel 5 untersucht. Zur Produktion monodisperser Tröpfchen haben wir Mikrofluidik verwendet. Die Tröpfchen enthalten die nematische Dispersion der *fd*-Viren umschlossen von einer Träger Öl Phase. Sowohl die Größe der Tröpfchen als auch die Konzentration der Viren wurde variiert. Mit Hilfe von *polarization microscopy* konnten wir zeigen, dass die Form der Teilchen im untersuchten Größenbereich immer sphärisch war. Wir beobachteten in den Polarisationsbildern eine sich mit zunehmender Größe sowie Konzentration deutlicher herausbildende Ringstruktur, welche wir mit einem cholesterischen Twist des Direktor-Feldes assoziieren. Wir konnten auf Basis der Einzel-Teilchen Daten einen Twist verifizieren, wenn auch auf nicht triviale Weise. Der Twist findet nicht monoton innerhalb des Tröpfchens statt und ist viel schwächer als im *Bulk*. Dementsprechend unterdrückt räumliche Begrenzung den *cholesterischen Twist*. In Kapitel 6 diskutieren wir das große Potenzial der *fd*-Tröpfchen für zukünftige Forschungsvorhaben. Wir zeigen, dass die Tröpfchen reversibel auf magnetische Felder antworten, sowie dass die Struktur sich vereinigender Tröpfchen verzerrt wird. Zudem kann das Schrumpfen der Tröpfchen auf Grund des Massentransfers einen nematisch-smektischen Phasenübergang sowie die Deformation des Tröpfchens induzieren.

Contents

1 Introduction

Small particles of sizes in the range from sub- nm to μm range are often referred as *Colloids*, from the greek word 'glue'. The dispersions of colloids are considered as gas or liquid phases of colloids in the background of solvent. The solute-solute interactions in such solutions are mediated by the solvent on the basis of the van der Waals interactions. The motion of colloids are actually 'passive', in contrast to the self-propelling behaviors of small particles. Colloids in dispersion are driven by the collective effect of the kinetic bombardments with the solvent molecules. The Brownian motion of minute-sized matters were first experimentally quantified by J.B.Perrin [1], which supported the colloid-atom analogy. Colloids also enable optical observations to advantage, due to their accessible sizes. Colloids with shape anisotropy attract the interest back to a century ago, when the first founded virus, tobacco mosaic virus (TMV) was extracted and characterized to be with rod-like shape. They are still used nowadays as a remarkable rigid object for biology and colloidal science. The naturally existing materials with rod-like shapes often serves as a typical rod-like experimental system in the field of colloids, where the complexity of polydispersity can be avoided.

The self-organization of colloids in space is often described by the word 'crowding'. Therefore, the crowder sizes and packing fraction are mostly important parameters for systems with a finite volume. The packing of rods, contrast to spheres, depends also on the relative orientations of the long axis of the particle. Both orientational and positional ordering can be induced for particles with shape anisotropy, opposed to spherical systems which can only possess positional ordering. It is to be expected that the competition between ordering of rods and confinement will lead to interesting physics. A common example in cell biology is the crowding of filaments, including F-actin filaments, microtubules, and intermediate filaments in cytoskeleton. The presence of these ordered states of the filaments provides the shapes and

structures of the cells, assists cell migration and other activities. The sickle-cell anemia, for instance, is an unpleasant disease, which is caused by the abnormality of hemoglobin molecules in red-blood cells. The crowding of these abnormal hemoglobin mutants with rod-like shapes results in rigid, sickle-like shapes of red-blood cells. The crowding of colloids may result in ordering within the self-organized structures, which links to the features of *liquid crystal colloids*.

1.1 Liquid Crystals

The conceptually simplest particles are spherical particles with hard core interactions, which means that there interaction is infinite when they touch and zero when they don't. Dispersion of colloidal spheres with hard core interactions undergoes a phase transition from a liquid phase to a solid phase, where particle positions are fixed in a crystal lattice, at a fixed volume fraction of 49.4% [2]. There are, however, materials that undergo phase transitions to a state that displays some degree of ordering while the material still has liquid-like properties. Those materials posses symmetries and properties intermediated between those of a liquid and those of a crystal. They are called, for this reason, *liquid crystals (LCs)*, or 'mesomorphic phases'. The building blocks of LCs are named as *mesogens* [3]. The symmetries of the mesogens needs to be anisotropic in order to form these kind of phases, because anisotropic particles can display orientational ordering without any positional ordering. Moreover, because of the anisotropy of the particles, ordering can occur on different length scales in different directions. Two classes of LCs can be defined depending on the controlling parameters: the *thermotropic LCs* and *lyotropic LCs*. The phase behavior of *thermotropic LCs* is set by the temperature and thermotropic LCs are pure one component systems mostly consisting often of small rod-like or disc-like organic molecules. *Lyotropic liquid crystals* are dispersions of anisotropic mesogens for which the phase behavior is set by the concentration of the particles. The mesogens can be amphiphilic macromolecules, e.g. surfacetants and lipids, or colloidal particles with shape anisotropy, e.g.tobacco mosaic virus (TMV), precipitated metal oxides, DNA, and canbon nanotubes (CNTs). For ideal particle which have hard-core interactions the phase behavior is athermal and driven by entropy.

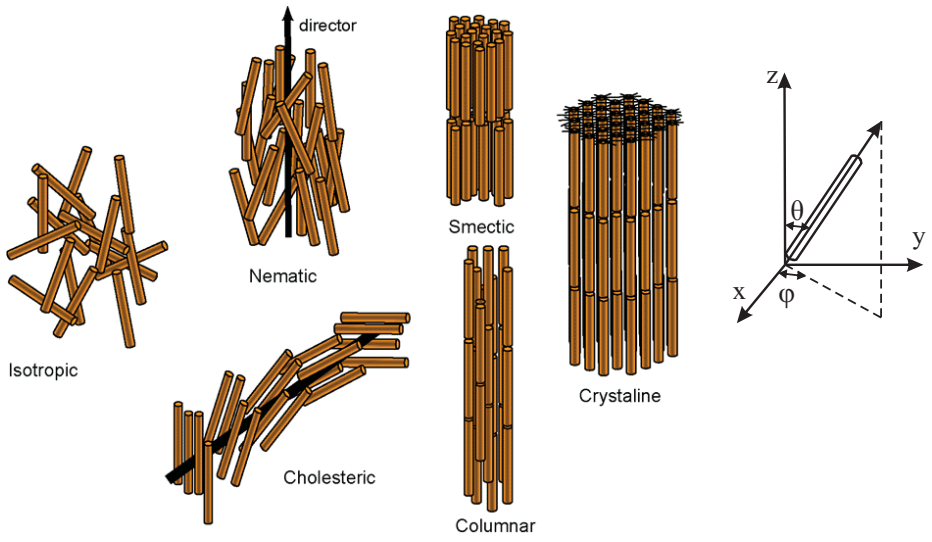

Figure 1.1: *Sketch of typical LC phases and the coordinate system defining the microscopic order parameter of nematic LC phases.*

1.1.1 Liquid Crystalline Phases

There is a plethora of phase transitions between the LC phases with increasing degree of ordering, starting from isotropic to the nematic, smectic, columnar and crystalline phase. The simplest conceivable anisotropic particles are rod-like particles, which displays all of these phases. The orientational order of rod-like particles can be described by considering the distribution of their long axis,given by the unit vector $\hat{\mathbf{u}}$, while the vector $\mathbf{r}$ describes the location of the center of mass. In the *isotropic* phase, the particles are randomly orientated with no positional order. The *nematics* phase displays long-range orientational order, but no positional order Fig.1.1. In the nematic LC phases $\hat{\mathbf{u}}$ has an average orientation along the 'director' described by the vector $\hat{\mathbf{n}}$. The polar angle between the unit vector $\hat{\mathbf{u}}$ and z-axis is defined as θ. The distribution function $f(\theta)$ gives the probability of finding rod-like particle at an angle θ around the director $\hat{\mathbf{n}}$. In order to quantify the degree of orientational ordering, often the *orientational order parameter S* is used, as first defined by Tsvetkov [4]. It describes the alignment of rod-like particles, as follows:

$$S = \frac{1}{2} < 3\cos^2\theta - 1 > . \tag{1.1}$$

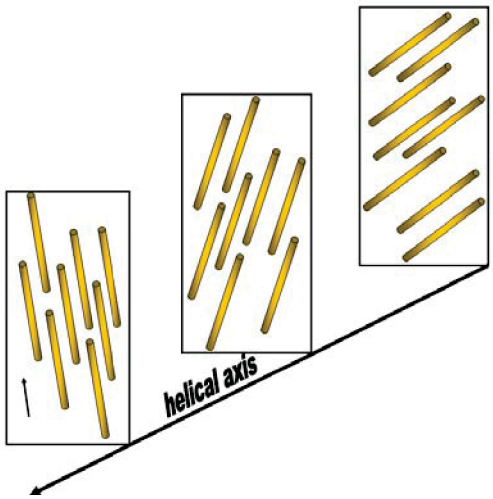

Figure 1.2: *Chiral nematic phase.*

For a random orientation distribution $< \cos^2\theta >= 1/3$ so that $S = 0$, while for perfectly oriented rods parallel aligned particles S equals 1.

The *chiral nematic*, or cholesteric, phase is a special case of nematic LCs. The physical properties of chiral nematic phase are similar to nematics, except that the director **n** twists as a helix within the LCs [5], see Fig.1.2. Although the twisting is of molecular origin and is due to the intermolecular forces between the asymmetric chiral molecules, it can be observed on length scales much bigger than the particles thickness. [6]. This leads to an energetically more favorable twisted alignment of mesogens. The chirality can be left-handed or right-handed, depending on the asymmetries of chiral molecules. A characteristic length, the *cholesteric pitch* p, is used to quantify the chiral nematic phase. p equals the distance over which the director **n** accomplishes a rotation of 360°. The natural wave vector of p_0 is defined as $q_0 = 2\pi/p_0$, according to de Gennes [3]. The periodic fingerprint structures of chiral nematic LC phases can be observed with polarizing microscopes. The typical length of the periodicity L refers to $p/2$, because the **n** and **-n** are not distinguishable.

In contrast to the nematic phase, the *smectic* phase does display position order Fig.1.1. In addition to the orientational order, it has one-dimensional positional order (in a two-dimensional layer), with evenly spaced layers. Based on subtle features, a few sub- states of smectic LC phase can be identified. For instance, *smectic A* has rods perpendicular to the layers, whereas *smectic C* possesses tilted arrangements. *Smectic B* has additional hexagonal crystalline order within the layers. The *columnar* phase has two-dimensional order and forms a two-dimensional arrays of liquid tubes [3]. It can be classified to hexagonal, rect-

angular, tetragonal, and oblique phases according to the two dimensional arrangements of mesogens Fig.1.1. The *crystals* have lattice structures expends to all directions.

In the following we will focus on the physics of the nematic phase. Although this is the phase with the lowest degree of ordering, still it displays many interesting phenomena from which we can learn basic principles of crowding.

1.1.2 Isotropic-Nematic Phase Transition

The Isotropi-Nematic (I-N) ordering of the mesogens with shape anisotropy was reasoned by Onsager considering rods with the simple hard-core excluded volume interactions in 1949 [7]. The rods are assumed impenetrable, therefore no overlapping occurs. He stated that the I-N transition was only driven by entropic reasons. For long rods, the translational entropy gain in the aligned N phase wins the orientational entropy lost. The I-N transition was predicted at a volume fraction of $\varphi_{I-N} = 4\frac{L}{d_{eff}}$ for stiff rods, where d_{eff} is the effective diameter of rods at the corresponding ionic strength. A phase coexistence between the isotropic and nematic phase for a specific range of concentration, which depends on the aspect ratio of the rods. Later theories are more expended by including the flexibility influence of the systems, with the $\varphi_{I-N} > 4\frac{L}{d_{eff}}$.

The birefringent structure that inspired Onsager of his seminal work showed spindle-like birefringent droplets on a black background with two cusps at the two poles of the droplet [8].Fig.1.3. These droplets, which are called tactoids, are formed by mesoscopic nematic rods in the two-phase region during I-N phase separation. The very first tactoids were reported for lyotropic inorganic systems, namely for dispersions of vanadium pentoxides and ferroxides in water [9] structures that inspired Onsager, however, were observed more then 10 years later for Tobacco Mosaic Virus by Bernal *et al* [8]. Much later, similar phenomena have been observed for a large variety of systems such as the sols of vanadium pentoxide in water [10],F-actin solution [11, 12], the carbon nanotubes [13].

Tactoids have the boundaries as circular arcs [10]. In order to understand the shape of the tactoids and of the structure of the nematic in general, it is a prerequisite to understand the forces needed to deform a nematic phase and to confine rods.

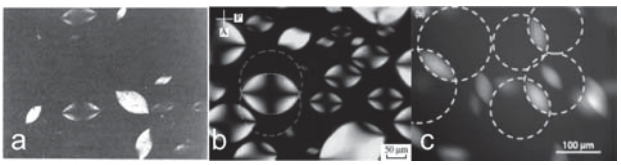

Figure 1.3: *Tactoids observed during I-N transition of different experimental systems. Nematic tactoids formed by TMV from infected sap (a), inorganic V_2O_5 (b), F-actin nematic tactoids in (c). [8, 10, 12].*

1.1.3 Deformations of the Director-Field

Ordered LC phases possess an orientational elasticity which connects to the deformation of director-field. They are sensitive to stimuli introduced by topology of the confinement, mechanical stresses, electric and magnetic fields, and so on. When a nematic is distorted by a perturbation, then a deformation of the nematic ordering may initially start with a local reorientation of the mesogens, which can transmit over a large region. This deformation will be opposed by the elasticity of the nematic. The deformation can be classified into three types, which are shown independently in Fig. 1.4. Likewise, the energy cost corresponding to the distortions of the director-field, i.e. the elastic contributions to free energy, is given by the Frank-Oseen elastic free energy F_e [3, 15]:

$$F_e = \frac{K_1}{2}(\nabla \cdot n)^2 + \frac{K_2}{2}(n \cdot \nabla \times n)^2 + \frac{K_3}{2}\big[n \times (\nabla \times n)\big]^2. \tag{1.2}$$

Here, K_1, K_2 and K_3 are the elastic constants representing the splay, twist and bend deformations respectively. These elastic constants are mostly assumed to be equal to a single value of K according to "one constant approximation". In practice, a resultant distorted director-field possesses usually a combination of the mentioned deformation types. There is an additional contribution of the twisted director-field, q_0, when considering a chiral nematic

$$F_e = \frac{K_1}{2}(\nabla \cdot n)^2 + \frac{K_2}{2}(n \cdot \nabla \times n + q_0)^2 + \frac{K_3}{2}\big[n \times (\nabla \times n)\big]^2 \tag{1.3}$$

Though it costs free energy to deform the nematic director-field, yet different types of defects(one-dimensional) and disclinations (often refers to two-dimensional line disclination) of the director-field spontaneously form. These lines boarder domains in which the director is locally well-defined. Under a polarization microscope they show as threads, see Fig.1.5, and hence the word nematic since $\nu\acute{\eta}\mu\alpha$ means "thread" in ancient greek. The reason that these

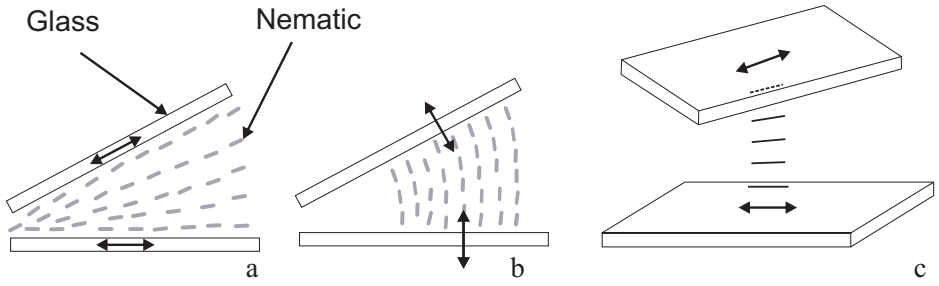

Figure 1.4: *Sketch of three classes of nematic deformations,* ***(a)*** *splay,* ***(b)*** *bend, and* ***(c)*** *twist between glass walls. The dashed lines in* ***(a)*** *and* ***(b)****refer to the nematic director-field. The twisted director-field forms a helical axis* ***n*** *perpendicular to the glass walls in* ***(c)****.*

domains form is that it causes the orientational entropy to increase globally, which reduces the free energy. Defects can be categorized by their strength, which is given by a sign and a magnitude, Fig. 1.5.(a). The heads of mesogens are marked in black color in order to distinguish from the tails. One may consider the rotation of mesogens following the director lines in an anti-clockwise manner, start from the no. 1 mesogens. The rotation of the mesogens themselves occurs, based on the distinguishable head-tail model, accompanied to the previous rotation. The sign is assigned positive according to the coupled rotation directions of the two, and negative if not. The magnitude of disclination is given by the ratio of the number of turns of the two [16]. The corresponding disclination strengths in Fig.1.5.(a) are $+1, +1/2, -1/2$, from left to right. Polarization images are always inconclusive in order to determine the nature of the disclinations, Fig.1.5.(b). Sketches of director-fields with disclinations correspond to the polarization microscope images in the upper and lower panel respectively. Here the red lines refer to the polarization direction of the placed polarizes [16]. Similar polarization images can be visualized from other disclinations.

There is a fourth type of deformations introduced by Oseen,Equ.1.4. This saddle-splay deformation describes the surface interactions (not listed in the Fig.1.4). It is usually ignored except for droplets with big surface-to-volume ratios, which turns out to be useful later [17, 18].

$$-K_{24}\nabla\cdot\Big[n\nabla\cdot n+n\times(\nabla\times n)\Big]\Big] \tag{1.4}$$

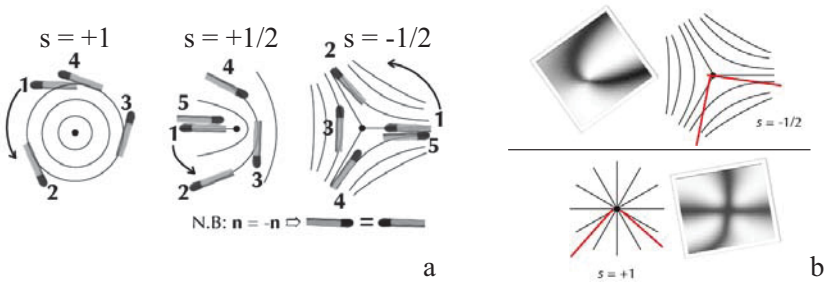

Figure 1.5: *The schematic interpretation of the defect strength calculation* ***(a)****. Sketches of defects and the corresponding example of polarizing microscope in the upper and lower panel respectively* ***(b)****. The black lines refer to the director lines and the red lines refer to the polarization direction of the placed polarizes [16]*

.

1.1.4 Anchoring Conditions

Anchoring conditions of the mesogens at the wall involve the local deformation of nematic director, in which the orientational order propagates to the bulk phase. This phenomena is always referred as "anchoring at the wall". A strong anchoring means the director prefers certain alignment when it comes close to the wall. A few typical "strong anchoring conditions" are shown in Fig.1.6, with director $\hat{n}$ parallel, perpendicular and tilted aligned at the wall accordingly.

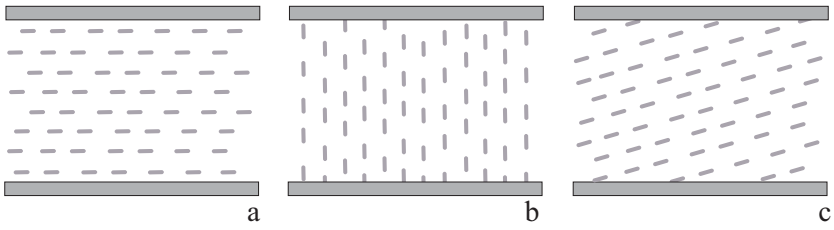

Figure 1.6: *Sketch of the nematic LCs anchoring on the wall:* ***(a)****. tangential,* ***(b)****. homeotropic and* ***(c)****. tilted.*

A dimensionless number ω is introduced to characterize the anchoring strength, where $\omega > 0$ if tangential anchoring is preferred and $-1 < \omega < 0$ if homeotropic anchoring is preferred [19]. A straight forward parameter, the '*extrapolation length, L*' is used to describe the resistance of the director-field distortion against the effect of wall anchoring [3], which is the distance from the 'imaginary surface', where the director would coincide with the director orientation in the bulk LC phase, to the real surface, see Equ.1.5.

$$L = \frac{K_1 - K_3}{\tau\omega} \tag{1.5}$$

The microscopic anchoring conditions are modeled by the energy term of the surface layer based on the orientational order of the mesogens [20]. The surface free energy F_s is given [15]:

$$F_s = \tau \int_A \mathrm{d}^2 r \left(1 + \omega(q \cdot n)^2\right) \tag{1.6}$$

with τ as the interfacial tension, A the surface area.

1.1.5 Influence of the Confinement

Confinements can be a useful tool to study the physical properties of LCs. Bulk elasticitic distortions imposed by anchoring conditions of LCs can be investigated. Anchoring conditions enforce deformations of director-fields when mesogens are close to the wall. Most nematic LCs possess strong anchoring conditions. The influences of the geometry and dimensionality of confinements are vital.

Spherical confinements were often employed to frustrate the LCs, as reported in both experimental and theoretical approaches by several groups [13, 17, 18, 21–26]. Mostly the spherical shape was chosen due to its highly symmetric structure and universal boundary conditions with certain curvature. The topological defects in LCs were also induced by other spatial confinement [27].

The spherical confinement imposes the deformation of the director-field of LCs, which is strongly bound to the anchoring conditions. The radial director-field configuration is known for LCs with perpendicular anchoring conditions, in which a point defect is located in the center of the confinement [28, 29]. For LCs with tangential wall anchoring, their director-fields vary for the interplay between bulk elastic property and the frustrated director filed, which results in interesting symmetries and topological defects of the director-field. The states of the nematic director-fields can be characterized by minimizing the sum of free energy, given by:

$$F = \int_V \mathrm{d}^3 r \Big[\frac{K_1}{2}(\nabla \cdot n)^2 + \frac{K_2}{2}(n \cdot \nabla \times n)^2 + \frac{K_3}{2}\big[n \times (\nabla \times n)\big]^2 \\ -K_{24}\nabla \cdot \big[n\nabla \cdot n + n \times (\nabla \times n)\big]\Big] + \tau \int_A \mathrm{d}^2 r \left(1 + \omega (q \cdot n)^2\right) \tag{1.7}$$

with V the droplet volume and A the surface area of the droplet.

The most prominent shapes in lyotropic LCs are tactoids, as introduced in the previous subsection. Prinsen and van der Schoot studied the shape and director-field transformation of tactoids varying the volume of the droplet, the anchoring strength, the interfacial tension and the elastic energy associated with the deformation of the director-field. Two types of director-field configurations were obtained, the bipolar and the homogeneous director-field. In the bipolar configuration, the director line follows smoothly the contour of the interface with bend deformation of the director-field. At one pole, it radiates outward and converges ultimately at the other diametrically opposed pole, with the two defect points sitting at the poles [30]. The homogeneous configurations possess with parallel director lines in the director of the main axis of the structures.

They identified the four regimes of droplets with spherical and spindle-like shapes from a homogeneous to a bipolar director-field by ruling out the role of twisted and the saddle-splay deformations. The crossover from a homogeneous to a bipolar director-field occurs if the surface anisotropy wins out from the elastic stiffness of the director-field, see Fig.1.7. These configurations are optimized by balancing of the minimum deformation of the director-field and a minimal interfacial area (Equ 1.7). The competition of these two parameters determines the eventual shape of the droplets. The dominate influence of the interfacial tension leads to a spherical large droplet and for the smaller droplet, an elongated shape is adopted to minimize the deformation.

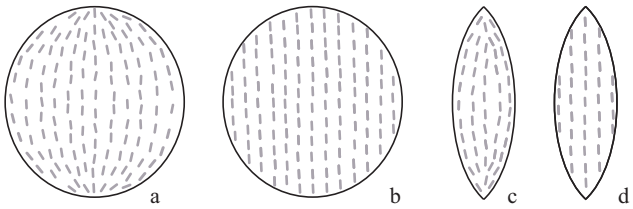

Figure 1.7: *Sketch of spherical and spindle-shaped droplets with homogeneous and bipolar director-field.* ***(a)****. Spherical droplet with bipolar director-field.* ***(b)****. Spherical droplet with homogeneous director-field.* ***(c)****. Spindle-like droplet with bipolar director-field.* ***(d)****. Spindle-like droplet with homogeneous director-field.*

They predicted a smooth crossing over of the director-field from a homogeneous (Fig. 1.7.**d**) to a bipolar configuration (Fig. 1.7 **c**), of the tactoids with increasing volume, by adding the contribution of the saddle-splay deformation (Equ.1.4). The speculation was that the two virtual point defects move in from infinity to the poles of the droplet with the infinite droplet volume [18], see Fig.1.8.

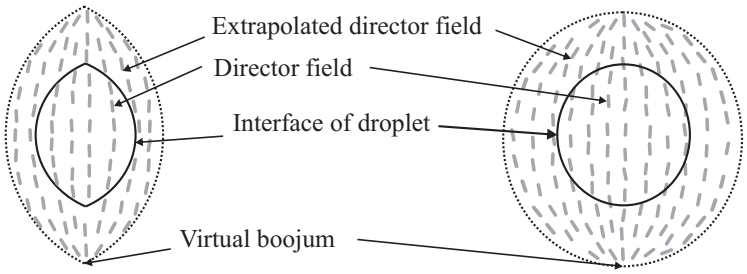

Figure 1.8: *Sketch of the shape and director-field of quasi bipolar nematic droplets with spherical and spindle-shape. Solid line: the contour of the droplet surface. The virtual director director-field converges in two point defects outside of the droplet. This figure is based on the work of Prinsen and van der Schoot, 2003 and 2004.*

The tactoidal shape, as the equilibrium shape of nematic droplets in the I-N phase transitions, is determined by three aspects: the surface tension, the anchoring condition, and the bulk elastic energy. The surface tension term tries to minimize the surface area; the anchoring condition determines the alignment of the rod-like particles at the boundary; and the bulk elastic energy avoids distortions of the nematic director-field.

1.2 Experimental System

To study the deformation of the director-fields by imposing spacial confinement, colloidal rods can be employed, which enable the possible optical observations at the single molecule level, and on the same time possess rich phase behaviors. *fd* viruses are typical biological monodisperse colloidal rods, which can be fluorescently labeled. *fd* virus and its mutant are semiflexible, and often used in the field of colloids to study lyotropic LCs. A *fd* virus is about 880 nm long and 6.6 nm thick, with aspect ratio of$\sim$ 100 (Fig.1.9d). The length scale of *fd* virus in $\sim 1\mu$m range makes the optical observations of LC phase transitions possible. The equilibrium phase behavior of *fd* virus is well-known [31–33]. The isotropic-nematic (I-N) phase transition of *fd* virus in equilibrium is well-understood on the basis of the Onsager theory. It undergoes a first order phase transition from isotropic to cholesteric LC phase.

Nematic(N) tactoids formed by *fd* virus were observed during I-N phase separation displaying both the spinodal decomposition and nucleation and growth, see Fig.1.9a-c,e [34].

Our work is motivated by the nematic tactoids formed by *fd* virus, where the system underwent nucleation and growth pathway, see Fig.1.9a-c. The elongated shape of tactoids and the merging of the tactoids were observed by confocal microscopy, which enable a 'zoom-in' of the tactaidal shape and the nematic director within the tactoids on the single molecule level, see Fig.1.9e.

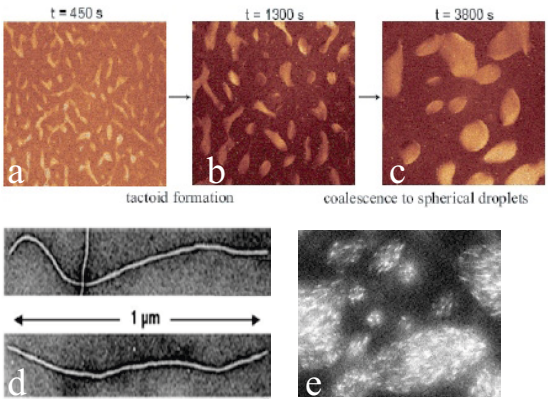

Figure 1.9: *The growth of nematic tactoids formed by fd virus during I-N phase separation from* ***(a)*** *to* ***(c)****. The electron micrograph of fd virus* ***(d)*** *and the confocal image of labeled fd virus in the tactoids* ***(b)****, which were observed in the process of the growth of the tactoids [34, 37].*

The morphology of the structures formed during I-N phase separation and the inspiring confocal microscope observations of *fd* virus suggest that the nematic director within tactoids might be under the influence of finite size effect, which is imposed by the tactoids. Even though tactoids are sensitive to mechanical perturbations, tactoids can settle back after the distortion of the order in the system, which is near the equilibrium metastable states [11].

The states of nematic director within tactoids are strongly connected to the anchoring conditions, which is tangential in the case of *fd* virus. Tactoids were observed experimentally with tangential anchoring condition along the arcs [10] by variation of polarization patterns of tactoids during their rotations, Fig.1.10a. The coalescence of tactoids leads to their gradually change towards spherical shape [34], Fig.1.10b. Tactoids might have a mirror symmetric nonchiral structure with the bipolar director-field. For instance, the merging of tactoids was observed when the neighboring tactoids share similar orientations of their mesogens at the contacted regions [10, 12, 34]. Otherwise the twisted orientation of rod-like particles can eas-

ily pin the interfacial region, which hinderds the coalescence. Tactoids with a homogeneous director-field was also reported, which were formed by CNTs [13], Fig.1.10d.

However, tactoids with chiral symmetry were also formed by achiral mesogens, where the crowding was supposed to drive the achiral-chiral transition by tuning the geometry of the tactoidal shape [25]. It is still an open question if the chiral symmetry is a consequence of chirality of the mesogens or the crowding effect in certain geometrical confinement.

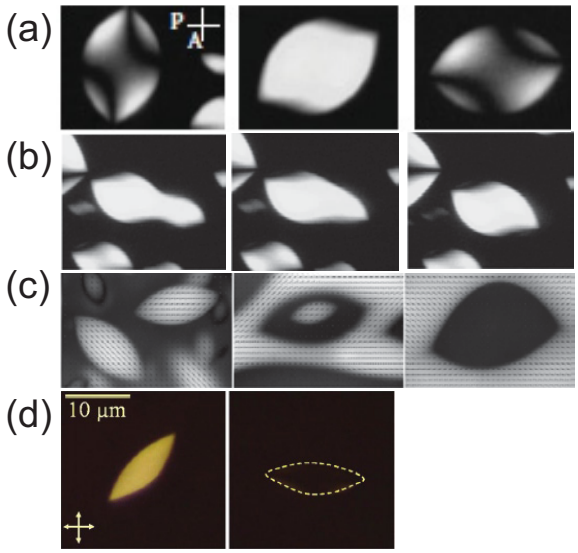

Figure 1.10: *Textures of tactoids formed in different experimental systems. Variation of textures of a F-action N tactoids during rotation between cross-polarizers* ***(a)****. The merging process of N tactoids such as* ***(a)*** *is presented in* ***(b)****. F-actin coexistence of N tactoids, N and I tactoids, and F-actin I tactoid in a N background, from left to right in* ***(c)****. The local alignment of F-actin are indicated by the line segments. Tactoids formed by CNTs with 'quasi-homogeneous' director-field* ***(d)*** *[10, 11, 13, 34].*

The practical issue of the studies on the basis of tactoids is the handling of the systems and the polydispersity of tactoids. We perform two approaches to attack this problem. One is to confine the nematic director in two-dimensional shallow microchambers by suppressing the chirality of fd virus in the third dimension. Since we fix the shape, enforcing the director-field to deal with shapes that are not encountered during the natural phase separation process, the frustrated nematic director because the shape of the microchambers are preset. The second approach is to address the complex three-dimensional problem by confining the fd virus in monodisperse droplets with tunable sizes. The interplay of the interfacial tension and bulk elastic deformation of the director-field is involved, by giving the strong tangential anchoring conditions. We study quantitatively the nematic director in both approaches by confocal fluo-

rescent microscope and polarization microscope because of the intrinsic nature of the nematic phase, namely the birefringence.

Birefringence is an optical effect occurs in anisotropic materials. It is caused by the variation of propagation of a light wave on its polarization and propagation direction. LCs are intrinsic birefringent materials because they have an axes of anisotropy. In uniaxial nematic LCs, the optical wave with arbitrary polarization breaks down into two orthogonal linear polarized waves: *ordinary* and *extraordinary* waves, with two corresponding refractive indices, n_o and n_e. The polarization direction of the ordinary wave is perpendicular to the axis of anisotropy, and that of the extraordinary wave is parallel to the axis of anisotropy. The velocity of the former one is independent of the propagation direction; the velocity of the later one depends on different propagation directions. The *birefringence* is given by $\Delta n = n_e - n_d$. The nematic order paramater S can be simply obtained based on the birefringence in dispersions of rod-like *fd* virus, which can be measured by a Berek compensator [38, 39].

$$\Delta n_{sat} S = \Delta n \tag{1.8}$$

with Δn_{sat} the saturation birefringence of perfectly aligned *fd*. The value $\Delta n_{sat}/\rho = 3.8 \times 10^{-5}$ ml/mg, was determined by x-ray diffraction, with ρ the concentration of *fd* in mg/ml [39]. The propagation of waves within optically anisotropic materials causes phase shifts $\Delta\varphi$ between the waves. The phase shift is proportional to the velocity difference and the travel distance of the waves.

$$\Delta\varphi = \frac{2\pi}{\lambda}(n_e - n_d)t \tag{1.9}$$

with λ, the wavelength of the incident light and t, the path length within the material. If a nematic LC sample is placed between crossed polarizer and analyzer and its optical axis has certain angles with the optical path ($\neq 0$ or 90°), some component of the ray can pass. The sample appears bright, which is often used to examine the ordering of the samples, Fig.1.3. When the white light is used as incident light, beautiful interference colors are displayed due to the wavelength dependence of the phase shift $\Delta\varphi$. The *optical path difference (OPD)* is given by $\mid (n_e - n_o) \mid t$, which is interchangeable with *retardation*. Optical plates with certain wavelength, reflected by the color, are designed to investigate the colorful textures of the birefringence, namely 'retarding plate'. This is realized by placing the plates between the

polarizer and the analyzer, which absorb the ray with the designed wavelength and therefore obtain, for instance, the phase changes and birefringence [40].

1.3 Emulsions

While mesoscopic tactoids are relatively exotic droplet-like structures that spontaneously form during phase separation of rod-like colloids, the most common phase separating structures are spherical droplets. Droplets of water-oil emulsions, or vise versa, are perhaps the most common example. Emulsions are involved in many aspects of our daily life due to their wide applications, from personal care to food. They are mostly composed of a dispersed liquid (dispersed phase), carrier liquid (continuous phase), and stabilizers or emulsifier. The dispersed phase and continuous phase are immiscible, and usually they are either oil or water (aquas system). Depending on the emulsification parameters, emulsions can be formed by dispersing water phase in oil phase (W/O) or oil phase in water phase (O/W).

Microemulsions are dispersions consisting of water, oil and surfactants, with droplet diameters varying from 1 to 100 nm. Mesoscopic mulsion with droplets' diameter close to the range of 10^{-3}m is commonly referred as macroemulsion or emulsion. The properties of these emulsions depend strongly on the length scale. Microemulsions are thermodynamically stable, forming either droplets or an bicontinuous phase. The formation of microemulsions is spontaneous and droplets do not coarsen over time. Mesoscopic emulsions, in contrast, are usually prepared by applying mechanical agitations to the system, e.g. stirring, ultrasonication, shaking, injection, microfluidics, stirring, vibration and so on.

A variety of stabilizer or emulsifier are applied to stabilize emulsions, e.g. solid particles, amphiphilic molecules, block co-polymers, and so on. The function of the stabilizer or emulsifier is not trivial. They should reduce substantially the interfacial tension between the dispersed phase and continuous phase in order to overcome the system-required energy barrier during the droplet formation. The work being used to create a new interface with an area of ΔA is important, which is given by

$$W = \sigma_i \Delta A \tag{1.10}$$

with σ_i, the *interfacial tension* between the liquid-liquid phase boundary. The interfacial tension can be reduced greatly by surfactants, therefore lowering the energy barrier of generating

the interfacial area. The most common examples in practices are surface active agents, called surfactants, see Fig. 1.11a. The systems undergo phase separation eventually, unless the non-zero interfacial tension σ_i is sufficiently low, for which the inherent nature of such emulsions is acknowledged. The system is just thermodynamically unstable in a long-term. Emulsions, however, can be kinetically stable in a short-term against some changes of their physical property, for instance, coalescence. The other role that the stabilizers play is to prevent the phase separation by forming effective interfacial barriers. The stabilizer can be, for example, solid particles (See Fig.1.11b) and non-ionic surfactants.

Stabilizers crowd at the liquid-liquid interfaces and form rigid steric barriers, which therefore prevent droplet coalescence. The type of emulsions stabilized by solid particles are named as "*Pickering emulsions*" after Pickering, who firstly performed systematic study of such emulsions. The solid particles accumulate irreversibly at the oil-water interface and form emulsions with the combination of steric hinderance and electrostatic repulsions, contrast to the surfactants stabilization mechanism, in which surfactants intend to adsorb at all the available surfaces and form micelles. The emulsions stabilized by solid particles are therefore inexpensive. However, the surface wettability of the solid particles are crucial for pickering emulsion formation and they should not have a tendency to form agglomerates. The coarsening of Pickering emulsions very often leads to sedimentation or creaming due to buoyancy. The efficiency of the solid particles can be improved by adjusting the amount of solid particles in the stabilization, for instance, the particle-bridging (will be introduced in chapter 3). Ostwarld ripening occurs susceptibly in pickering emulsions, which is an important sign of emulsion destabilization.

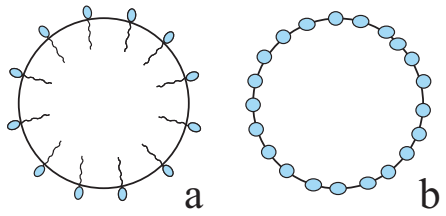

Figure 1.11: *Examples of emulsion stabilization mechanisms by:* ***(a)*** *amphiphilic molecules and* ***(b)*** *solid particles.*

The typical destabilization processes of emulsions are often discussed, which is particularly important to the kinetic stability or shelf-time of emulsions. A polydisperse emulsion system is shown in Fig.1.12. Regarding the stabilities of emulsions, one might concern the following questions: 1). the identities; 2). shapes; 3). volumes of droplets after destabilization. Fig.1.12.(a) refers to a perfectly stabilized emulsion with droplets evenly distributed in the carrier phase. Fig.1.12.(b). and (d). are similar in the sense that the identities of droplets are

not lost, the droplet go to the top or bottom of carrier phases due to their density difference with carrier phases. The shape and volume of the droplets are well preserved. In Fig.1.12.(c)., the droplets attach to each other and form local flocs. This is a result of van der Waals attraction, when the distances between droplets are not sufficient for counter repulsion. One common feature of Fig.1.12 (b), (c), and (e) is that the droplets come into contact with each other and the identities of droplets are preserved. These processes are often reversible by much less energy input comparing to the initial emulsification process.

Further ultimate states of emulsion systems are shown in Fig. 1.12.(e) coalescence, (f) Ostwald ripening, and (g) phase separation. The first example refers to the situation of droplets coarsening and lose their identities after the attachment of droplets. The direct consequence of coalescence is the formation of droplets with greater volume and therefore, less interfacial area. The *Ostwald ripening* is named for the mass transfer of the solute of disperse phase from smaller droplets to bigger droplets because of the Laplace pressure difference in the curvatures of the droplets. The speed of this process does not only depends on the solubility of dispersed phase in continuous phase but also the permeability of dispersed phase going through the surfactants layer. The sign of this destabilization process is the formation of larger droplets with relatively narrow distribution and the continuous growth of droplets.

Droplets break and the system goes through a phase separation in (g). The eventual phase separation is a clear sign for unstable emulsion systems. The interfacial area is minimized to decrease the interfacial potential. It is initiated by coalescence of attached droplets and probably driven by depletion interactions of surfactants, due to unbalanced osmotic pressures caused by the excess surfactant micelles. The thin film of surfactants at the contact regions rupture and the droplets merge into bigger droplets. The resultant emulsion has a broader size distribution of the droplets and this process is relatively rapid [41]. The stability of emulsion can be influenced by external factors, for instance, the ambient temperature, and pressure, and undesirable side-effects originated the nature of surfactants. The direct proof of emulsion destabilization down to the molecular-lever is not yet available.

In practical work, the boundary of defining kinetically stable emulsions lies in between the flocculation and the coalescence. Therefore, the criteria hung upon potential applications of emulsion systems.

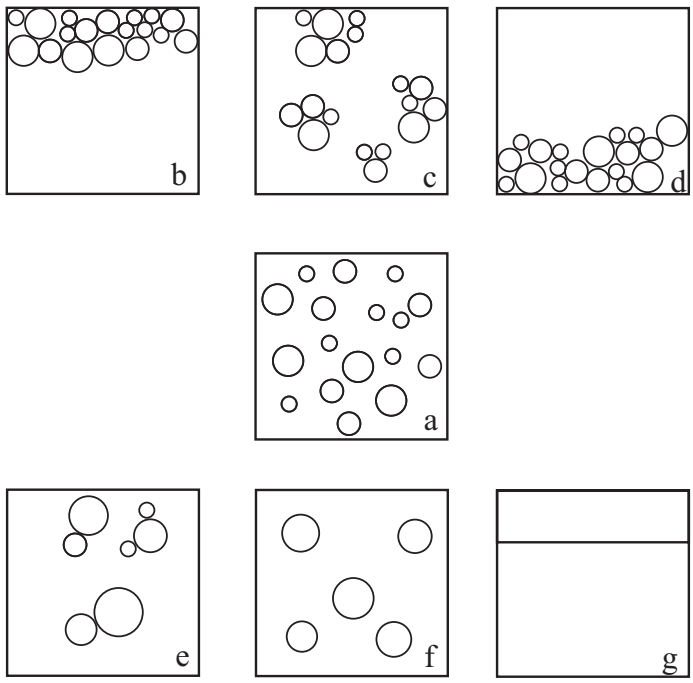

Figure 1.12: *Schematic representations of emulsion stabilization issues. (a) stable, (b) creaming, (c) flocculation, (d) sedimentation, (e) coalescence, (f) Ostwald ripening, and (g) phase separation.*

1.4 Scope of the Thesis

The aim of this thesis is to investigate the effect of confinement on the structure of the nematic director-field of colloidal liquid crystals with the rod-like shape, inspired by the mesoscopic nematic tactoids observed in the isotropic-nematic phase separation. The peculiar shape and internal structure of tactoids is determined by the competition of the interfacial tension, which prefers a spherical geometry, and Frank elasticity, which favors a straight director-field, and the anchoring conditions. We will use two approaches to produce the confinements: in chapter 4 we use fixed geometries made by soft lithography while in chapter 5 we produce deformable mesoscopic droplets with fixed volume. In the first part of the thesis we focus on producing stable droplets, which is a prerequisite for our final goal. In chapter 2, which is a technical chapter, we produced monodisperse mesoscopic water in oil droplets using microfluidic techniques. We study the kinetic stability of the emulsion droplets on the basis of the effective molecular area occupied by a surfactant molecule. We select the proper surfactant in combination with the carrier oil for later work in chapter 5.

In chapter 3 we choose another route. Instead of manipulating a water-oil droplet by struc-

turing the inside of the droplet, we modify the surface of the droplet by using newly developed colloids that are omniphobic, i.e. they avoid water as well as oil. We aim at improving the efficiency in solid particle stabilization.

In chapter 4 we confine the nematic phase in two-dimensional shallow chamber by suppressing the chirality of the chiral nematic LC phase in the third dimension. We study the frustration of the nematic director-field, which is enslaved by the anchoring conditions. The confinements are in circular and elongated spindle shapes with various aspect ratios to project the nematic director of the tactoidal shape of N LC tactoids appeared in the I-N phase separation in a two-dimensional simplified model.

In chapter 5 we study the director-field configuration of the chiral nematic liquid crystal (LC) phase in three-dimensional confinements. We employ microfluidics to produce monodisperse mesoscopic droplets containing the nematic dispersions of *fd* virus surrounded by a carrier oil phase, and vary the size of the droplet as well as the concentration of the virus. Here the competition between the minimization of the surface free energy and of the elastic free energy connected to the nematic is expected to result either in the deformation of the droplet or the deformation of the director-field. Chapter 6 is an exploratory chapter in which we demonstrate the potential of the *fd* droplets for future investigations.

2

Microfluidics and Droplet Generation

In this technical chapter, we produce monodisperse mesoscopic water in oil droplets using microfluidic techniques. We study phenomenologically the detachment of droplets at the junctions in the form of dripping and jetting. The kinetic stability of the emulsion droplets is quantitatively studied, which strongly relies on the effective molecular area occupied by a surfactant molecule. The mass transfer from the dispersed phase to the continuous phase takes place, in case of an excess of surfactant. We observe a budding phenomenon in which the small satellite droplets are formed at the droplet surface, thus further reducing the molecular area per surfactant. We selecte the proper surfactant in combination with the carrier oil for later work in chapter 5.

2.1 Introduction

Microfluidics is the science and technology of systems that process or manipulate small amounts (10^{-9} to 10^{-18} liters) of fluids, using channels with dimensions of tens to hundreds of micrometers and with typical flow rates of 1 μl/s [42]. The emergence of microfluidics over the past two decades is related with developments in lithographic techniques, which are used to produce these channels. The popularity of microfluidics is due to the broad range of applications.

First, basically any desired 2D shape can be produced in a fast and cheap way, using replica molding, where cross-linkable polymer is pored on a mold made by lithograph technique. A very well known polymer which is commonly used for this so called *soft* lithography, is poly(dimethylsiloxane) (PDMS) [43]. This features can be used to address fundamental phys-

ical issues, since many physical processes are affected when a system is confined to the micrometer length scale. At this length scale, for example, mass transport is generally dominated by viscous dissipation, and inertia effects are generally negligible [44]. For instance, in the macroscopic world fluids mix in a convective way, see for example how smoke coming out from a chimney mixes with air. In microfluidic channels, parallel streams will flow alongside with each other and the mixing happens as a result of diffusion of molecules across the fluid interface [44]. Micro-channels can also be designed such that any type of flow can be induced, including turbulent flow [45]. Turbulent flow can be used in a second important application of micro-fluidics, namely that chemical reactions on ultra small amounts of samples can be analyzed in so called micro-reactors [46–48]. Micro-channels are also used to develop analytical methods with greater throughput, higher sensitivity and resolution than conventional methods, as it is applied now for the high-throughput DNA sequencing and crystallization of membrane proteins [49–51]. There is a growing interest in the application of microfluidics for compartmentalization in droplets where the 'micrometric reactor' or 'confinement with variable dimension' can be produced [52, 53], especially in the field of soft matter. Here there is the fundamental interest of finite size effects, which set in when the contained particles, such as colloidal spheres or rods, approach the length scale of the confinements [54]. Moreover, microfluidics can be designed to accomplish complex emulsions, such as multi-emulsions [45, 55, 56]. Molecular nematic LC shells with various thickness were prepared in a microcapilary device to engineer defects within the LC shell with tangential anchoring conditions [57]. Similar study observed a transition of the LCs from the N to smectic-A phases via tuning the anchoring conditions and shell thickness [58].

In this thesis we make use of two of the main feature microfluidics, in both cases in combination with nematic dispersions of fd virus. In chapter 4 home-made PDMS-based chips are used to study the effect of confinement on the ordering of fd virus. Here we make use of flexibility of soft lithography with which different structure can be designed and produced. In chapter 5 and 6, we produce and study droplets with the same dispersion of nematic fd virus. For this study it is a prerequisite to make droplets that are *stable* and *tunable in size*, which is the aim of this chapter.

This chapter is organized as follows. First we introduce the technical experimental setup and the scenario of droplet generation based on the flow control. Then the flow rates of our Microfluidic system by determining a suitable working range of chamber pressures is calibrated in order to generate aqueous droplets with the diameter range of 10-300 μm. We afterwards present a few phenomena regarding the snapping off of aqueous droplets by the liquid pro-

files. Further we study of the stability of aqueous droplets and propose mechanisms of droplet destabilization considering the effective molecular area taken by each surfactant and the inherint nature of surfactants. In the end we discuss the stability of droplets and the useague of surfactants.

2.1.1 Microfluidic Chips and Flow Control

The model geometries of the microfluidic toolbox, such as the flow-focusing (X-junction) and T-junction, can be employed to produce monodisperse droplets and bubbles with variable size by adjusting the dimensions of model geometry. There are several types of microfluidic chips being used for the droplet generation, which are mainly equipped with T-junctions [59–61] and X-junctions [62]. Depending on different applications, the proper junction format should be chosen. For instance, the X-junction is able to provide more stable droplet formation at higher flow rates than the T-junction. The dimension of the junctions is varied to enable the generation of the droplets with proper sizes.

The production of tunable monodisperse droplets is performed by a controlled mechanical emulsification process of liquid fragmentation. A typical example of such process is shown in Fig. 2.1 with a couple of droplets marked in blue. First, the two fluids are pumped into two separate microchannels, where they form liquid columns. The liquid columns of both phases meet at an orifice, where the destabilisation of the liquid column from the dispersed phase (D-Phase) is a result of the shear introduced by the flow of continuous phase (C-Phase), see Fig. 2.1.(c)-(d). The growing liquid 'jet' or 'finger' of D-phase, which is connected to the orifice wall by a liquid bridge, obstructs the orifice and thus the flow of the continuous phase is hindered, Fig.2.1.(e). The resulting path for the continuous phase is reduced greatly and therefore the local dynamic stress in the continuous phase upstream of the droplet increases, which drives the thinning of the liquid neck after which the droplets will pinch off one after another in a controlled manner, Fig.2.1.(e) [63, 64].

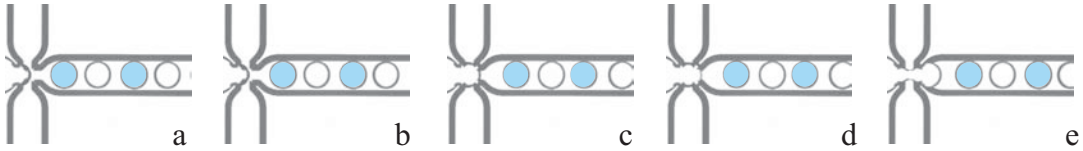

Figure 2.1: *Kinetics of monodisperse droplet production from real-time microscope observations.*

The competition between the local viscous stress and the dynamic pressure field surround-

ing the emerging droplet depends on a set vital parameters: the fluid viscosities μ_d and μ_c; densities ρ_d and ρ_c; the applied pressures P_d and P_c; the volumetric flow rates Q_d and Q_c; the channel width w_d and w_c; the interfacial tension σ; the interface curvature κ; channel depth h. Here the subscripts 'd' and 'c' refer the dispersed phase and the continuous phase. The viscous stress can be estimated by the product $\mu_c G$. Here G is a characteristic rate of strain that is proportional to the volumetric flow rate Q_c and a geometric factor S. The volumetric flow rate $\varphi = Q_c/Q_d$ is often used to control the formation of droplets. The capillary number Ca describes the relative effect of viscous forces vs the surface tension at the liquid-liquid, or liquid-gas interface, which is given by

$$Ca = \frac{\mu_c G a}{\sigma} \propto \frac{\mu_c Q_c S a}{\sigma} \tag{2.1}$$

with the characteristic size of the finger before approaching the orifice a. The typical Ca accessible for syringe pump ranges from $Ca \sim 10^{-3} - 10^{1}$.

The droplet detachment scenario differs for the different microfluidic geometries used for droplet generation, which is introduced in the previous section. This includes the most common examples of dripping, in which droplet detachment takes place in the vicinity of the orifice, (Fig.2.1) and jetting, in which droplets are pinched off from an extended thread downstream of the orifice (Fig.2.6). The transition of the droplets pinching off scenario from dripping to jetting has been studied in various geometries, in which capillary numbers and viscous stress were found crucial [64–67]. The critical flow velocity Q_c in this process is set by the flow velocity of the D-Phase Q_d, the viscosity of D-Phase μ_d and interfacial tensions σ [65–67]. Dripping of the droplets takes place at low capillary numbers and jetting happens at high capillary numbers, when the 'liquid finger' does not block the walls of the channel, therefore the 'liquid-finger' is not confined. In the X-junction geometry, this transition was characterized as the transition from an absolute to a convective instability. The viscous carrier fluid phase allows a stable thread to form before the pinching off of the droplets takes place [67]. Droplet sizes cannot be predicted for most of the applications, because the phenomenological models proposed were usually bound to the specific channel geometries [64].

One of the controlling parameters of droplet detachment is the surface properties of the microfluidic channel, because the continuous phase shall preferentially wet the wall. The snapping off of the droplets is more difficult if the wetting of the liquid 'jet' or 'finger' on the channel takes place, as the liquid 'jet' or 'finger' influences indirectly the thinning of the liquid neck. Hydrophobic microfluidic channel surface are therefore used to fabricate water-

in-oil (W/O) emulsions, and vise verse. Hydrophobicity can be achieved by siliconized or fluorophilic channel surfaces to avoid sticking of the dispersed aqueous phase and to facilitate the droplet detachment. In addition, it provides a lubricate path for the droplets afterwards.

Droplet generation process relies on the continuous flows of the C- and the D- phases, which can be provided by external sources. Pressure-driven pumps are often employed to ensure pulseless flows, which is advantageous compared to the step-wise driven model provided by most syringe-based pumps. The droplet size distribution of the droplets generated by the later case has experimentally been examined by us and the flow rate fluctuation of the step-wise driven syringe pump was found to be responsible for the polydispersity. With the pressure-driven-based microfluidic devices, the pressure can be precisely controlled by the operation mode. The flow rate of samples can be transformed by the precise input chamber pressure (gauge pressure) with fixed resistance of the system parameters. The flow rates of fluidic sample in the pressure driven pumps do not only depend on the selected pressure but also the resistance of the system, for instance, the inlet and outlet tubing inner diameter (ID), the length of the tubing, additional flow resisters, droplet generator channel geometry and dimensions, the viscosity of the fluid sample itself and so on. The interchangeble flow resistors in the flow system enable the application with very low viscosity fluids and the strong contrast in viscosities of the C-Phase and the D-Phase. The droplet formation can also be operated at very low flow rates with proper flow resistors and it provides the possibility of real-time optical observations. A proper transformation of the chamber pressure to the flow rate is needed, in order to have a control over the droplet generation process. For this purpose, a calibration of the flow system is usually performed.

2.1.2 Stability of Aqueous Droplets

Besides the detachment of the droplets, the stability of the droplets within or outside of the channel is considered to be a complicated issue involving coalescence, spreading of droplets on the substrate, consistency of the droplet volume, the general shelf time and so on, as introduced in chapter 1. Surfactants are generally employed for this purpose in the field of microfluidics. In our application, single- or multi- component surfactants are needed to stabilize droplets with diameter in the range of 10-300 μm in a wide range of temperature and under biological conditions. They should facilitate stability of micro-droplets since the formation of spherical droplets. In the case of droplets with internal structures, the role of stabilizer is vital due to the elasticity of the internal structures. Fluorinated surfactants, comparing to the

surfactants based on hydrocarbons, can decrease the interfacial tension more effectively and promote emulsion stability, compared with surfacetants on the basis of hydrocarbons [68].

The mass transfer of the fluid of the dispersed phase to the continuous phase is observed in some studies, which is referred as droplet *consolidation* or *compositional ripening* [69–72]. This process is accompanied by prominent reduction of the emulsion droplet volume as a function of time. Droplet consolidation was treated via a diffusion modal when the applied surfactant concentration is below its critical micelle concentration (CMC) and a molecular diffusion mechanism of the mass transfer was established [72]. The shrinking rate of droplets strongly depends on species of the oil and surfactants, if its concentration is above CMC [71, 72]. The mass transfer is independent of the saturation state of the continuous phase [72]. The end stage of the evolution can be extinction, in the case of water droplets, or non-spherical deformation of the aqueous droplets, if the droplets are employed for purpose of compartmentalisation [71]. The number of constitutent particles in the droplet influences the rate of consolidation. In general, the more particles the droplet constitutes, the lower the shrinking rate is [72].

The underlying mechanism of the compositional ripening process is that the surfactant micelles, present in the continuous phase, play the role of 'carriers' for the fluid of the dispersed phase [70]. Fluorinated surfactants combined with the usage of fluorinated oil are reported to hinder this compositional ripening process [68]. In both cases, the mass transfer of the dispersed phase fluid is not driven by the higher Laplace pressure of the smaller droplets from the small to big droplets, compared with the principle of Ostwald ripening.

For surfactant stabilized monodisperse emulsion droplets, an effective way to quantify the influence of surfactant concentrations in both compositional ripening and Ostwald ripening is to calculate the molecular area occupied by a surfactant. The idea is to categorize the consistency of droplet volumes over time, which can also be directly used to study the stability of emulsion droplets. The assumption is that all surfactants stay at the oil/water interface. The volume of the continuous phase V_c and D-Phase V_d are experimentally measured. The surface area a and volume v of a droplet can be calculated based on the diameter of the droplet d by πd^2 and $\pi d^3/6$. Therefore, the number of droplets n_d is given by V_d/v. The total surface to volume ratio of the system is

$$\frac{A}{V_c} = \frac{an_d}{V_c} \tag{2.2}$$

and the volume density of the surfactants is given by

$$\frac{n_s}{V_c} = \frac{c_s \rho_c V_c N_A}{V_c M_s} \tag{2.3}$$

with the concentration of the surfactant in continuous phase c_s, the density and molecular mass of the surfactant ρ_c and M_s. The molecular area occupied by a surfactant molecule is

$$\sigma = \frac{A}{n_s} = \frac{\frac{A}{V_c}}{\frac{n_s}{V_c}} = \frac{a n_d M_s}{c_s \rho_c V_c N_A} \tag{2.4}$$

Emulsion stability can be studied based on the molecular area of surfactant σ and the consistency of the emulsion droplet volumes with time. The mechanisms of the mass transfer can be examined by the dependence of droplet shrinkage of the molecular area occupied by each surfactant.

2.2 Materials and Methods

2.2.1 Surfactants and Carrier Oils

A variety of surfactants were used in the W/O emulsion applications to stabilize the water droplets. They were dispersed in the oil phase. In our experiments the common used oils were paraffin oil (density of 0.827-0.890 g/mL at 20 °C Sigma-Aldrich Co. LLC.) and perfluorinated FC-40^{TM} (density of 1.76 gm/ml at 25 °C, 3M Deutschland GmbH).

Abil EM90® (CL 530) was used to study the stability of the aqueous droplets in the carrier oil phase of paraffin oil. It is a mixture of modified polyether-polysiloxane dimethicone copolyol, also named as Cetyl PEG/PPG-10/1 Dimethicone (Evonik GmbH). It is often used as stabilizer in cosmetic products. The number average molar mass of Abil EM90® is in excess of 1000 with significant amount of low molecular weight species below 1000 (less than 9 %). Because of the flexible siloxane linkages of this emulsifier, the hydrophobic methyl substituents are allowed to align towards the non-polar phase and polysiloxane backbone heads towards the polar phase.

The fluorinated surfactant Pico-Surf^{TM} is a formulated chemical solution, in which the fluorous biocompatible copolymer surfactant (Sphere Fluidics Limited, The Dolomite Center Ltd.) is dispersed in the carrier oil FC-40^{TM}. The surfactant content is varied from 2 to 5%. In our

application, the lowest 2% of Pico-Surf^{TM} in FC-40^{TM} was chosen, which is recommended for stable droplets with diameter from 25 μm to 100 μm.

2.2.2 Surface Treatment

In this work, two kinds of surface reactive chemicals were used to prepare the non-sticky surface of the microfluidic channels to water objects, either a siliconized surface or fluorophilic surface. Sigmacote$^{®}$(Sigma-Aldrich Co. LLC.) is a clear and colorless heptane solution containing a chlorinated organopolysiloxane and it reacts with surface silanol groups on glass surface to form a neutral, hydrophobic coating film. The coating film is often used for preparing non-sticky surfaces for water objects. In this case, it is neither hydrophilic nor lipophilic. Pico-Glide^{TM} is another commercial product of specially formulated perfluorinated oil carrying 0.5% (w/w) functional perfluoropolyether (PFPE) (Sphere Fluidics Limited, The Dolomite Center Ltd.). The Pico-Glide^{TM} reacts to plasma treated surfaces and forms an even and dense fluorophilic surface which bond covalently to the surface. The standard hydrophobic coating of the dolomite chips is not optimised for the system, as suggested by the producer. Therefore, the Pico-Glide^{TM} coating (fluorophilic) on the channel surface combining with the usage of Pico-Surf^{TM}(fluorocarbon oils) is used to promote droplet generation process.

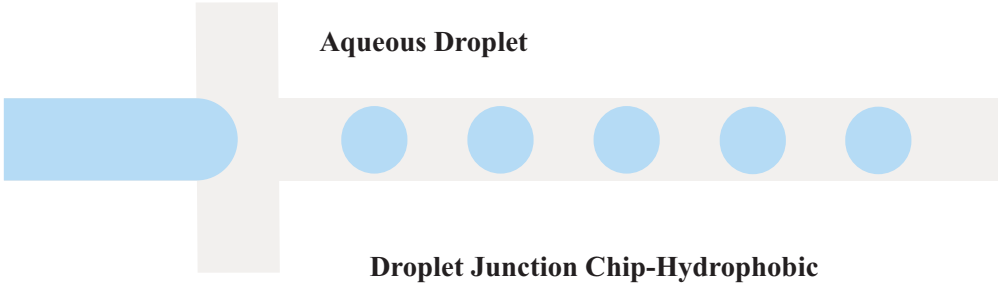

Figure 2.2: *W/O Droplet Production in Hydrophobic droplet generator*

2.2.3 Experimental Setup

The flows of the C-Phase and D-Phase within microfluidic channels were driven by pressure, the Mitos Pressure Pumps (Mitos P-Pumps)(The Dolomite Center Ltd., Fig.2.4(a)). The Mitos P-Pumps allow a wide range of pressure up to 10 bar. In this application, a highly stable flow is required in an equally broaden range of shear rates from nl/min to μl/min, which ensures the generation of monodisperse droplets with constant diameters.

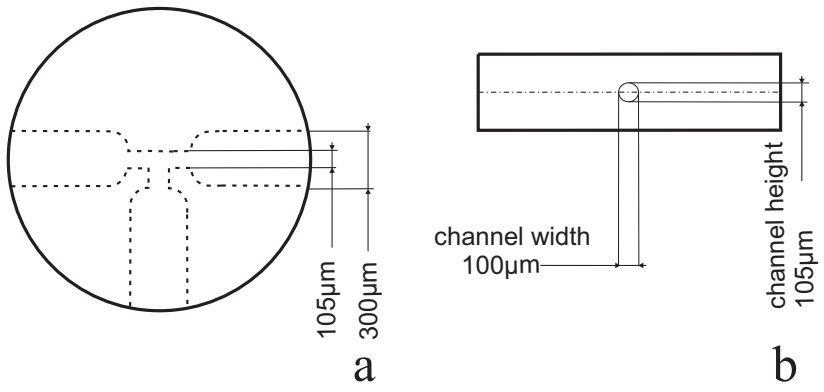

Figure 2.3: *Sketch of droplet generator chip.*

In general, the pulseless flow was generated by applying variable laboratory air pressure onto the isolated sample chamber, which was fitted with a lockable pressure chamber for safety of operation. The fluid sample can be contained in glass vials or plastic tubes with the help of vessel holders kit(The Dolomite Center Ltd., Part No. 3200017). The fluid sample is assumed to be uncompressible and it is pushed into the tubing which connects the fluid vessel, the flow resistor (Fig.2.4(b)) and the droplet generator chip, Fig. 2.4(c). The system is connected with pneumatic tubing (6 mm outer diameter (OD), 3 m length) and quick connect fitting. For the application in the X-junction droplet generator chip, the tubing was aligned properly with a lock pocket for splitting the inlet phase. Typically the tubing guides the fluidic sample from the sample reservoir in the isolated pressure chamber to the droplet generator. The typical dimension of the tubing is 250 μm ID, 1/16" OD.

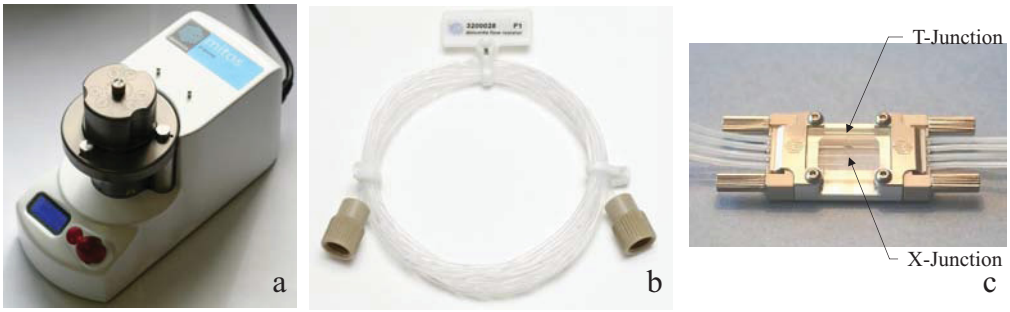

Figure 2.4: *Mitos P-Pump* ***(a)****, Flow Resistor F1* ***(b)****, and Droplet Generator Connection with T- and X-junction* ***(c)****. Pictures are taken from dolomite website.*

In order to generate aqueous droplet containing *fd* virus, *fd* virus dispersion, the D-Phase was dispersed into the Pico-Surf^{TM} 1, 2% in FC-40^{TM}, the C-Phase. The emulsification takes

place in hydrophobic Dolomite Droplet Junction chip with 100 μm etch depth (Part Number. 3000301, Fig. 2.2).

The connections for the experiments were prepared, including the flow resistors and suitable tubing. After the Mitos P-Pumps was switched on and 'wearing safety glasses' safety reminder was confirmed, the target pressure was set. Then the fluid vessel was inserted into the pressure chambers. The fluidic samples ought to arrive at the junction of the microfludic chip simultaneously by adjusting the flow frontier in the inlet tubing. The chamber pressures were adjusted gradually until a suitable range of pressures for stable droplets formation was found as well as the desirable size of droplets. For fine tuning of the applied pressure, flow resistors were mounted into the fluidic path (Fig. 2.4).

VitroTubes^{TM}(VitroCom) glass capillaries were used to store the droplets after the droplet generation process, which facilitate further optical observations. VitroTubes^{TM} glass capillaries were treated with the solution of 2% Hellmanex$^{®}$III solution, MilliQ water and Ethanol. In each step, the glass capillaries were sonicated for 20 min at 70 °C and rinsed thoroughly with MilliQ water. Then the glass capillaries were air dried. In the end, the glass capillaries were air dried in the heating vacuum oven at 70 °C to evaporate the rest heptane.

To coat the capillaries, they were completely filled with Sigmacote$^{®}$ or Pico-Glide^{TM} by capillary force. The coating was kept in capillaries for 2 hours in the hood. Then, the capillaries were transferred to the oven at 100 °C in vacuum till the solvent evacuate completely. The glass capillaries were then rinsed thoroughly by loading the capillaries with MilliQ water, Ethanol subsequently to remove the HCl by-products. The capillaries with siliconized inner surface were dried with compressed air and kept at 100 °C for 30 min in vacuum oven for a slightly more durable coating layer. The siliconized coating can be tested by rinsing or dipping the glass capillaries and observing the "beading" or "sheeting" of water on the outer surface, or non-water filled capillaries.

The outlet of the system was guided to the VitroTubes^{TM} glass capillary with coated inner surface. By capillary force, the capillary is fully filled during droplet production. The excess liquid is wiped off and the glass capillary was sealed on top of the glass slide by Ultraviolet Cure Adhesive, Norland Optical Adhesive 81 (NOA 81) with UV-light induced curing (polymerization). The NOA 81 from Norland Products Inc. is sensitive to wavelength light range from 320 to 380 nanometers with peak sensitivity around 365 nm. The samples labeled with fluorescence dye are covered with sufficient Aluminum foil to prevent bleaching of the dye. The UV radiation should last at least 20 min to make sure the ultraviolet adhesive NOA

81 is completely solidified. The samples were then stored in the dark for potential optical observations.

2.2.4 Imaging and Image Analysis

The droplet generation process were observed using the Zeiss Axioplan 200 microscope with a 5x Plan-APOCHROMAT objective, NA0.45, equipped with a "Pixelink" camera (3x binning and 32 ms exposure time). For the later droplet stability study, the sizes of droplets were obtained by numerical analysis of the bright-field microscope images, with a home-written software using IDL, in which each droplet was identified. The volume of the droplets were recorded over time.

2.3 Results and Discussion

2.3.1 Droplets Production using Microfluidics

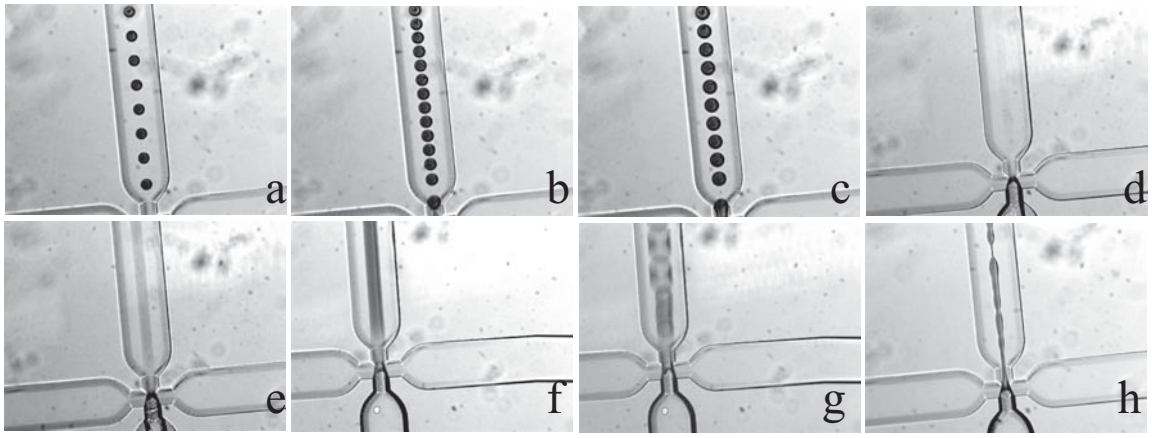

Figure 2.5: *Variety of droplet productions, from small to big droplets, (a)-(c). The trajectory of droplets is shown in (d)-(f), when the droplet generation takes place at high flow rates. Unstable conditions for droplet generations is shown in (g) and (h).*

The scenarios of droplet detachment depend on the variation of applied pressure ratio. The droplet size can be varied with slow flow rates, from small to big droplets, Fig.2.5(a)-(c). In the high flow rate case, one can hardly see each single droplet, but a trajectory of the droplets in the middle of the channel leading to the exit, Fig.2.5(d)-(f). The size of the droplets can still be adjusted. However, the droplet production is problematic when the pressure ratio of the

P_c/P_d is small. The relatively weak dynamtic stress of the continuous phase is not sufficient to break the D-Phase, therefore it leads to the co-flow of the D-Phase and the continuous phase, see Fig.2.5 (g) and (h). It is opposed to the transition of droplet detachment from dripping to jetting by increasing the P_c, which results a higher capillary number Ca. The droplet productions is therefore mainly conducted within the stable flow range. It ensures the stable droplet productions and the reproducibility of our experiments.

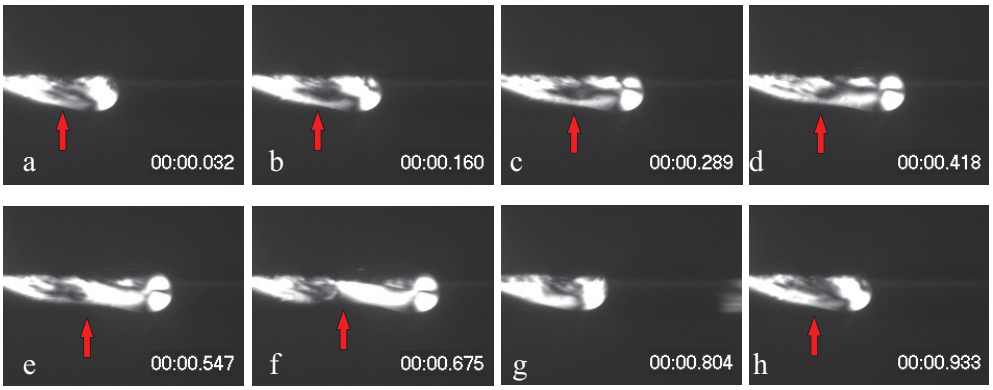

Figure 2.6: *The typical example of droplet pinched off at T-junction with long exit. Continuous phase was fitted with the flow resistor F10, and D-Phase with F30.*

Ideally, the kinetics of droplets pinching-off at the x-junction is a result of the thinning of the liquid neck of the D-Phase by the local dynamic stress of C-Phase, see Fig. 2.1. This is a continuous procedure where the produced droplets follow the channel to the exit. We also observed more complicated production of the monodisperse droplets. Fig.2.6 depicts a series of snapshots during the production of droplets containing the chiral nematic phase of *fd* virus taken at the T-junction of the microfluidic channel. Here the C-Phase here is paraffin oil and the FC-40^{TM} chip was used which has a long exit chip of zig-zag shape. The red arrows are used here to illustrate the position where the thinning of the liquid neck occurs. According to the record of the live stream, the thinning of the liquid neck lasts from Fig.2.6 (a) to (f). In Fig.2.6 (g), the liquid neck retracts to the initial state after the previous droplet was snapped off. As the D-Phase grows and the shear of the C-Phase continues, the liquid neck thinning cycles again. In principle, one might obtain the dynamic interfacial tension from the liquid thread profiles and some information of the local alignment of the chiral nematic LC rods based on the polarization pattern, which is introduced in chapter 1. However, understanding of this behavior is a nontrivial example because it involves the sheer induced alignment of the chiral nematic LC rods, the viscoelasticity of the structure before and after alignment, the

possible wetting problem caused by the coating protein of the *fd* virus, and so on. It is shown here because it is of potential interest for the work presented in Chapter 5.

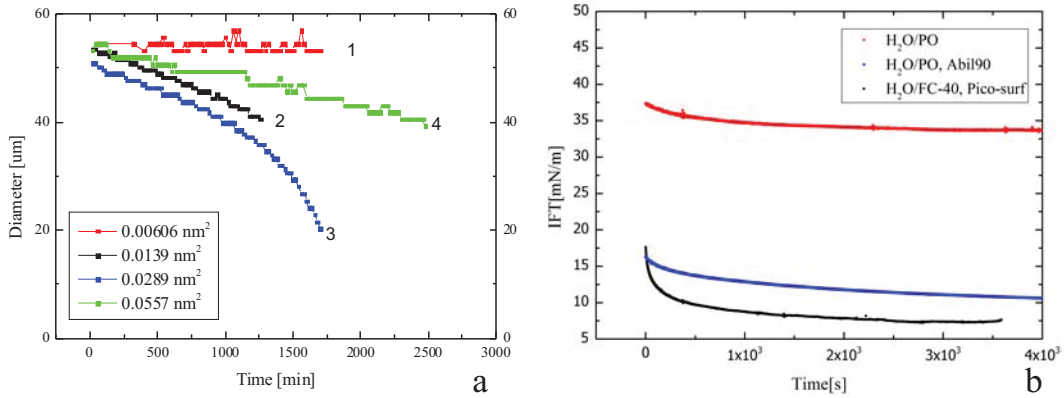

Figure 2.7: *Droplet diameters as a function of time for dropletsa(a), which are stabilized by Abil EM90® in paraffin oil. The initial droplet diameters were about 53 µm. The variation of droplet diameters are related to the order of increasing effective surface areas of surfactants. The interfacial tensions of the applied systems are shown in (b).*

To ensure the droplet generation, we start with the proper calibration of the flow system. The C-Phase was the mineral oil and D-Phase was MilliQ water. The geomerty of the microfluidic chip was fitted with X-junction. The flow rate was calibrated by collecting and measuring the liquid sample from the outlet. The system was tested without surfactant or very little amount of surfactant, so that the resulting liquid sample eventually phase separated into oil phase and water phases. Some small amount of Abil EM90® was used in partial experiments in order to test the influence of the added surfactant.

The relation between the applied pressure with the resulting flow rate and the dimension of formed droplets are shown as an example. The pressure of D-Phase was varied (0.8-3 bar) by fixing the pressure of C-Phase at 3 bar. As a result, the flow rate between C-Phase and D-Phase V_c/V_d was greatly influenced. In Fig. 2.8(a), the dependence of the flow rate ratio V_c/V_d on the applied pressure ratio between the C-Phase and D-Phase P_c/P_d is shown. It is clear that the flow rate ratio V_c/V_d increases with increasing applied pressure ratio P_c/P_d at the beginning. The V_c/V_d does not have a simple linear dependence on the P_c/P_d, showing a stronger increase at higher P_c/P_d. Fluctuations cannot be avoided, due to the accuracy of our measurement method and the non-stable flow at high flow rate. Further increase of pressure ratio P_c/P_d led the retreat of D-Phase's fluidic sample in the upstream part of the channel. This kind of behavior is also described by Cramer *et al* [65], where they described the similar trend

of the monotonically decrease of the droplet sizes with increasing flow rate of the C-Phase, see examples from Fig.2.5c to a.

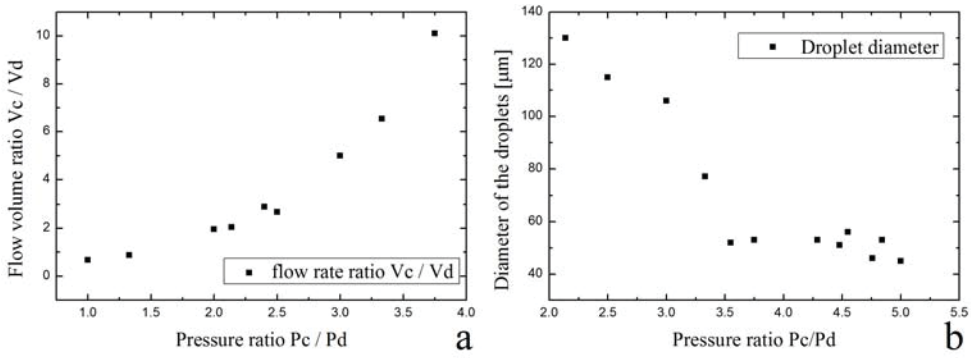

Figure 2.8: *Calibration of the dolomite microfluidics.* ***(a)****.Dependence of flow volume ratio V_c/V_d on applied pressure ratio P_c/P_d. The pressure of C-Phase was constant of 3 bar.* ***(b)****.Droplet size depending on the applied pressure ratio P_c/P_d.*

The dependence of the resulting droplet diameter on the applied pressure ratio is plotted in Fig.2.8(b). Droplets were produced with a diameter in the range of $50-130\mu m$. In general, droplet diameter decreases with increasing P_c/P_d. When the P_c/P_d is less than 3, the decrease of the droplet diameter is almost linear. After P_c/P_d reaches 3.5, the system seems to reach its limit. The droplet diameter fluctuates around 55 μm and this is most probably limited by the junction. The further increase of P_c/P_d also leads to low droplet production efficiency, which binds to the droplet generation rate, see examples of Fig.2.5b to a. The fluctuating droplet diameters ($P_c/P_d \geq 4.5$) are due to the unstable flows.

2.3.2 Stability of Water Droplets

The kinetics of emulsion droplet stability and its dependence on the molecular area per surfactant σ was studied by following the droplet diameter in time. We calculated σ using Equ. 2.4 with the size determination as described in section 2.2.4 and molecular parameters as described in section 2.2.1 as input. The minimum surfactant molecular area found to be $\sigma \leq 0.0557nm^2$. At lower surface coverage droplets would coalescence and wet the glass substrate. When increasing the surfactant concentration we observe a monotonous trend, as can be appreciated from Fig.2.7a, where the droplet size of the major population was plotted for four different surfactant molecular areas σ. The curves are labeled in the order of the decreasing σ.

Droplets were found consistent with their volumes if the surfactant molecular area σ is smaller than 0.00606 nm^2. It is presented as the red curve in Fig.2.7.a. In this case, droplets formed many small droplets initially at the interface, as satellites 2-3μm, which is referred as *budding*, see Fig.2.9. Most of the satellites gathered at the interface and block the path of further budding by their full coverage of the initial droplet (Fig.2.9e-h).

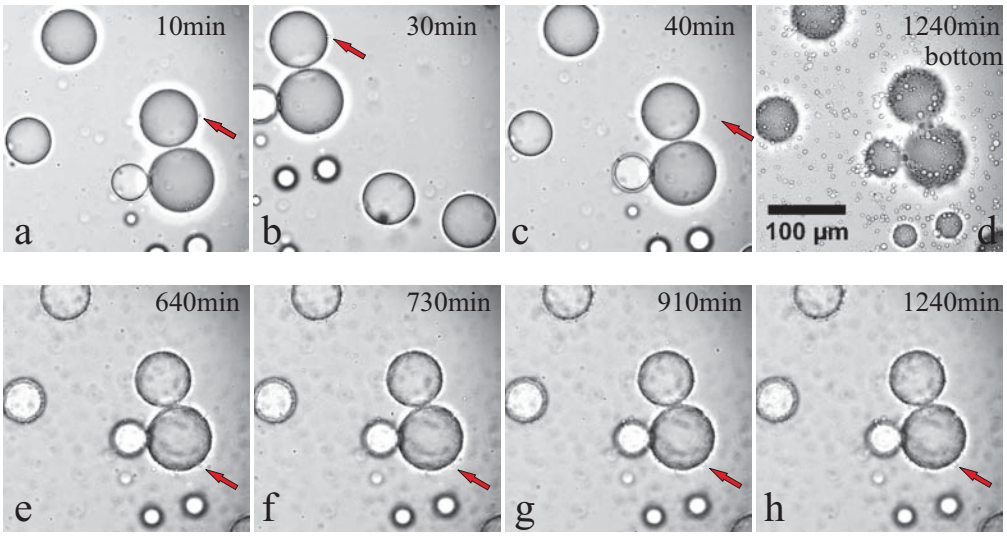

Figure 2.9: *Example of budding on the surface of the w/o emulsion droplets. The budding process is recorded at different time point, (a)-(c), and (e)-(h). The settled satellites on the glass wall are shown in (d). The arrows are used to mark the position of the satellites.*

Droplet shrinkage process was very pronounced in curve 2 and 3, when the molecular area of each surfactant increases. The droplets were observed in a shorter period of about 20 hours in curve 2. The constant decay of droplet diameters were observed. Droplets formed a few satellite droplets with the major lubricated interface. Curve 3 represents similar systems but observed up to 28 hours till droplets vanished. This is similar to what was observed in the study of He *etal* [71]. The curve 2 and 3 are treated indifferent due to the initial difference of the droplet diameter and the similar slope of the decay curves.

Further increase of the molecular area of a surfactant σ leads to a process of droplet shrinkage with slower rates, see Fig.2.7.a.curve 4. The monotonic decay of the droplet diameter lasts up to 2 days.

Our quantitative study of the droplet shrinkage lies in the mechanisms depending on effective molecular area taken by a surfactant, which suggests the micelle carrier mechanism suggested by Binks *etal* [70]. The smaller effective molecular area each surfactant takes σ,

the more excess surfactant micelles present in the continuous phase. The mass transfer of the dispersed phase fluid from droplet to oil is more prominent. In curve 4, both the molecular diffusion mechanism proposed by Shen *etal* [72] and the micelle carrier mechanism might occur. We suspect that the rate difference of the two might explain the turnover of the droplet stability from curve 4 to 2/3. Because the mechanism based on molecular diffusion has probably a much slower rate than the micelle carrier one. The rates depend strongly on individual experimental system [71], therefore no reference can be given in this case.

As the σ decreases, excess surfactants crowded at the w/o interfaces and formed micelles in the oil phase, for instance, curve 1. Droplets started to form satellite droplets of sub- micron sizes. The rate of budding probably is higher than the rate that the satellites displace from the interface, which terminated the budding and other interfacial activities of the surfactants by forming a thick steric layer of satellite droplets.

A supplementary study of the interfacial tensions of water/paraffin oil, water/Abil EM90®/paraffin oil, and water/FC-40™/Pico-surf is presented in Fig.2.7.b, in order to compare the efficiency of surfactant in reducing the interfacial tension. The presence of Abil EM90® is able to decrease the water/paraffin oil interfacial tension from 35 to 12 mN/m. The presence of Pico-surf can lower the water/FC-40™/Pico-surf interfacial tension down to 7 mN/m. Similar study of droplet stability using Pico-surf combined with FC-40™ was also performed and resulted much less prominent shrinkage of droplets with time [68]. Therefore the Pico-surf fulfills the duty of balancing the interfacial tension between the disperse and continuous phase.

2.4 Conclusion

In this chapter, we performed systematic study of monodisperse emulsion droplets generated by microfluidic devices, including the geometries of microfluidic chips, the proper surface treatment, flow control and scenarios regarding to droplet detachment. We performed the phenomenological study of droplet pitching off and observed both the dripping and jetting of the droplet detachment, which depends on the flow velocity of the continuous phase, and therefore the capillary number and binds to specific geometries of microfluidic chips.

We performed quantitative investigation of emulsion droplet stability based on the effective molecular area taken by each surfactant σ and probe the influence of excess surfactants on the stability of emulsion droplets. Droplet shrinkage was observed for most cases, except the novel

process *budding*, in which many small satellite droplets of sub- micron sizes form. These satellite droplets were emulsion droplets, and hindered the subsequent budding process by forming a thick steric layer on the droplet. We suspected that it is due to the excess surfactants on the water/oil interface given by the limited interface produced by microfluidic devices. The spontaneous formation of water/oil interface is probably more energetically favorable.

Droplet shrinkage is more pronounced as the σ increases, which is realized by the mass transfer of the dispersed phase fluid from emulsion droplets to the continuous phase by micelle carriers in the continuous phase. This takes place if there are prominent amount of excess surfactants present in the system. At high σ, the molecular diffusion mechanism might take place owing to the slowing down of the droplet shrinkage, compared to the cases with low σ.

The shrinkage of the water droplets was considered to be strongly related to the physical and chemical properties of the applied surfactants and the paraffin oil. It is very much of our interest to study the budding phenomena and droplet dissolution to determine whether the mass transfer involves only the solutes or also the compartmentalized particles [71]. In the end, we chose to use Pico-surf to fulfill the further compartmentalization purpose in chapter 5, considering the low interfacial tension and the stability of droplets.

3 Pickering Emulsion

In this chapter, Pickering emulsions stabilized by fluorinated latex-core-shell particles were studied. These particles, which are omniphobic, appeared to be extremely efficient in stabilizing water droplets in oil because only few particles are needed to avoid coalescence. We find that the efficiency of particle stabilization is due to a mechanism where only few particles are needed to form very stable bridges between two droplets. For this we used fluorinated latex particles with a fluorescent core, which enabled the confocal microscope observations at a single particle level. An experimental phase diagram of three component emulsion system was presented, in which the transition of emulsion stability was mapped.

3.1 Introduction

Additives are often used in the field of formulation, serving as stabilizers of emulsions or foams. A special class of additives are colloids which can irreversibly accumulate at the liquid-liquid interface [73]. If many solid particles are arrested at the interface then they promote emulsion stability and prevent the breakdown of emulsions by sterical hinderance when two droplets come into contact. These are the so called Pickering emulsions [74]. The destabilization of Pickering emulsions is similar to those conventional emulsions stabilized by amphiphilic molecules (described in Chapter 1), although Pickering emulsions are reported to be more stable. A pleasant example of colloids in food industry is given by ice cream forms stabilized by tiny fat globules to prevent the coarsening.

The driving force of forming Pickering emulsions is the tendency of solid particles to adhere at the oil-water interface, because that is their thermodynamically preferred position. This

force depends on the wettability by either one of the two phases. In case of stable emulsions the major part of the solid-particle is wetted by the continuous phase. The contact angle θ of the solid-particle at the oil-water interface is $> 90^\circ$ [74, 75], Fig.3.1.(a). Similar conclusion was obtained by the inversion of the transitional inversion of the emulsions from forming water in oil to oil in water emulsions, and later the transition of the oil in air or air in oil forms by promoting the hydrophilicity of silica particles [76, 77].

The presence of solid particles at the interface cannot, however, lower the interfacial tensions σ_i. The energy cost of generating Pickering emulsion is high, Eq.1.10, and therefore these emulsion are not thermodynamically stable. Pickering emulsions can be kinetically stable by resisting physical changes over time, which could for instance be due to coalescence.

Pickering emulsions are typical examples of emulsions stabilized by steric barriers. The classical steric hindrance is provided by solid-particles surrounding droplet surfaces. If emulsion droplets are covered completely by solid-particles then coalescence, which is a sign for emulsions destabilization, is prevented. When droplets come close to each other, two layers of particles form the *'bilayer' stabilization* [78], see Fig. 3.1.(b). The stabilizing mechanism based on this steric hindrance effect requires per definition a relatively large amount of solid particles because the full surface needs to be covered. This has many disadvantages for practical applications, because the solid particles will constitute a significant fraction of the product. Hence, it is of huge interest to increase the efficiency of the Pickering emulsion, which we define as the minimum surface area per particle needed to have a stable emulsion.

Alternatively, stable Pickering emulsions can also be formed when droplets are sparsely covered by solid-particles. Here, well-ordered particles form a monolayer at the interface. Under the circumstances of collision, particles are held in the thinnest contact interface between two droplets. The film bridged by particles can prevent coalescence of droplets and the interfacial region between droplets can be slightly deformed, Fig.3.1.(c) [75]. The mechanism of Pickering emulsion stabilized by *particle-bridging* has been studied by several groups [75, 79]. The thin liquid film between droplets is thermodynamically preferred by the solid particles, because of the energy cost of particle displacement from the thin liquid films [78]. *Limited coalescence* was observed at low particle concentrations for emulsions stabilized by particle-bridging [80]. Transformations of the system from transient unstable emulsions to final stable emulsions lead to reduction of interfacial area. The degree of particle coverage is improved at the same time, which is opposed to the surfactant stabilized emulsions.

Though the bridging mechanism might be more effective than the steric hindrance mechanism, still it requires a significant amount of material. In this chapter we introduce and

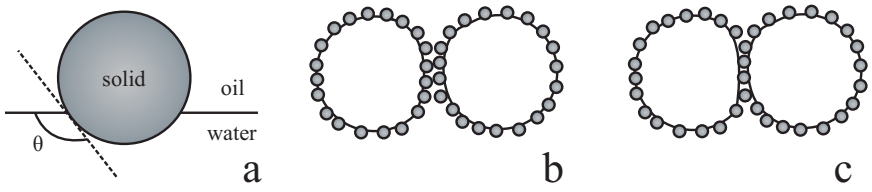

Figure 3.1: *Sketch of contact angles θ of a solid particle at oil-water interface (a) and possible configuration of particle-bridging between droplets (b).*

study an alternative way of stabilizing water-oil emulsions. The idea is based on the use of fluorinated colloids that are hydrophobic as well as lipophobic and therefore is omniphobic. The particles were first synthesized by Aussimont and also by Patmahanoharan [81]. Since these particles cannot be dispersed in either two phases, it is to be expected that they would strongly bind to the water-oil interface. In this chapter we study the stabilization mechanisms of Pickering emulsions using these omniphobic particles.

We will use confocal microscopy in combination with fluorescently-labeled fluorinated particles to locate the position of the particles, while we keep track of the droplet size distribution, using bright-field microscopy, in order to judge the stability of the emulsion. We start from observations of particles surrounding single droplets. Next, we characterize the structure of the stable emulsion, focussing on the distribution of particles at the oil-water interface. We finish by mapping the ternary phase diagram of water-oil-particle identifying the region where emulsions are stable. We will show that the efficiency of the fluorinated particles is orders of magnitude higher than conventional Pickering emulsions.

3.2 Materials and Methods

Fluorinated latex core-shell particles were prepared in our laboratory via two-step polymerization processes of the monomer 1H,1H-HeptaFluoroButyl Methacrylate (FBMA, $CH_2 = CHCOOCH_2(CF_2)_2CF_3$, 97% Lancaster), in the presence of Sodium dodecyl sulfate (SDS, as surfactant), and Potassium persulfate ($K_2S_2O_8$, as initiator) [81]. This is realized by a two-step emulsion polymerization. First, the fluorescently labeled monomers (Rhodamine B) were added resulting in a fluorescent core, which is covered in the second step. The hydrodynamic radius of the resulting FBMA particles is about $380nm$. The particles are negatively charged, with a charge density that depends on the concentration of the initiator.

Emulsions consist of paraffin oil (Sigma-Aldrich Co. LLC., carrier oil phase) and aqueous dispersions of FBMA particles (as the dispersed phase and solid stabilizers), because in the stock solution the FBMA particles are dispersed in the water after the polymerization procedure. The mass fraction of the particles in the stock solution was measured by evaporation of the solution and was found to be 2%wt. Using the density of the FBMA particles of 1.6 g/ml this corresponds with a volume fraction in the stock of φ=1.25%. The desired volume fraction of the FBMA particles dispersed in water was obtained by a few dilution steps. The stock solution was homogenized prior to experiments. For a few selected experiments Fluorescein-isothiocyanate-dextran (FITC-Dextran, average mol wt of 4000, FITC:Glucose=1:250, Sigma Aldrich) was dissolved in the water, in order to image the water in confocal microscopy experiments with the end concentration of 0.5 mg/ml.

The emulsion was prepared by mixing the FBMA particles suspension with paraffin oil mechanically and then homogenized by a sonication process for 2-3 minutes. Glass capillaries VitroTubes^{TM} with inner thickness of 100μm were filled with the emulsion by capillary force for microscope observations. Systematic tests were carried out to study the emulsion stabilities with various compositions. Volume ratios of water and oil phases (W:O) were varied from 1:100, 1:50, 1:25, 1:10, 1:5 to 1:2. For each ratio, the volume fractions of FBMA particles in water was varied, given by the constant volume of paraffin oil of 10 ml.

The resultant droplets were investigated using the Olympus IX71 microscope fitted with the objective UPLSAPO 60$\times$w,NA1.2. This microscope has the option to simultaneously capture a bright-field image, using a detection unit connected to the condenser, and a fluorescence confocal image, using the standard channel. Kinetic stabilization of emulsions against coalescence was studied over a period of 10 days.

3.3 Results

There are basically two steps in the phase separation processes of oil-water emulsions. First the small droplets coalesce and then the phase with the lowest surface tension wets the wall. We will see that the addition of FBMA particles affects both process.

3.3.1 Stability against Coalescence

In Fig.3.2.a we display an example of the polydisperse emulsions taken shortly after sample loading for systems where droplets are sparsely covered by the FBMA particles. The image is an overlay of a bright field image, showing the emulsion droplet, and a confocal microscope images, showing the location of the FBMA particles. For isolated droplets we observe that the FBMA particles are held by the interface as expected, see the upper right example in Fig.3.2b, which is a local 'zoom-in' of the region marked in Fig.3.2a. This droplet is stabilized by a single particle which prevents wetting of the water phase at the wall. This will be discussed in the next section. The fine structures at single particle level is resolved, however with the cost of the overexposed region where many particles accumulate.

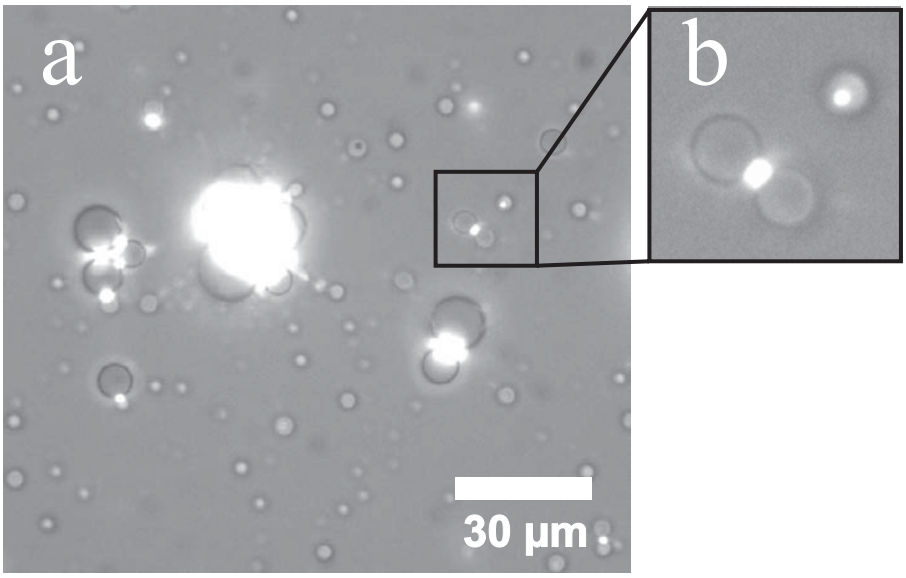

Figure 3.2: *(a) Overlay of a bright field image and a confocal image of pickering emulsions stabilized by fluorescently labeled fluorenated latex particles. (b) The 'zoom-in' of the region indicated indicated in a, showing two droplets that are stabilized after collision (lower left) and after sedimentation to touching the oil-water interface (upper right).*

When droplets are in contact, we observe a very surprising phenomenon: even though we have just a few FBMA particles per droplet, droplets remain stable after collision. This can already be seen in Fig.3.2b at the second arrow where two droplets are in contact but separated by fluorescent particles. In Fig.3.3 we resolve this effect more extensively. The FBMA particles (in red) are strongly located at the point of contact between the two droplets, which do not show any deformation, as can be appreciated from the FITC-Dextran (in blue) which mimics

to location of the water. These figures are part of a z-stack of images taken from the bottom of the chamber upwards into the chamber, scanning sedimented droplets. Clearly there are also particles which are located at the contact region between the droplets and the glass wall. This is contrast with the particle-bridging Pickering emulsions which do not show a contact point but a contact region and a local flattening of the droplet, as depicted in Fig. 3.1. The localization of the FBMA particles at the contact point before coalescence takes place suggests that the FBMA particles very quickly migrate to the contact point when the droplets collide. Due to the limited time resolution of our experiment we could not follow this migration process. In case there are more FBMA particles, they will all assemble at the contact point and one can not resolve single FBMA particle due to the dense packing.

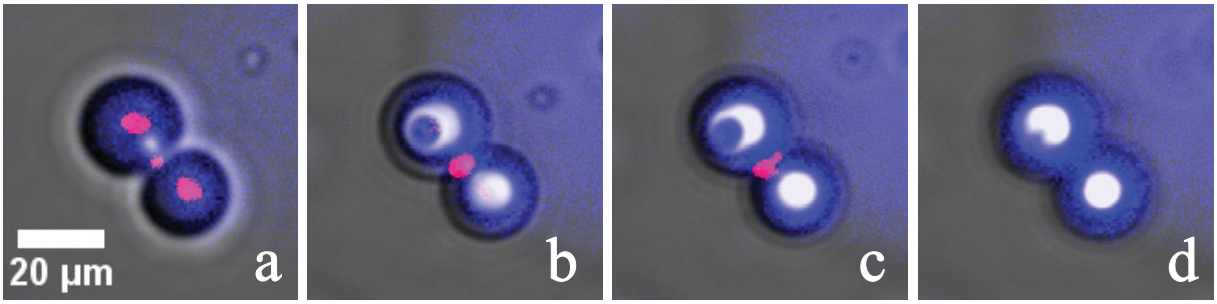

Figure 3.3: *Example of stable droplets against coalescence. The FBMA particles are in red and the dispersed aqueous phase is in blue, due to the dissolved FITC-Dextran in the water phase. The figures from a to d are captured during scanning of the samples from the bottom of the glass wall to the top of the droplets. The upper right part of the background is wetted by droplets, which is indicated by the fluorescence marked in blue.*

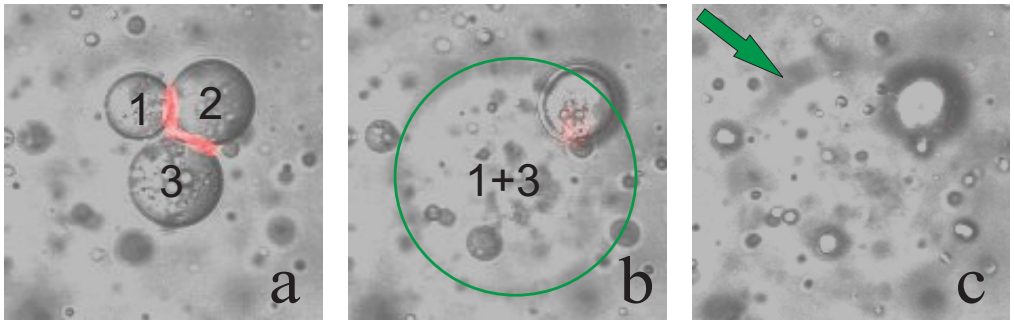

Figure 3.4: *Example of coalescence of droplets. Overlaid bright field and confocal microscope images are shown to define the interfacial area. The FBMA particles accumulate between droplet no. 1 and 2, as well as 2 and 3. The coalescence of droplet no. 1 and 3 takes place during capturing figure a and b. The rim of the wetted glass wall was marked with green circle in b, obtained as the focus of imaging approaches the glass wall in c.*

It is expected that the emulsion destabilizes when there are no FBMA particles available, so that droplet coalescence takes place when the stabilizing particle is absent. Fig.3.4 displays a sequence of images taken in a relatively short time frame (from a to c), exemplifying that droplets that were covered with a limited amount of FBMA particles, collide and eventually coalesced. In this figure the red colour sources from the fluorescent FBMA particles. Comparison with the bright field image in Fig. 3.4a shows that FBMA particles accumulate between droplet no. 1 and 2, as well as 2 and 3, but not between 1 and 3. Between Fig. 3.4a and b we observe a sudden coalescence of droplet no. 1-3. The resulting droplet wetted the underlying glass surface, Fig.3.4b. The green circle in Fig.3.4b marks the rim of the wetted glass surface which formed by the coalescence of droplet no. 1 and 3 and is obtained from an image at the glass wall, Fig.3.4c .

At higher volume fractions of FBMA particles we observe that not all FBMA particles migrate to the contact point, 3.5a. At very high volume fractions we observe that particles equally distribute over the surface and become immobile, see 3.5b and c. This is probably due to the fact that the particles are highly charged and therefore repulsive. We also observe that an access of FBMA particles will not be adsorbed by the contact area but will stay at the freely accessible interface, as can be observed for the small droplet in Fig. 3.5c.

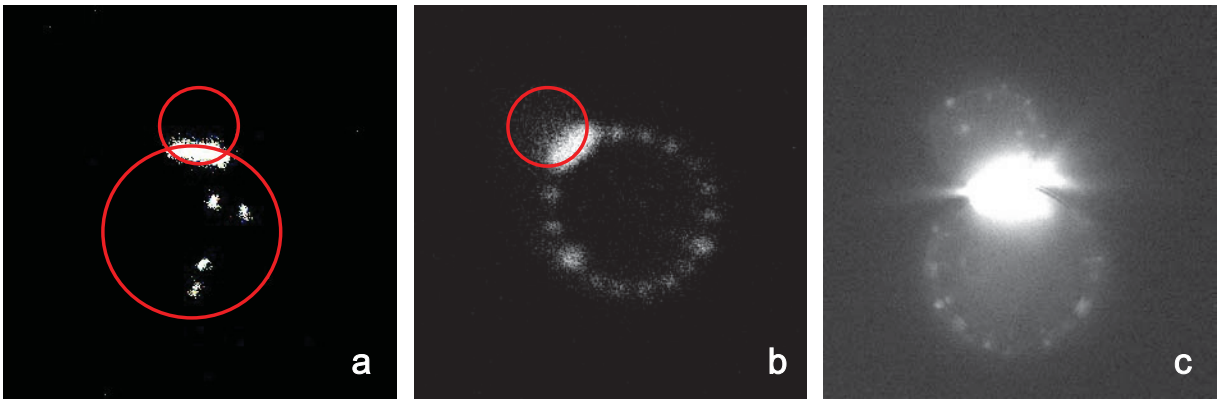

Figure 3.5: *Particle-bridging formed between two droplets. The particle coverage of droplet increase from (a), (b) to (c). Red circles in (a) and (b) refer to droplets with poor visibility, because particles they possess only attach to the contact regions between droplets. Particles on the big droplet (a) and small droplet (c) diffused freely.*

We have shown the influence of the FBMA particles on droplet coalescence up to now. The stable emulsions are formed with the droplets sparsely covered with FBMA particles to resist the coalescence. Droplet coalescence with the absent of the particles at the contact point is observed and a subsequent wetting of the ruptured droplets to the glass wall links to

the second important issue during phase separation of the oil-water emulsions, which is the stability against wetting.

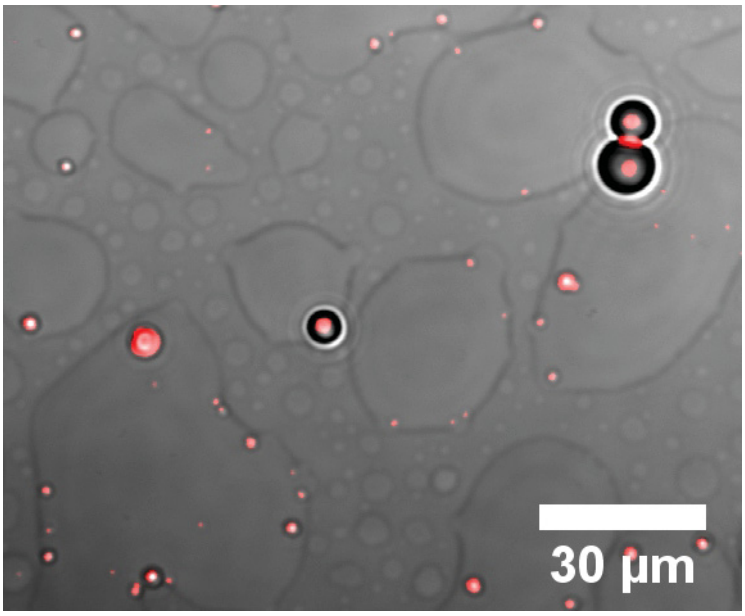

Figure 3.6: *Example of stable droplets against coalescence. The FBMA particles are in red and the dispersed aqueous phase is in blue, owning to the dissolved FITC-Dextran.*

3.3.2 Stability against Wetting

Wetting of the aqueous droplets with the glass wall is observed for emulsions close to the transition from stable to unstable emulsions, when decreasing the volume fraction of particles. As water has a higher affinity for the glass wall than the oil and as is also more dense, it is expected that a completely wetted bottom wall is observed. An example of such a system close to the transition to complete phase separates is shown in Fig.3.6. This example was captured close to the glass wall, where we observe the sharp interface of the oil-water-glass three phase boundary.

Interestingly, we observe no complete wetting but rather a wetting landscape by comparing the confocal image with the overlaid bright field microscope image. The FBMA particles (in red) accumulate at the contact lines between partially wetting droplets and the glass surface. They also accumulate at contact points between sedimented droplets and the contact line between the glass surface and the partially wetting droplets. The particles jitter around a fixed

position and prevent the aqueous phase from complete wetting, although the wetting angle of the droplets is very small.

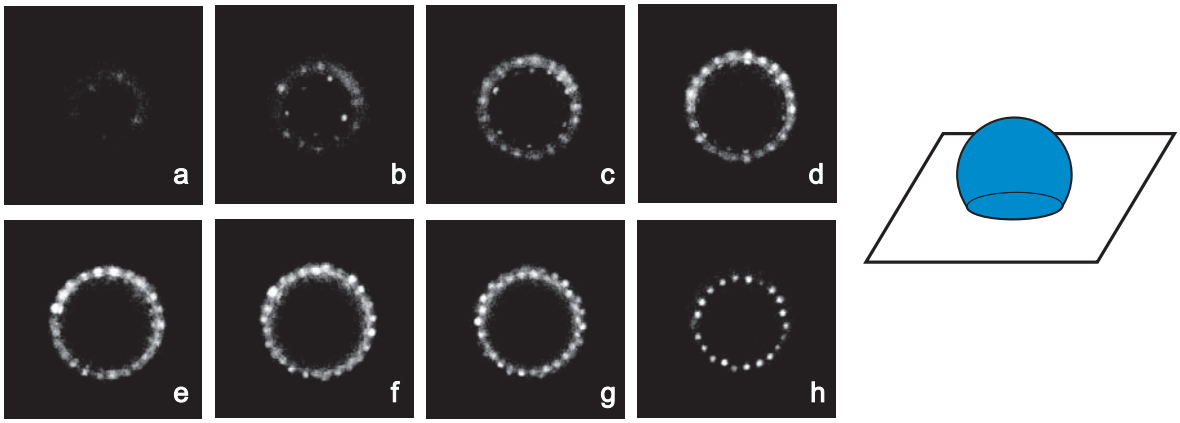

Figure 3.7: *Representation of droplets sparsely covered by solid particles, which form lattic structure within monolayer.*

At higher volume fractions we observe that the sedimented droplets have a high wetting angle, as can be inferred from Fig.3.7. Here, a z-scans of the droplet is performed and presented from the top to the bottom of the droplet accordingly, Fig.3.7a-h. A sketch of the sedimented droplet is given on the right. The FBMA particles can be observed as bright dots in the figures and again it is observed that they are equally distributed exemplifying the repulsion between the particles.

At the top of the droplet we observe particles that can freely diffuse at the water-oil interface, see Fig.3.7a and Supplementary info. When approaching the wall, the lattice structure is observed and the particles are more strongly localized, see Fig.3.7b-g and Supplementary info. At contact with the wall we observe a sharp rim of regularly spaced particles located at the three-phase boundary (water-oil-glass wall), see Fig.3.7 h. The particles are immobile at the glass wall and prevent the droplet from spreading on the glass.

With further increase of the particle volume fraction we observe complete dewetting, so a very high contact angle, as can be inferred from Fig.3.8. A thick layer of particles can be seen through out the droplet, from Fig.3.8a-h. The droplet that is depicted here has a diameter of the droplet at the equator is around 300 μm while the vertical distance of the glass capillary is 100 μm. Thus, this droplet is highly compressed by the chamber. This shows the efficiency of the FBMA particles as stabilizers, since no wetting is observed despite of the compressional force.

We have now identified the stabilization mechanism for the FBMA particles. These pref-

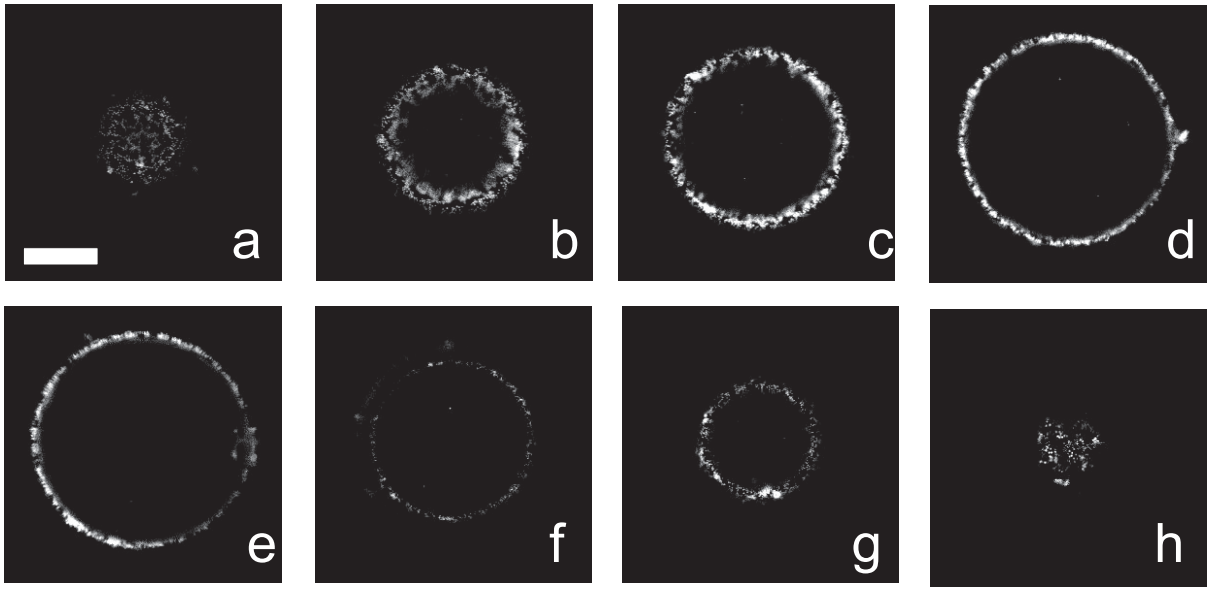

Figure 3.8: *An example of droplets covered completely by FBMA particles. The signal is provided by fluorescent cores of these particles, as a reflection of the boundary of droplet. The indicated scale bar is 100 μm.*

erentially accumulate at the oil-water-glass three phase interface and stabilize droplets from spreading on the glass surface. For the systems close to the critical transition from stable to unstable emulsions, the FBMA particles pin at the three phase boundary with highly curved interface and prevent the further spreading of the wetted landscape. The quantitatively study of the kinetic stability of emulsion droplets is needed to probe the states of emulsions with various compositions.

3.3.3 Ternary Phase Diagram of Emulsion Composition

The kinetic stability of emulsions is studied tracking the emulsion droplet size distribution with time by bright-field microscopy. The rapid coarsening of droplets in the initial stage is observed as described in the introduction. Fig.3.9 displays a growth of the average droplet size for different volume fractions of particles. These plots can be employed to quantitatively define the boundary of emulsion stabilization volume fraction for a volume ratio of water:oil of W:O, 1:25 in a and 1:2 in b. Droplets were prepared using the same protocol and therefore the initial size distribution of the droplets is comparable for samples with different volume fractions. The observation time window of droplet size variation is set to 10 days in this case.

If the particle volume fraction is too low we see a complete oil-water phase separation

within 2 hours, as the black, red and blue curve shoot up in Fig.3.9a and b. In contrast, the kinetically stable emulsions have a gradual increase of the droplet sizes as a function of time. Clearly there we can identify a sharp transition in particle volume fraction: a stable emulsions form with particle volume fractions more than 0.19% in emulsions with W:O=1:25 and 0.62% in emulsions with W:O=1:2, while they are unstable for volume fractions of 0.18% or less in emulsions with W:O=1:25, and 0.62% or less in emulsions with W:O=1:2, respectively. Therefore, we find that the particle volume fraction of 0.19% in emulsions with W:O=1:25 and 0.62% in emulsions with W:O=1:2 are the critical volume fractions of the FBMA particles to form stable emulsions.

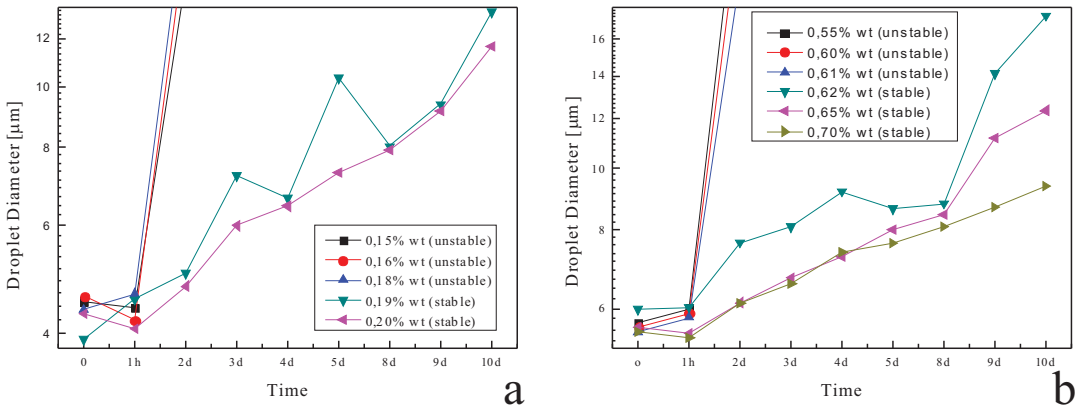

Figure 3.9: *Stability of the FBMA particles stabilized emulsions. Droplet diameters are plotted as a function of time. Volume ratios of W:O is 1:25(a) and 1:2(b). The weight percentages of the FBMA particles in water are distinguished with different colors in both figures, with the stability of the emulsions indicated in the legend.*

We can now construct a phase diagram of this system using the thus obtained transitions for the different compositions of the water-oil-particle studied. We plot the phase diagram in Fig.3.10 where we converted the mass fraction to the ratio of the volume fractions of the oil over the volume fraction of the particles, $lnV_{oil}/V_{particles}$. The black dots are experimental data of critical particle concentrations. Emulsions were kinetically stable over time when their compositions located above the critical line.

3.4 Discussion

The FBMA particles were employed to stabilize water in oil emulsions. The kinetic stability of the emulsion droplets was studied by observing the distribution of the FBMA particles at the

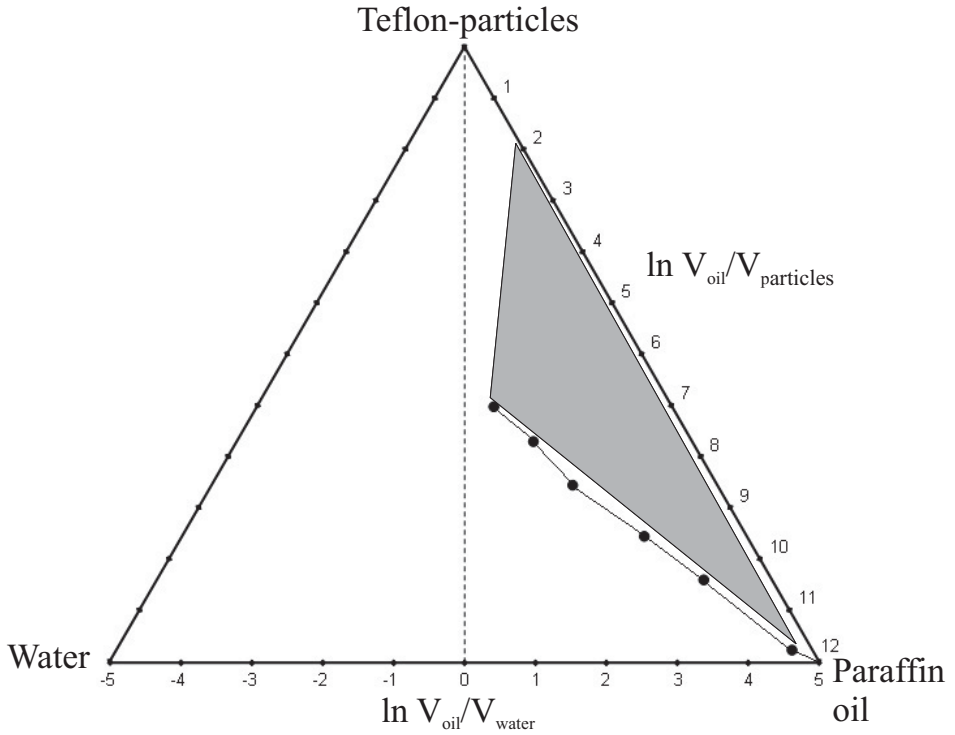

Figure 3.10: *Phase diagram of Pickering emulsions stabilized by the FBMA particles. Black dots are experimentally determined critical point of emulsion stability. The gray region refers to kinetically stabilized emulsions.*

water-oil interface using confocal fluorescent microscope in combination with the bright-field microscope. The FBMA particles accumulate at the contact point between two droplets and prevent coalescence of emulsion droplets , see Fig.3.11c, which would be the first step of eventual oil-water phase separation. This is clearly a different mechanism than the conventional steric barriers stabilization by solid particles (Fig.3.11a) and particle-bridging (Fig.3.11b). The spherical shape of droplets are retained when the droplets are in contact in our novel emulsions, whereas the slightly deformed interfacial regions are often observed in the case of the classical mechanisms. The particles at the contact point are not resolved at single particle level, probably due to the local dense packing of the particles. The rapid dynamical process of the particles' migration to the contact regions between droplets is not obtained due to the time resolution of our experimental setups and remains a challenge for future experiments. We can here only speculate about the driving force that pushes the particles to the contact point. This driving force must be considerate, since the coalescence of two water droplet that come in contact is a very fast process. We speculate that surface charge could play a role as the particles are highly charged, see below. The interactions with the approaching droplets would

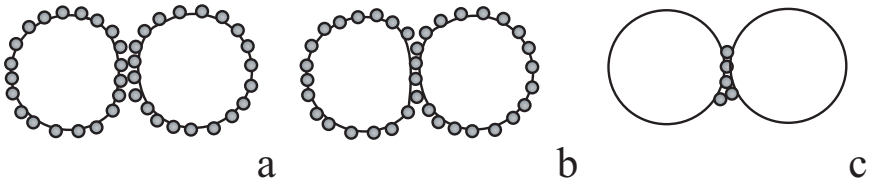

Figure 3.11: *Sketch of mechanisms of emulsions stabilized by solid particles, by forming bilayer stabilizaion (a), particle-bridging between droplets (b) and the novel contact point (c).*

then be long ranged, which is needed to have the particles in place at the moment the droplets make contact. The other question is how such small particles can prevent coalescence. Here the deformability of the particles might play a role, since there is little cross-linking in these polymer particles. It must be noted, however, that both features, the deformability and surface charge, are not typical for FBMA particles. The omni-phobic character of the particles most certainly plays a crucial role, as fluorenated particles tend to avoid any contact with bulk solvent.

The FBMA particles also prevent the droplets from wetting at the wall, therefore further hindering oil-water phase separation. Sedimented droplets can be stabilized by single fluorinated latex particles against wetting of the water phase at the wall, see Fig.3.3, and have a wetting angle of 180°. We also observed droplets with more FBMA particles are also stabilized by an accumulation of particles at the oil-water-glass three phase interface where some degrees of wetting occurs (Fig.3.7). We noticed that there are less particles at the top part of the droplet surface and the particles are still mobile, which can be speculated as the effect of the higher density of the particles 1.6 mg/ml, compared to the water and oil phases. At the bottom par and at the oil-water-glass rim particles are regularly spaced and immobile, probably due to the high surface charge. From the images stack in Fig. 3.7 we infer that the wetting angle for this examples is approximately 140°.

The macroscopic kinetic stability of the emulsions was studied over a period of 10 days. Unstable systems undergo a rapid phase separation (infinite droplet sizes), in contrast to the gradual increase of the droplet sizes in the kinetically stable emulsions. Our experiments did not allow observations of the 'limited coalescence' process, where rapid coarsening of emulsion droplets because of the 'missing' particles at the contact points between droplets takes place, typical for stable Pickering emulsions [80]. The two examples we for which we displayed the growth kinetics, see 3.9, exemplify that the transition between unstable and kinetically stable dispersions is very sharp and lies within a small variation of the particle

composition of 0.01%wt. Thus we could compose a well defined phase diagram of emulsion compositions 3.10.

The stability transition of emulsion droplets is considered in the light of particle coverage. The two critical concentrations can be compared when calculating the interfacial area per particle no. difference in the two, which can be used to calculate the overall particle coverage. The calculation can be obtained as the similar approach described in chapter 2, assuming the droplets have the same size distributions. The volume of the water in emulsions with W:O=1:2(b) is 12.5x times that of the emulsions with W:O=1:25(a). The difference in the interfacial area between both samples is then 5.4x. The difference in the number of particles at the critical concentrations 3.7x, which is quite close to the interfacial area difference of 5.4x. The deviation of the calculation can be caused by small differences in the size distribution of the droplets. When comparing the efficiency of the stabilization mechanism introduced here with the classical Pickering stabilization, we first note that for a sterically stabilized emulsions/forms, the liquid/liquid or liquid/air interface is covered fully with the particles. The particle compositions reported in the work of Binks *et al.* is up to 1%wt [76, 77], where a particle mass fraction of a maximum of 0.07%wt. The comparison is however somewhat arbitrary, because it depends on exact size distributions etc. Therefore we also make a simple calculation. For steric Pickering stabilization the minimum number of particles that is needed is calculated assuming a full surface coverage. Assuming an averaged droplet radius 5 μm, calculate the minimum number of particles $n_p = A_{collids}/A_{droplets}$ to be

$$n_p = \frac{A_{droplets}}{A_{colloids}} = \frac{4\pi R^2_{droplets}}{4R^2_{colloids}} \approx 530 \tag{3.1}$$

with $A_{collids}$ and $A_{droplets}$ as the total surface of a droplet and lattice area occupied by a particle. For $R_{colloids}$ we used the hydrodynamic radius of the FBMA particles of 380 *nm*. Thus the droplet stabilized by conventional steric hinderance of the colloids requires the minimum amount of colloids 530. In contrast, we observed the droplets stabilized by a few FBMA particles, which is 2-3 orders of magnitude less. Hence, the efficiency of the particles in stabilizing emulsions is quite impressive according to our experimentally determined phase boundary (shallow region in the phase diagram).

3.5 Conclusion and Outlook

Pickering emulsions (water in oil) were stabilized by the FBMA particles in this chapter, the cores of which were fluorescently labeled. The distribution of the FBMA particles in the emulsions was studied by confocal fluorescent microscope in combination with bright field microscope. The omniphobic particles were held at their thermodynamically preferred positions at the oil-water interface with the major potion wetted by the oil phase, which is preset by their wettability by the two phases. The emulsion droplets were stabilized by the particles against coalescence and wetting of the dispersed phase at the glass surface. The particles accumulated at the contact point between droplets or between droplets and glass surface. The experimental observations indicated the novel mechanism of the emulsion stabilized by our omniphobic particles, in which the least amount of particles was employed to stabilize emulsion droplets,see Fig.3.11c. The efficiency of the employed FBMA particles in stabilizing emulsions was at least two orders of magnitude higher than the other Pickering emulsions. Our studies have relevance to the improved efficiency of stabilization of emulsions stabilized by solid particles. The idea can be applied to avoid side effects of high percentage of the particles applied for conventional Pickering emulsions. For a deeper understanding of the novel mechanism it is however a prerequisite to record the particle accumulation process at the contact between two droplets, which must be an intriguing process given the rates that are involved. To capture this event, a fast confocal is needed in combination with an *in situ* mixing device.

4

fd Virus in Two-Dimensional Confinement

In this chapter, we study a simple case of confining the nematic phase in two-dimensional microchambers. The experimental system we used in the study is the lyotropic liquid crystals consisting of rod-like particles, the *fd* virus. The heights of these chambers were a few microns, much smaller than the "cholesteric pitch" of the particles [82]. Topological influences were explore in this chapter, including dimensionalities and geometries of the confinements, which varies from the circular to spindle-like shapes (elongated circular shape with two cups diametrically opposed).

Prior to the use of microfluidic droplets to study the three-dimensional structure of the nematic phase, we used in chapter 4 soft lithography to confine the nematic phase of *fd* virus in two-dimensional micro-chambers. The height of these chambers was a few microns, much smaller than the "cholesteric pitch" of the particles. We manufactured spindle-like chambers, mimicking in 2-D the shape of tacoids, the nematic droplets that form during isotropic-nematic phase separation. By systematically varying the size and aspect ratio of the chambers we found configurations predicted for 3-D tactoids as well as novel configurations. The transitions between the different states, as presented in diagram of states, were discussed in view of recent simulations.

4.1 Introduction

The peculiar shape and structure of nematic droplets that form during the isotropic-nematic (I-N) phase separation has been been observed for many systems. These so-called tactoids, named after their tactoidal shape, have been observed for both synthetic systems, such as vana-

dium pentoxide as observed in 1925 [9], as well as for biological systems, such as Tobacco Mosaic Virus as observed in 1936 [8]. Later on, many other lyotropic systems have shown to display a similar behavior, such as thermotropic organic liquid crystals [28, 29, 57, 83], *fd* viruses [34, 35], F-actin [11, 12, 14], and carbon nanotubes (CNT) [13].

Almost all studies were performed by using polarization microscopy. The shape of the droplets that are observed can be characterized by the cross-section of two overlapping circles which gives a elongated circular shape with two cusps diamatrically opposed with an overlapping angle α, see Fig. 4.1. The aspect ratio x of the spindle is defined as the ratio of the major axis $2R$ over the minor axis $2r$, see Fig. 4.1. During phase separation mostly small tactoids with high aspect ratio are observed in the beginning, which evolve into big almost spherical droplets. Polarization microscopy shows that the structure of the nematic director field within the droplets is mostly biaxial, which means that two point defects are located in the cusps, while the director line follows smoothly the contour of the interface. The homogeneous configurations, which possess parallel director lines in the director of the main axis of the structures, have only been observed for tactoids of CNTs [13], which are particles with extremely high stiffness. These tactoids had an aspect ratio of 4 with major axis up to 36 μm and an extremely low surface tension of the order of nN/m.

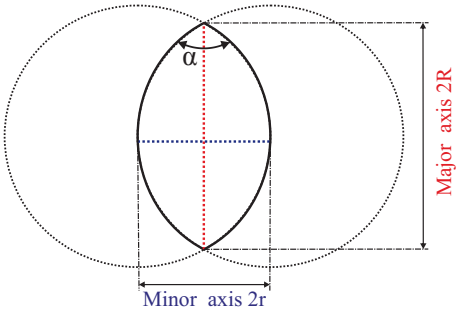

Figure 4.1: *Definition of the dimensions of a tactoid. [17, 18]*

The peculiar shape and internal structure of tactoids is determined by the elastic properties of nematic LC phase, the interfacial tension, and the anchoring conditions of the mesogens, and can be theoretically obtained by minimizing the total free energy of these three contributions. The weight of each of the contributions is determined by the exact properties of the mesogen. Considering the anchoring, it is known that colloidal rods, which are in the focus of this thesis, preferably align with the long axis parallel to the wall [84]. For such systems the formation of spindle-shaped structures that undergo a transition from a homogeneous director-field for small droplets with high aspect ratio to low aspect ratio droplets with bipolar structure is predicted [10, 17, 18, 85] as displayed in Fig. 4.2. Considering the stiffness of the rods, it

is known that the ratio between the bend elastic constant K_3 and the splay elastic constant K_1 increases with increasing stiffness. Kaznacheev *et al.* observed tactoids with bipolar director-field of very stiff inorganic mesogens, from which they could obtain the anchoring strength as well as the elastic constant ratios $K_3/K_1 \sim 10$. Considering the aspect ratio of rods, theoretical and computational studies showed that high aspect ratios of the rod-like particles lead to the formation of more elongated droplets [18, 86]. Since CNTs are known to be very stiff and long, this could explain the homogeneous director field in CNTs [13].

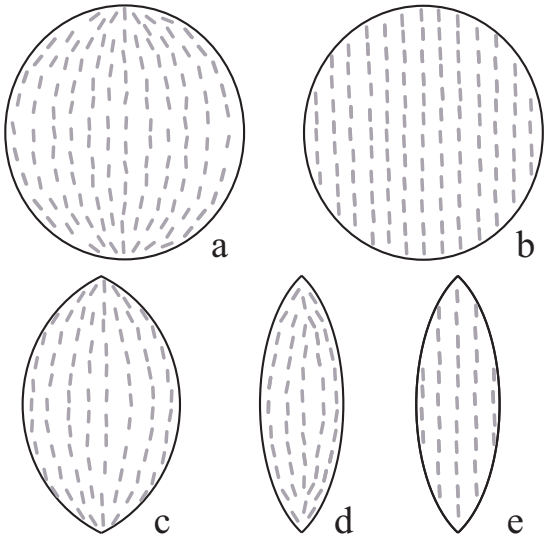

Figure 4.2: *Sketch of the expected configurations of the nematic director-field in two-dimensional microchambers.* ***(a)*** *bipolar and* ***(b)*** *homogeneous configurations in circular microchambers.* ***(c)*** *bipolar configuration in spindle-like microchambers with smaller aspect ratio x.* ***(d)*** *bipolar configuration in spindle-like microchambers with bigger aspect ratio x.* ***(e)*** *homogeneous configuration in spindle-like microchambers with big aspect ratio x.*

In almost all experimental studies, the shape of the droplet depends on the moment during the phase separation that the images is taken while the the relation between the shape of the droplet and the structure of the director field follows a path that is set by the energy balance described above. Thus, the system is in constant development and the structure of the director field can only be studied for a fixed range of shapes, namely from small high-aspect ratio droplets to big small aspect ratio droplets. In order to study the fully equilibrated structure of the nematic for all different shapes, it would therefore be advantageous to fix the size of the droplet, which obviously cannot be done during a phase separation process. Moreover, in the work of Prinsen and van der Schoot, explaining the transition of the homogeneous and bipolar

director-field of spherical and spindle-like droplets, the influence of the finite particle size and the possible twist deformation of the director-field are not taken into account.

One promising approach to simplify the complex three-dimensional confinement problem is to restrict the nematic LC phase to a shallow two-dimensional chamber. This is the approach we will follow in this chapter, varying the shape from spindle to circles. We suspect that the nematic director-field would be greatly influenced by the dimensionality of the confinement and the magnitude of the overlapping angle. Interesting work was done with two-dimensional confinements recently [87–89]. For example, F-actin were confined into cell-sized confinement. These filaments formed bundle-like structures and curved along the walls with the central bundles aligning along the chamber diagonal [87]. Using Monto Carlo simulations, hard rods in small circular cavities were studied by Heras and Velasco, from the dilute to high-density regime [88]. They studied the director-field with both planar to homeotropic anchoring conditions by varying the aspect ratio of the rods and the imposed confinement effect. In the former case, the director-field consisted, with increasing rod packing fraction, of an isotropic core with a nematic fluid shell adsorbed on the surface, a bipolar, and a quasi-uniform phase with two domain walls.

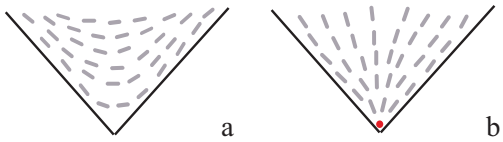

Figure 4.3: *Sketch of the splay and the bend deformation of the nematic director-field at the wedge:* ***(a)****. bend deformation and* ***(b)*** *splay deformation*

In our studies we will use *fd* virus, as it is the system that comes closest to Onsagers ideal hard rod, with its aspect ratio of 120 and persistence length of more than twice the contour length. The contour length itself lies with 880 *nm* almost in the range of length scales that can be achieved with micro-fluidics. Dammone *et al.* studied the possible director-field of a nematic liquid crystal phase at the wedge using rod-like *fd* viruses. They observed a splay-to-bend transition as a function of the wedge opening angle with "pseudo 2D" confinement at an angle of $70^\circ - 80^\circ$, as indicated in Fig. 4.3 [90]. This transition is set by the elasticity of the bulk liquid crystal phases and the anchoring condition of the nematic at the wall (Fig. 1.6 in Chapter 1). Based on the fact that the *fd* virus aligned tangential to the wall, it could be inferred from this transition that the ratio $K_3/K_1 \approx 1$ for these semi-flexible rods. Simulations

showed that for stiff rods, for which $K_3/K_1 \approx 10$ the transition takes places at an angle of $90° - 80°$, which has already been confirmed for *fd*-Y21M, a 5 times stiffer mutant of *fd*.

The competition of the elasticity of the nematic and the defined shape of the microchambers might pin down the transition from a homogeneous to a bipolar configurations of the director-field, with decreasing aspect ratio x of the microchambers, as predicted by theory [10, 17, 18]. On the other hand, as the angle at the tip of the 2-D tactoidal shape also changes with the aspect ratio of the droplets, we expect that a similar splay-bend transition as observed for the 2-D wedges of Dammone et al. [90], see Fig. 4.3. Moreover, when the spatial limitations increase and approach the size of the mesogen, finite size effects, where the continuum description with the bulk elasticity constants might break down. Using direct imaging of single labeled particles on the background of unlabeled particles we identified more classes of director field than could be expected on the base of present theory. We will therefore present a rich diagram of states and discuss the different transitions between the states.

4.2 Experimental Setup

Spindles are defined by the cross section of two overlapping circles. The boundary is set by the arcs of the overlapping region. The major axis of the spindle is set by the distance between the vertexes, while as the minor axis the distances between the centers of the arcs, see Fig.4.1. α represents the overlapping angle of the spindle-like shaped confinement, also referred as "angle of the wedge". In this way, we designed a mask where we varied the major axis of the spindles between 10-70 μm and the angle α between α = 180° ($x = 1$ and therefore a circle) and α = 30° ($x = 7.14$) in steps of 10°. This mask is shown in Fig.4.4. Microchambers were designed with a major axis of 10 μm, 20 μm, 30 μm, 50 μm, and 70 μm, respectively. In Fig.4.4a, series of microchambers were vertically placed in a matrix, in the order of the major axis length. In each series, two rows of microchambers were arranged. The corresponding aspect ratio increases accordingly from left to right, and from top to down.

Photo-lithography technique was used to prepare shallow microchambers. For later microscope observation, they were built up on top of clean cover slips by negative photoresist (SU-8, 2005, MicroChem). The first step of preparing the mask was to spincoat SU-8 on clean glass cover slips and went through two-step baking process (75 °C for 15 min, and 95 °C for 5 min). During UV irradiation, it was covered by a custom-designed mask printed on soda-lime glass (DeltaMask). Followed by another baking process (150 °C for 2 hours) the mask of SU-8 was

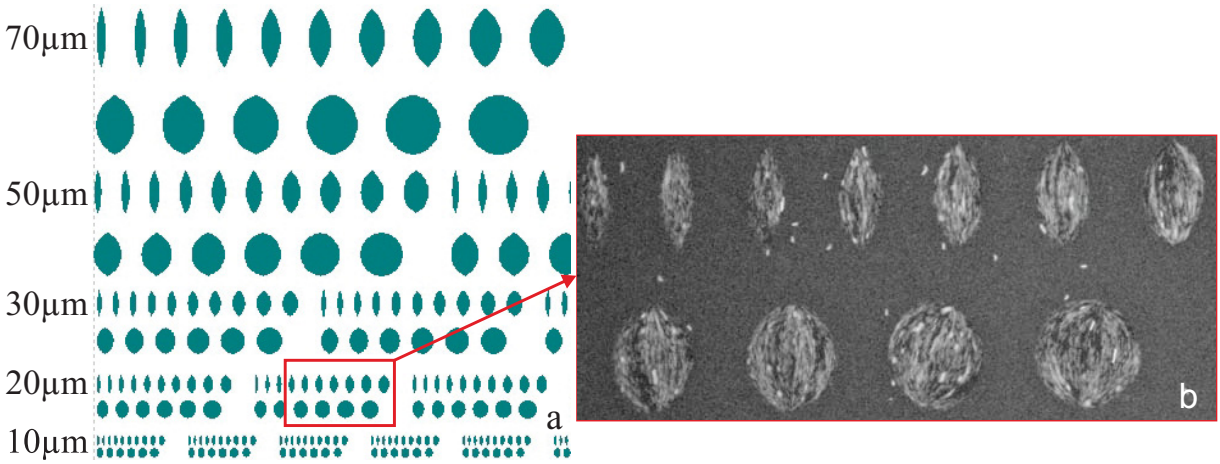

Figure 4.4: ***(a)****. Schematic representation of the glass substrate patterned with SU-8 microchambers, with gradually varied x from 7.14 to 1.00.* ***(b)****. Microscope image with 30 overlaid frames of region indicated in* ***(a)****. The major axis of the spindle-like confinement is 20 µm.*

completed. Microchamber with different heights were tested, for instance, 0.7 μm, 2.5 μm, 3 μm, and 5 μm. Due to the handling issues, "quasi-2D" microchambers with height of 3 μm were used for the following experiments. Prior to experiments, the microchambers were immersed within sample buffer containing 0.1 wt% of the amphiphilic block copolymer Pluronic F-127 (Sigma-Aldrich) in order to avoid non-specific adsorption of the material, as well as the drying out of the sample.

The rod-like particles being used here were the bacteriophage *fd* viruses. As introduced in the introduction chapter, *fd* virus is an ideal lyotropic liquid crystal model system for its monodisperse size and aspect ratio. Details are given in Chapter 1. These *fd* viruses were mainly prepared according to the work of K. R. Purdy [38]. The buffer used in this study was MilliQ water with 20 mM Tris pH 8.15, 100 mM sodium chloride, 15% ethanol. *fd* dispersions were purified and dialysised in several cycles prior to the labeling procedure. *fd* viruses were fluorescence-labeled afterwards with Alexa-488 succinimidyl ester(Invitrogen). The end concentrations of *fd* viruses was $C_{fd} = 24\ mg/ml$. This ensured the lowest nematic phase concentration, just beyond the isotropic-nematic coexistence phase at this ionic strength. In this case, the energy cost of the nematic phase to rearrange its director-field is relatively low, compared to the higher concentrated samples. The density of the sample at this concentration is low as well. The microchambers were filled by pipetting a drop of the *fd* virus dispersion and sealed by clamping a glass cover slip coated with a very thin layer of polydimethylsiloxane (PDMS).

A local "zoom-in" of the marked region (Fig.4.4a) was made and presented as an overlaid fluorescence confocal microscope image (Fig.4.4b). The fluorescence confocal microscope images were taken by a Nikon microscope with C1 confocal point scanner [91, 92]. The timelapse, consisting of 30 frames, was performed at a rate of 1 frame per 1-2 minutes. The resulting microscope observation indicated that all *fd* viruses in microchambers with different heights preferred a parallel anchoring at the x-y plane, see Fig. 4.5. The bright objects were the fluorescence-labeled *fd* viruses. The back ground was adjusted based on the averaged intensity of the 30 overlaid frames. One can see clearly the region of microchambers because of the densely packed particles. The particles with higher intensities were either out of their confinements, or they were immobilized particles sticking on bottom of the confinements. This was mainly due to the overlaid intensity overlay process. In the later analysis, only the confinements being completely filled with particles were studied, in order to avoid the misleading local void information.

4.3 Image Analysis

The images were analyzed by two different approaches. The first approach is based on single particle tracking, using a modified version of an IDL tracking routine [93]. It was specially designed to identify the location and orientation of single particles. This information was used to generate an orientation map, giving the director structure. The variation of the orientation angles was very well presented by the gradually changed gradients of the colors. The local brightness referred to the coherency of the particles' intensities. The distribution of the local orientation was clearly shown by the encoded color of each region of interest.

An alternative analysis was performed by a free plugin of "ImageJ", the so called "OrientationJ", which quantifies the orientation of features, based on the gradient in the intensity of the feature. It was originally developed to find the local orientation of collagen fibers and the isotropic properties (coherency and energy) of every pixel in the image [94]. It worked also very well for our data when the overlap of all images was processed, such that the features basically are the traces of the rods. With the help of "OrientationJ", the axes and defects can be easily found. However, the drawback of it was that the local orientation of each single trace was not very well represented, due to the overlaid information. We used it mainly to get the general information about the local orientation of our rod-like particles and to compare with the single particle results.

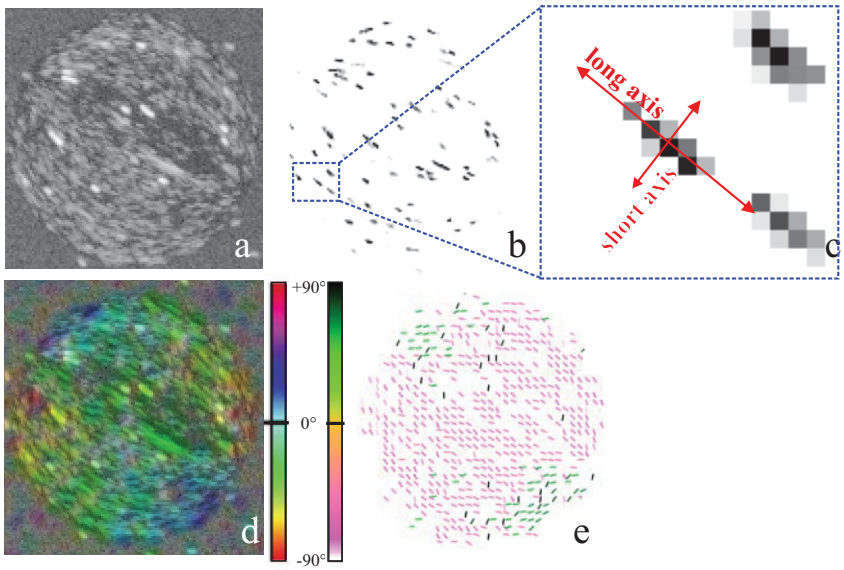

Figure 4.5: *The typical overlaid structure by 30 overlaid images formed by fd virus in circular 2D confinement with diameter of 30 µm,* ***(a)****. The inversed image of fluorescence confocal microscope single image frame of the fd viruses with in microchamber,* ***(b)****. A schematic representation of the long axis and short axis of identified single fd virus taken from a small region,* ***(c)****. fd virus are colorcoded by their orientations , which were analyzed with OrientationJ,* ***(d)****. The colormap is shown on the right of the image. The director-field of the virus analyzed by IDL,****(e)****. The color of the rods represent the local orientation of the viruses encode with the green-pink colormap on the left of the image. Orientation angles are indicated for both colormaps,* ***(d)*** *and* ***(e)****.*

In Fig. 4.5, we present the results analyzed by the above mentioned image analysis methods. It is a typical example of fluorescence-labeled *fd* viruses in 2D confinement in a perfect circular microchamber with diameter of 30 μm, which means that the diameter of the example was roughly 30 times the rod length. The resulting director-field displays as a circular bipolar structure. To obtain the boundary of the confinement and the distribution of the *fd* virus in the confinement, an overlaid microscope image with 30 single frames was used, as indicated in Fig. 4.5a. An axis can be drawn, which connects the two poles of the circle. The structure was axisymmetric. The axis of the structure was making an angle of 45° with respect to both the x and y axes of the images. In Fig. 4.5b, a single original fluorescence confocal microscope image of *fd* viruses with inverted color table is shown. The director-field of the viruses was obtained by the tracking the diffusion of labeled *fd* virus. A zoom-in of a small region in Fig.4.5b is shown as Fig.4.5c. The long and short axis of the labeled virus is shown in red.

The overlaid microsocpe image was analyzed by "OrientationJ". The features with a certain orientation were encoded by a rainbow color map. The corresponding orientation angles were indicated by the individual encoded color, in the order of a rainbow color map, see Fig.4.5d. The axis of the director-field (in green) refers to $-45°$. The blue color only showed up next to the poles (defects) as an indication of rods with orientation of 40° - 45°, in the second and fourth quarters. In a clockwise manner, the cyan, green, yellow and orange subsequently appeared along the contour of the confinement.

We further analyzed the overlaid microscope image Fig.4.5a with IDL. The analyses based on IDL is very helpful when we need to identify the position of the defects. For a better contrast in color, the orientation of the particles going through a transition respect around 90° can be easily distinguished according to the colormap on the left of the image, see Fig.4.5e.

4.4 Results and Discussion

In this part, we start with the listing of our observed classes of director-fields, including the theoretical predicted structures and novel structures. Then we sketch a rich diagram of states on the basis of the length of the major axis and the overlay angle α, which is proportional to the aspect ratio R/r of the microchambers. We finish this section with discussions of the transition of the states.

4.4.1 Identification of Director-fields

The behavior of the director structures we find for the range of aspect ratios and sizes is more complex than we expected, 4.2 (Fig. 4.2). The director-fields we observed can be categorized based on the symmetries of the director-field, types of deformation at the overlaying angles (wedge), number of defect points in the structures, and their locations. Each category of director configurations is given a short abbreviation. We found that the shape of the director-field depends on both the dimensionality and overlay angle α of the microchambers. The categories of director-field are categorized in Tab. 4.1.

The listed first five classes are often found in the smaller microchambers (at lease with a short minor axis), while the "M" class is found in larger microchambers. The director-field configurations ("B","D**", "D*", and "S") all have with two defect points. The defect points were found in combination with splay deformations, and they were not necessary located at the vertexes of the wedges. The "D*" is mostly found at slightly smaller α than the "D**". The difference of these two configuration is that in the "D*" configuration one defect is located at the casp.

The other novel "S" configuration appeared directly after the "D**" configuration and some of them accompanied the "D*" configuration as well, for the α approximate 100°, see Fig.4.6. It is named after the director lines displaying a S-shape. The distribution of this "S" structure an be only found in a narrow range of angle α ($90^\circ \leq \alpha \leq 130^\circ$). All above mentioned structures were stable with time. This means that they were stable or metastable states.

4.4.2 The diagram of states

Having identified all different configurations we now set up a diagram of states plotting which states we find as a function of the major axis $2R$ and the aspect ratio x. For small confinements, the trend is as predicted by Prinsen and van der Schoot, see Fig. 4.2 [17, 18]. For larger confinements we find novel structures. The regions where the new structures are found are highlighted by dashed lines, respectively for "S" structure and "D" structure. Both the novel "D**" and "D*" configurations are referred as "D" in this diagram and will be distinguished in the later part of this section.

Abbreviation	Structure	Director-field sketch
B	Bipolar configuration with two point defects sitting diametrically opposed at the poles in circular or spindle-like shaped microchambers. The director lines are on average parallel to an axis which connects the defect points. The director-field presents splay deformations at the wedges and bend deformations close to the arcs.	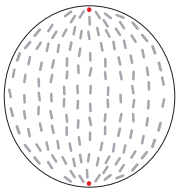
D^{**}	Configurations with two point defects located at the side wall in spindle-like shaped microchambers. The director-field presents the splay deformations around the defect points and bend deformations in the wedge.	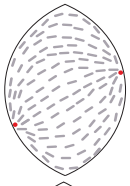
D^{*}	Configurations with one point defect at the pole and the one at the side wall in spindle-like shaped microchambers. The director-field presents both the splay and bend deformations at the wedges.	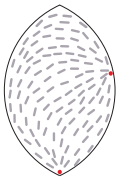
S	Configurations show structural chirality with two point defects at the vertexes in spindle-like shaped microchambers. The director lines in this configuration are "quasi-uniformly" aligned, with a central domain tilted either upper-left or upper-right respect to the major axis of the microchambers. The director-field presents the splay deformations twice at the wedges.	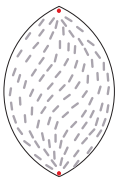
H	Quasi- homogeneous director-field with director lines parallel to the major axis of the microchamber with no defects. It could also be a quasi bipolar director-field, "B", with the defects remain outside of the boundary, see Fig.1.8.a.	
M	Multi- defect points and domains in larger microchambers	Complicated director configurations with many possibilities

‡ Notes: "$*$" here indicates number of defect points located at the arcs.

Table 4.1: *Table of states of the director-field.*

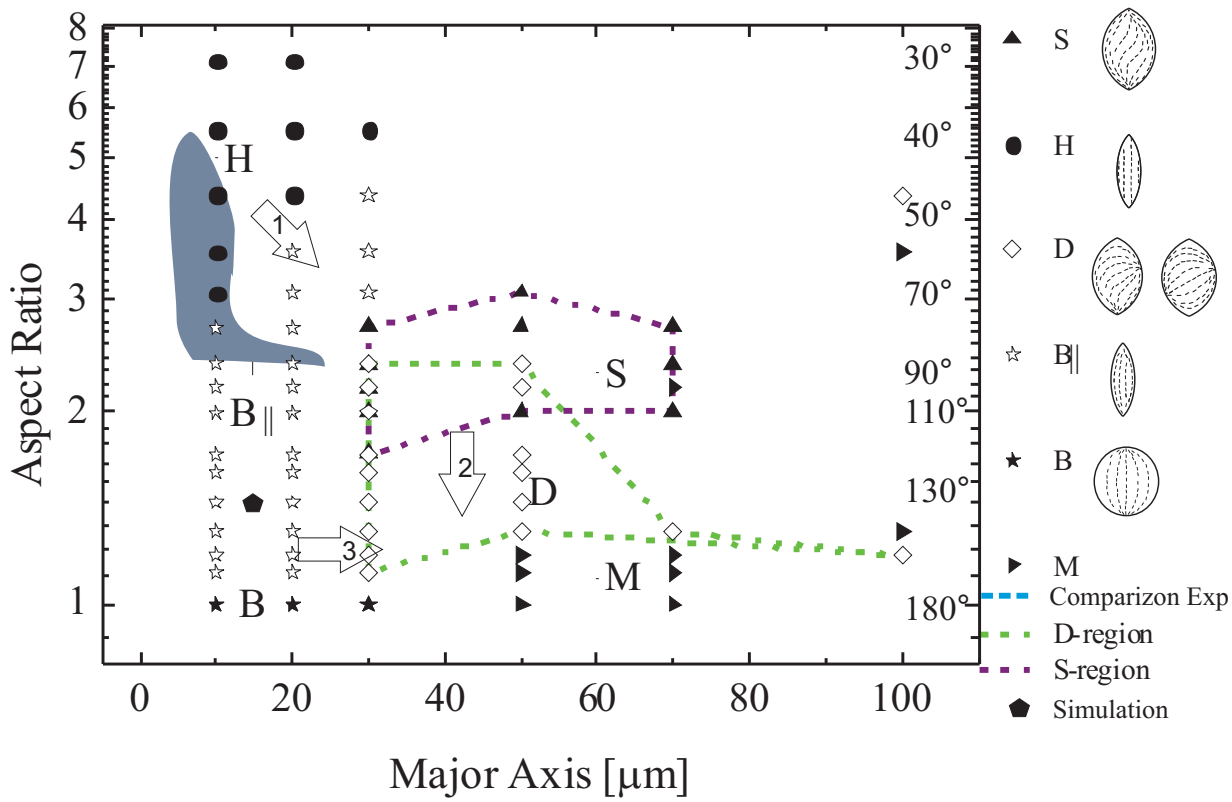

Figure 4.6: *The diagram of states of fd viruses in 2d confinement for which $K_3/K_1 = 1$. The left vertical axis is the aspect ratio, which is proportional to the overlaying angles marked on the right vertical axis. The location of D is outlined in green, with the overlaid region with the location of the S states labeled in purple. The numerical simulation data is marked with a filled polygon, taken from Ref. [96]. The gray region is marked, where the data from fd tactoids locate. The transitions of the states will be presented later are indicated by arrows marked as 1-3.*

4.4.3 Transitions in the diagram of states

In the diagram of states we can identify three different transitions of the director-field states, which we mark with arrows 1-3. The transitions are related to the crossing over from a homogeneous to a bipolar director-field configurations, the transitions from "D" to the "S" configurations, and the transition from "B" to "M" states, respectively. We find that the degree of complexity is influenced by the dimension of microchambers.

The first transition of the director-field configurations from a homogeneous to a bipolar, indicated by arrow 1 in Fig.4.6, takes place in the relatively smaller microchambers (and $2r/a$). For microchambers with the major axis of 10 μm and 20 μm, a transition of director-field from

quasi homogeneous "H" to the bipolar "B" states takes place. Moreover, the transition takes place at smaller aspect ratios with reducing the length of the long axis $2R$. We notice the curvature at the wall of the "H" might almost not be felt by the particles in this case, because the $2r$ is only up to 5 rod length.

Our two-dimensional approach of confining nematic director-field is comparable with the results based on experimental observed tactoids by Dogic [95]. These tactoids were formed by *fd* virus and the polysaccharide dextran with spindle shapes. The aspect ratios of the tactoids are in the range of 2.5-5.5, with comparable long axes 10-20μm. The location of which is marked as gray in our diagram of states. Their data suggested the deformation of the nematic director-field overrides the surface energy at this length scale of 10-20μm in the 3-D problem. The spindle-like shape of the tactoids is comparable with our 2-D approach where we found the crossover of the states from "H" to "B", when the imposed geometry of the confinement is absent. In the theoretical work of Prinsen, they observed the "B" director-field configuration of the droplets taking the elastic stiffness of the director-field and the anisotropy of the interfacial tension into account [17, 18], and they predicted "H" configuration in the smallest droplets. We notice that the theory and experiment in the 3-D approach agree only qualitatively to our 2-D results.

In the second transition, indicated by arrow 2 in Fig.4.6, we observed that the director-field confined in bigger microchambers (start with 30 μm major axis) present the novel states, e.g."D**" , "D*", and "S", instead of a simple "B". By decreasing length of the minor axis, the configuration "B", "D**" , "D*", "S", "B", and "H" structures show up in a order, noticing the overlapped region between "D" and "S". It is difficult in this case to draw a clear boundary between the different configurations. In order to characterize the structures of the director-field, it is important to know the locations of the defect points. To do that, a "drift" angle β is defined for both "D**" and "D*" configurations, based on the direction of the major axis.

For "D**" director-field, the angle β is defined as the angle between the line (l) connecting the two point defects and the major axis of the confinement. It was schematically presented in Fig.4.7b. Additional, the line connecting two point defects do not necessarily need to pass the center of the confinement. We also show in Fig.4.7c the "D**" director-field predicted by Mulder *et al*, by Monte Carlo numerical simulations (private communications). They predicted this structure formed by hard rods with the major axis of the confinement of 15x longer than the length of the mesogens, with the aspect ratio x of the confinement of 1.5, and the aspect ratio of the mesogen of 20.

For "D*", the drift angle is defined as shown in Fig. 4.7e. β is the angle between major

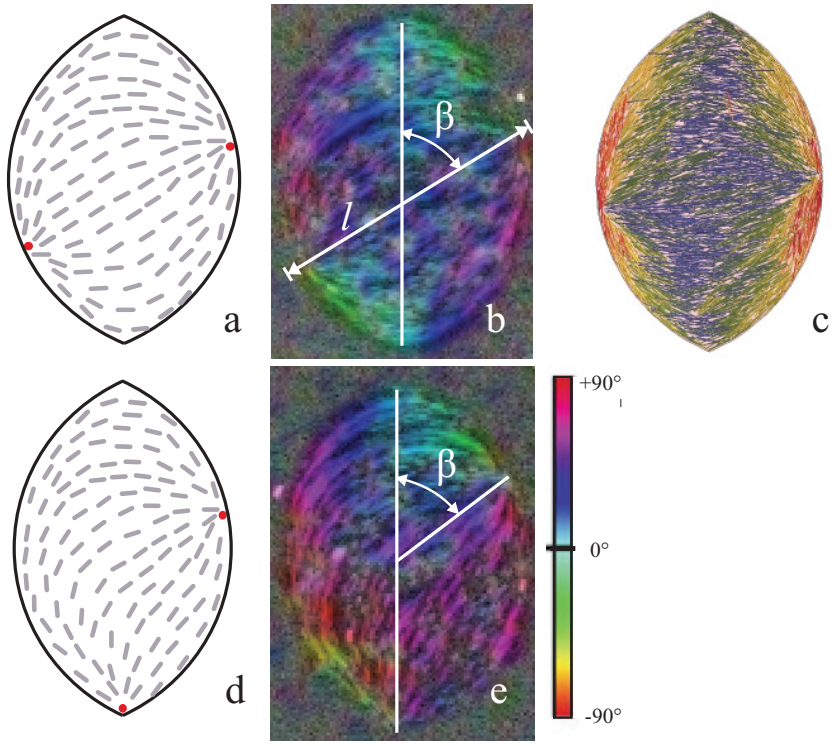

Figure 4.7: *The sketch of angle β defined for the "D**" **(a)** and "D*" configuration **(d)**. The drift angle of the point defect(s) away from the major axis based on the overlaid microscope images with the color coding, **(b)** and **(e)**. The color lookup table was indicated on the right. The examples were taken from confinement with major axis 30 µm with x of 1.3 and 1.4, respectively. The predicted state of director-field by numerical simulations, with x of 1.5 is shown in **(c)** [96].*

axis of the microchamber and the other line, which connects the point defect located at the side wall and the center of the microchamber. As an example, we plotted the drift angle of the defects away from the confinement's major axis in microchambers (Fig.4.8).

Based on the results shown in Fig. 4.8a, we find a gradual crossover from a "D**" to "D*" with decreasing α. The transition takes place in a broad range of α ($160 - 120°$). For microchambers with "D**" and "D*" configurations angle β increases with increasing α. As indicated in the figure, the distance l between the "D**" configuration varies with respect to the change of α. To emphasize the variation of the l, the lengths are labeled directly in Fig.4.8a. However, the change of l is only about a few rod lengths. The system tends to maintain the length of l by decreasing "drift" angle β, when l seemed to be at least 20 times the length of the rod-like particles in the microchambers with major axis of 30μm. The angle β and distance l are also plotted as function of the major axis $2R$. The microchambers in this plot

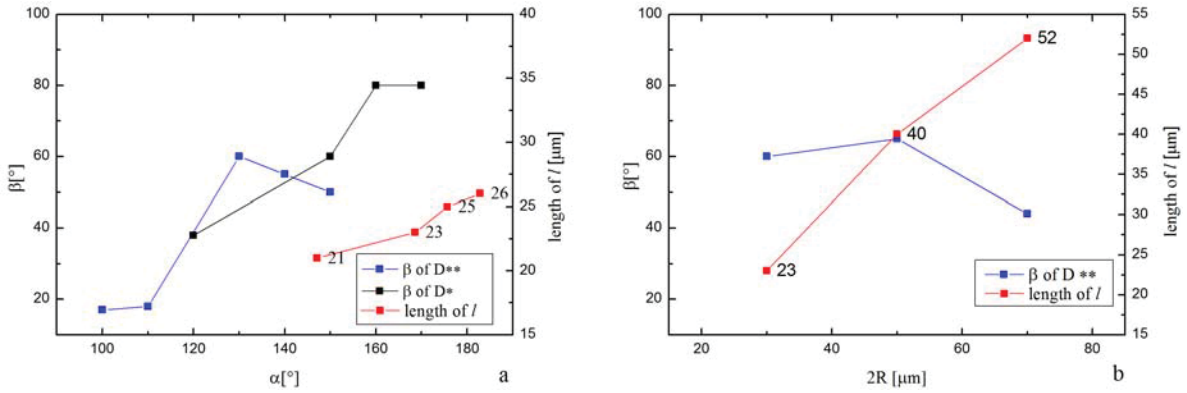

Figure 4.8: *Drift angle β and distance l connecting the two point defects in the "D**" configuration. The symbols refer to the experimental results.* ***(a)****. Drift angles β of D** (blue) and D* (black) configurations as a function of overlaying angle α for microchambers with major axis of 30 μm. The distance l between the defects in "D**" configuration is plotted against the angle α as well (red).* ***(b)****. The β (blue) and distance l (red) as a function of the microchamber major axis 2R.*

have the same angle $\alpha.\beta$ is quasi constant, according to the data in Fig.4.8b, while the length of l obviously increased with increasing size of microchambers.

The transition of the states from "D" to "S" takes place with decreasing α (increasing x). The "S" configuration shows up in region of $80^\circ \leq \alpha \leq 120^\circ$. The "S" is not due to the chirality of *fd* virus since the chirality of fd is indeed suppressed due to the limited height of these shallow microchambers, 3 μm. We speculate that the "S" structure is formed due to the packing of the rod-like particles, as also reported by Tortora *et al* [25]. In "S" state, both two point defect locate at the cusps.

We start our discussion now for the "D**" and "D*" states because of their partially similar symmetries and neighboring positions (in Fig.4.8). We know that the wedge opening angle α might influence the distortion of the director-field at the wedges, as reported by Dammone *et al* [90]. The bend and splay deformation of the director-field at the wedge transits from a bend deformation to splay deformation. Dammone *et al.* [90] identified a splay-to-bend transitions at $70^\circ - 80^\circ$ opening angle. They estimated the elastic stiffness of the semiflexible fd virus, with the $K_3/K_1 \approx 1$. We observed the bend-splay transition at the casps in a boarder range, owning to the coexistence "D**" and "S" configurations, see Fig.4.6. Our observations agree qualitatively with their results. It is partially due to the different geometries of the wedge + channel and our spindle-like shaped microchambers. The dimension of the wedges (minimum height of 75 μm, depth 10 μm) is larger than ours. We speculate that the reason that our bend-to-splay transition takes place in the broader range of the opening angles than their work is the

more confined 2-D microchambers, in contrast to the wedges. Our finding is also confirmed by numerical simulations, where they find the "D**" for the hard rods, Ref. [96]. It is not yet confirmed if the states of "D**" is the equilibrated state, due to the extended equilibration time. They also found "D*" state, which is found to be an intermediate states during the settling of the nematic director-field with the end stage of "B". The size of the confinements is can be related with the driving force for the structure to settle. The smaller the confinements are, the shorter time needed for the director-field takes to settle. It suggests the free energy difference of the intermediate state "D*" is small, compared to the equilibrated "B" states.

The third transition from "B" to "M", the arrow 3 in the diagram of states, takes place in confinements with major axis $2R \geq 30$ μm. Hereby, an example is given for microchambers with aspect ratio $x = 1.19$. The director-fields within microchambers of major axis of 10 μm, 20 μm, 30 μm, 50 μm and 70 μm are showed in Fig. 4.9a-e. The director-field with a bipolar structure "B" with orientation angles of the fd virus in the range of $45 - 135^\circ$ is found in microchambers with major axis of 10 and 20 μm, see Fig.4.9a and b. When the size of the microchamber increases, we observe the local homogeneous director-field sets in the core region of the microchambers. The director-field formed two bend deformations at the wedges, see Fig.4.9c-e. The "D**" state with the variation of the particle orientations is indicated by the color change from green to pink. The "M" configuration appears with formation of defects and nematic domains(Fig.4.9d and 4.9e.

We display the dependence of the director-field states on the aspect ratios x in microchambers with the major axis of 50 μm in figure 4.10, in which the states of director-field change from a "D**" configuration (Fig. 4.10c) to a "M" configuration (Fig. 4.10b-a). A characteristic feature from Fig.4.10c to b was that the director-field, instead of following the wedge ($\alpha = 160^\circ$) at the bottom of the image, flipped over and a point defect formed at the bottom of the boundary with strength of +1/2 and another defect with strength -1/2 in the confinement. The new wedge disclination appeared where the color red-green-cyan met in Fig.4.10b. As a consequent, the other opposite point defect with strength +1/2 drifted to the upper position at the wall. When the $2r$ ($2r/a$) increased further (from Fig.4.10b to a), the point defect on the left with strength +1/2 drifted upwards. We also found the state of director-field within circular 50 μm confinement was with only with two defects from the Fig.4.10. The difference in minor axis $2r$ of the three microchambers is only around 2.5 μm.

For $2R$ = 50 μm, 70 μm, and 100 μm, the situation is more complicated. The influence of aspect ratio x, the angle α and the minor axis S were important and combined. The general tendency of getting certain director-field configuration is similar as the microchambers with

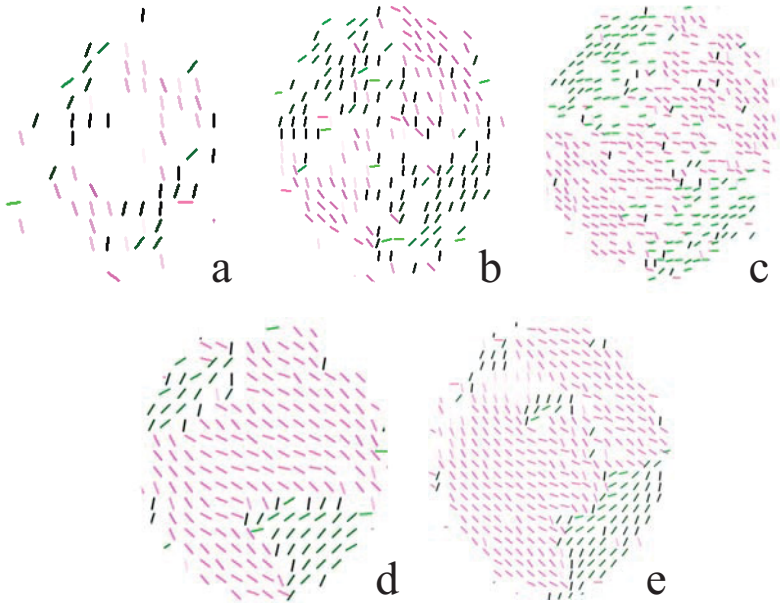

Figure 4.9: *Directer field of fd virus in confinements with fixed aspect ratio 1.19 and increasing major axis length:* ***(a)*** *10 µm,* ***(b)*** *20 µm,* ***(c)*** *30 µm,* ***(d)*** *50 µm and* ***(e)*** *70 µm.*

30 μm, except the multi- defects "M" configuration. The director-field is clearly less spatial confined ($1 \leq x \leq 1.19$, $L = 50$) compared with the previous case. While, we suspect that the range of "M" configuration is much larger than the case of 50 μm. Because the length of minor axis $2r$ is also much larger for the confinements with major axis 70 μm, and 100 μm, with the same aspect ratio x.

4.5 Conclusions

We studied the influence of 2-D confinement on the structure of the director-field, which was employed as a 2-D simplified model to mimic the structure of tactoids during the phase separation of lyotropic liquid crystals, in particular the monodisperse *fd* virus. The microchambers are with a spindle shape and 3 μm thick, varying the aspect ratio between 7.14 and 1, which corresponds by changing the angle at the tip between 30 and 180°. In this way, we studied the finite size effect, when the confinement becomes of the same order as the mesogen. We used nematic dispersions of *fd* virus close to the isotropic-nematic phase transition. The resulting configurations were a consequence of the competition between the elasticity of the nematic phase and the preferred tangential anchoring of the rods.

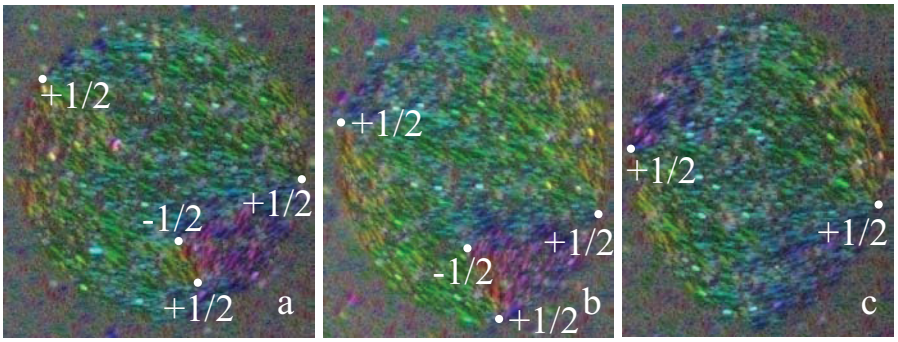

Figure 4.10: *Formation of multi- point defects with decreasing aspect ratio:* ***(a)*** *1.12,* ***(b)*** *1.19, and* ***(c)*** *1.30. The examples were given within confinements with major axis 50 µm. Defect points were indicated as white dots and labeled with strength.*

We found configurations predicted for 3-D tactoids as well as novel configurations, which are presented in a diagram of states. As expected we observed the transition of the distorted director-field from a "B" to "H" configuration with the high aspect ratio of microchambers, $x \geq 3$ where we expect the finite size effect.

The novel configurations ,"D**" , "D*", and "S", were observed, see Tab.4.1. The director-field ends either with bend + bend, or bend + splay deformation in the wedges of the microchambers, accompanied with the formation of defects along the arc. The transition between "D**" , "D*", and "S", is a rather smooth and continuous process ($80^\circ - 170^\circ$). It is therefore, difficult to draw a sharp transition line between these structures. Even though Dammone *et al.* found the transition angle $70^\circ - 80^\circ$ from the splay to bend deformation for the director-field at the wedges and their work was based on similar systems but with different experimental settings. In our study, the director-field with rich behaviors is spatially more confined and the band-splay transition takes place at bigger angles. The estimated elastic stiffness of the *fd* virus with $K_3/K_1 \approx 1$ of their work is probably comparable to our expectations.

We also observed the confinement effect. The resultant director-field starts from the bipolar "B" structure in smaller circular confinements and ends with multi- nematic domain formation. The director-field starts locally with slight flips. The small local stress accumulates and leads to the formation of local defects. The influence of these stress propagated slowly over the whole confinement and gradually leads to stable configurations. We speculate that the 'core' of the structure is in relation with the nematic domain size of *fd* virus.

This part of the work is a preliminary exploration of the problem. We could not conclude sharp transition lines between different configurations due to the limited information and the

overlapped region between different director-field configurations. However, one can still find a clear trend of configurations in each region of the phase diagram.

5 *fd* Virus in Three-dimensional Droplets

The director-field configuration of the chiral nematic liquid crystal (LC) phase in three-dimensional confinement is studied in this chapter. We employ microfluidics to produce monodisperse droplets containing the nematic dispersions of *fd* virus surrounded by a carrier oil phase, while we vary the size of the droplet as well as the concentration of the virus. The resulting director-field within the droplets is studied at the single-molecule level, using confocal microscopy. The results are linked to polarization microscopy observations. We find a ring structure evolving in the polarization images with increasing size and concentration which we attribute to a cholesteric twist of the director-field. We confirm, using the single particle data, that indeed such a twist is present in a non-trivial way. The twist is non-monotonous throughout the droplet and much smaller then observed in bulk. Thus, confinement suppresses the cholesteric twist.

5.1 Introduction

Tactoids, which form during the isotropic-nematic phase separation, are mesoscopic nematic droplets. Their peculiar shape and internal structure is determined by the elastic properties of nematic LC phase, the interfacial tension, and the anchoring conditions of the mesogens, and can be theoretically obtained by minimizing the total free energy of these three contributions. The weight of each of the contributions is determined by the exact properties of the mesogen. In chapter 4 we already discussed that for colloidal rods there are strong anchoring conditions, such that the rods will tend to align with the wall. This surface anchoring in combination with the Frank elasticity constants, which describe the elastic properties of the nematic phase, result

in structures as complex as those described in chapter 4. Another feature of many lyotropic LCs is that the mesogens are chiral. This intrinsic chirality results in a chiral strength which induces a twist of the director-field, described by the polar angle θ, as illustrated in Fig. 5.1. This twist is irrelevant in a two confinement, but very relevant in 3-D confinements. The question is how the twist can be accommodated in such a confinement, strong at the wall and decaying as it moving away from the wall. Moreover, most experimental work on the determination of the director-field configurations of nematic droplets concerns tactoids during the phase separation process [10–12,28,29,57,83,85]. In these studies, the shape of the droplet always depends on the moment during the phase separation that the images is taken and there is a fixed relation between the size of the droplet and its aspect ratio. As in chapter 4, it is advantageous to study the fully equilibrated structure by fixing the size of the droplet, which obviously cannot be done during a phase separation process. In Chapter 4 we fixed the shape of the droplet and confined the colloidal rods in different 2-D confinements. In this chapter we do not fix the shape, but we fix the volume of the droplet, using the microfluidic device introduced in chapter 2 to produce monodisperse droplets of variable size. This procedure now allows, in contrast with the 2-D confinement, to study the effect of the chirality of the mesogen, which is an intrinsic property of many colloidal rods.

Theory based on Frank free energy was developed to predict the structure of the director-field for chiral nematic droplets [21,22,97]. This structure can be generally described as

$$\mathbf{n}(\Theta,\Phi,R) = f_1(\Theta,\Phi,r)\,\hat{e}_\theta + f_2(\Theta,\Phi,r)\,\hat{e}_\phi + f_3(\Theta,\Phi,r)\,\hat{e}_r, \tag{5.1}$$

where the spherical coordinates (Θ,Φ,R) indicate the position in the droplet and the local director-field $\hat{n}$, given by the directions $\hat{e}_{\theta,\phi,r}$, see Fig.5.1a and b.

Structures which are much more complex configurations than the biaxial and homogeneous structure, as introduced in Chapter 1 were found, both experimentally and from theory, such as diametrical spherical, radial spherical, 'twisted bipolar', planar bipolar, and Lyre and Yeti structures. In Fig.5.1 c and d we show a few of the most prominent structures, including the polarization images which always show a ring structure, indicating a local pitch, superimposed on complex background. The stability of these configurations vary for different ratios of cholesteric pitch sizes and diameters of droplets. The 'twisted bipolar' director-field is stablest for large pitches, $p_0 \geq 4R/3$, where R is the radius of the droplet. 'Twisted bipolar' differs from the bipolar director-field formed by nematic phase in twisted director lines around the symmetry axis.

Interestingly, it was recently found that macroscopic chiral structure can be formed in confinement, even when mesogens are achiral. Totoral and Lavrentovich studied tactoids formed by achiral LC in molecularly nonchiral aqueous solutions [25]. They found that the chirality induction was a replacement of the energetically costed splay packing with twisted packing. Niori *et al.* showed that macroscopic chiral domains are formed by achiral LCs with banana shapes, due to the packing of these mesogens [98]. Hough *et al* found that bend-core shaped achiral molecules formed periodic arrays of helical filaments because of the spatial limitation of layering [99].

So far, the studies of nematic/chiral nematic director-field in spherical geometry were carried out based on polarization microscope observations, although theory and computer simulations predict detailed director-field which cannot unambiguously be confirmed by this technique. We explore in this chapter the influence of confinement on the alignment of chiral nematic LC phase at the single-molecule level, exploiting the colloidal length scale of the *fd* virus which we use in our study. We first construct a diagram of states indicating transitions between on and two rings in the polarization images as a function of droplet size and concentrations. We then determine in 3-D the director-structure with confocal microscopy, where we directly measure the rotation in the director locally.

5.2 Methods and Experiments

5.2.1 Sample Preparation

The experimental system used in this chapter is *fd* virus dispersed in a TrisHCL buffer (20 mM) with pH 8.0. Initially very diluted *fd* virus dispersions are prepared and centrifuged. Only the upper part of the pellet is carefully re-dispersed by freshly prepared buffer in order to avoid the presence of any residual bacteria, which might influence the structure of the nematic director-field. The concentration of the final virus dispersion is determined spectroscopically by NANODROP (Thermo Fisher Scientific Inc.). The samples of *fd* virus are prepared directly before every measurement. A separate batch of *fd* virus was labeled with Alexa Fluor® 488 (Alexa Fluor® 488 5-TFP, MW of 884.91 mg/mol, Intitrogen™) for single-molecule observations, using the method in the work of Purdy [38]. The fluorescently labeled rods are mixed at a small volume fraction (1-2%) with unlabelled rods, to act as tracers to reveal the director field. The further procedure of the droplet preparation is described in chapter 2.

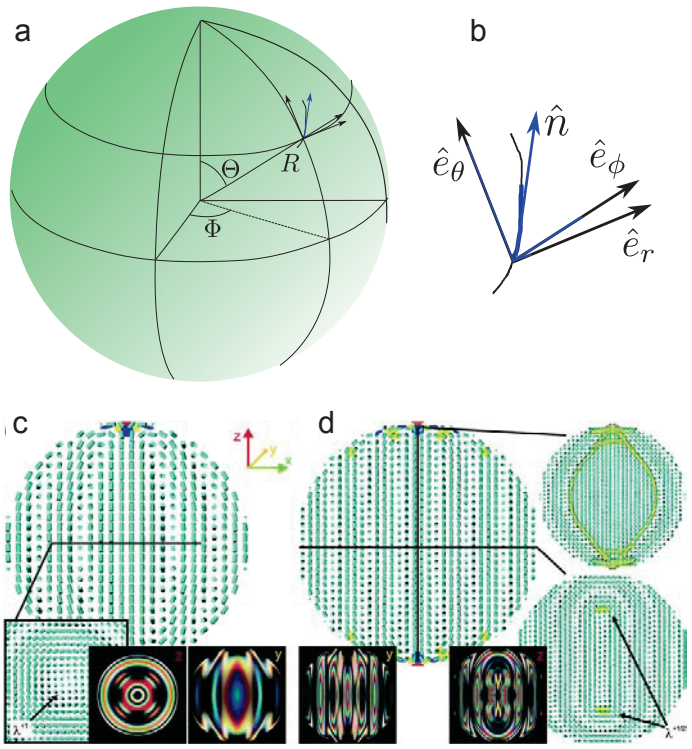

Figure 5.1: *(a) Definition of the angles defining the location within the droplet* (Θ, Φ, R) *and (b) the director* $\hat{n}$ *with the different components* $\hat{e}_{\theta,\phi,r}$*. (c) and (d) show a bipolar structure with a cholesteric pitch and a planar bipolar structure as taken from Ref. [21].*

5.2.2 Microscopy

The samples were studied by polarization microscope Zeiss Axioplan 2 with Plan-Neofluar objective, 40x, NA=1.3. The single molecule experiments for the determination of the cholesteric pitch were performed by Axiovert 200 equipped with a fast scanning confocal unit (VisiTech "VT-Infinity") and ANDOR $iXon^{EM}$897 camera, LCI Plan-Neofluar objective,Gly./W, 63x, NA=1.3. The exposure time was 100 ms, which allows the labeled *fd* to diffuse in the background of unlabeled chiral nematic phase. This setting was also partially employed to investigate the chiral nematic phase director-field confined in droplets, by an averaging of 5x. We also used LSM 510, equipped with the single-pinhole confocal unit, at 1.93 frames per second to study the frustrated director-field in droplets. This does not only improve the contrast, but in addition the rods will diffuse during the exposure time following the director-field, such that full trajectories are recorded, which mimic the line of the director-field.

We determined the cholesteric pitch of the fd virus in the bulk phase at a concentration of 60 mg/ml and an ionic strength of I = 10 mM. We present the characterization of the cholesteric

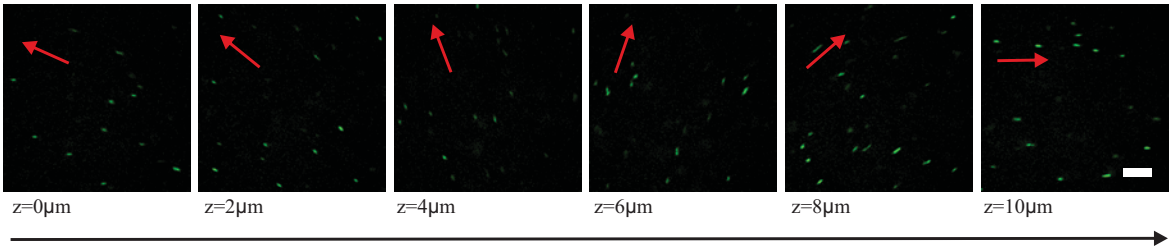

Figure 5.2: *Confocal scan of a fd virus dispersion at a concentration of 60 mg/ml. The green rod-like particles are single fluorescently labeled particles, which are used to determine the orientation of the director field, indicated by the red arrow. The Scale bar is 20μm.*

pitch as obtained by confocal microscope in Fig.5.2. The variation of the cholesteric pitch is 16° over the length of 1 μm, we measure a cholesteric pitch size of 22 μm. Our result agrees with the cholesteric pitch as measured for this fd concentration and ionic strength as determined by Dogic *et al* [82].

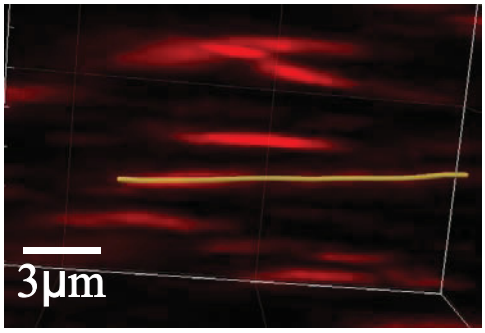

Figure 5.3: *A fitted trace after manually selecting the trace with the help of auto-depth function of IMARIS, with the raw data in the background.*

5.2.3 Image Analysis

The first step of the image analysis is focused on identifying the full 3-D coordinates of the traces which we image in the x-y-z scans. To this end, the microscope images are initially analyzed with IMARIS 5.5 (Bitplane AG). The program is specialized in the data processing method of three-dimensional and four-dimensional microscope images. Its algorithm is based on the local intensity contrast to the objects of interest. A median filter is usually applied prior to the analysis. Under the surpass view of IMARIS, the objects are processed as point-like structures. Automatic calculations of the depth of the individual points in the plane of the screen are done by the software, when we manually indicate the points at a trace on the

screen. The chain of points that is thus generated is used as an input for the final fit of the trace, where an automatic centering is performed. In Fig.5.3, we present the fitted trace with the background of raw data. In this way, the positional information of the point-like structures in the Cartesian coordinate system is obtained.

In the post-processing of the traces, the positional information of the traces is further transformed and analyzed in order to obtain the spatial resolved orientational information throughout the full droplet. For each coordinate of the trace we determine the tangent and then calculate the polar angle θ and azimuth angle ϕ of that tangent, according to Fig.5.1b. This post-processing is performed numerically by home-written Matlab software, see section 5.3.3.

5.3 Results and Discussions

5.3.1 Polarization Microscopy

Typical birefringent droplets with cholesteric *fd* dispersion are shown in Fig.5.4a-d, taken over a period of 3 days after preparation. The concentration of the *fd* virus dispersion was 23μg/ml. The polarization microscope images clearly indicates the smooth spherical shape of the droplets with a birefringent structure which settles after about one day. The evolution of the droplets was recorded 5 minutes (a), 1 hour (b), 23 hours (c) and 3 days (d) after the droplets were prepared. The droplet on the left part of the images kept similar polarization pattern as the beginning, with subtle rearrangement. On the lower part of the image, the pattern of the droplet dramatically differ between 1 hour and 24 hours after preparation, Fig.5.4a-c. The settling of the polarization patterns seems to be related to the concentration of the *fd* virus within the droplets: the evolution of the droplets with *fd* concentration above 60 μg/ml takes approximately only about 2 hours.

The polarization pattern we observe after 24 hours in Fig.5.4 can be characterized by a ring structure superimposed on a baseball-shape at the top left and a cross-shape structure at the bottom right. We further investigate these patterns by imaging the droplets during a 90° rotation of the microscope sample stage with fixed orientations of the polarizer and analyser. One type polarization pattern changes during the rotation accordingly, from cross-shape, baseball-shape, back to cross-shape again. This is shown subsequently in Fig.5.5a-e. A core region with ellipsoidal shape can be seen and bears a slight weakened birefringence. This pattern type will be referred to as 'baseball+++' hereafter, where the number of '+' indicates

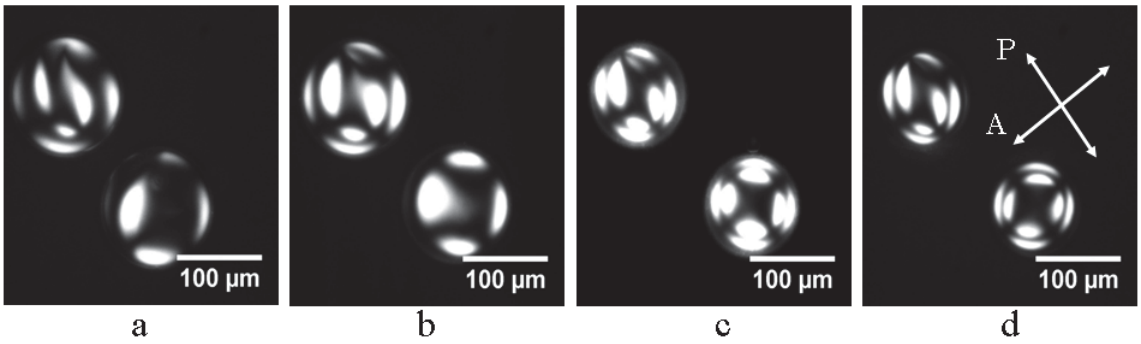

Figure 5.4: *The kinetics of droplets with a dispersion of fd virus at a concentration of 23µg/ml as imaged by polarization microscopy. The images were taken 5 minutes (a), 1 hour (b), 23 hours(c) and 3 days (d) after the droplets were produced. The directions of the polarizer and analyser for all images are indicated in (d).*

the numbers of rings. In contrast, in the other example is presented in Fig.5.5f-j the patterns hardly change during the rotation, while the central part of the birefringence is always dark. The patterns have a clear and constant cross-shape, which will be referred as 'cross++' pattern type. Both of the polarization pattern types mentioned above are found to be the 'prototypes' among our experimentally observed polarization patterns, because other patterns are found to be strongly related to one of these types. It is speculated that both 'prototypes' are different representations of the same structure of the director-field, owning to the tilting of the droplets. The steady states of the polarization patterns are presented in Tab.5.1.

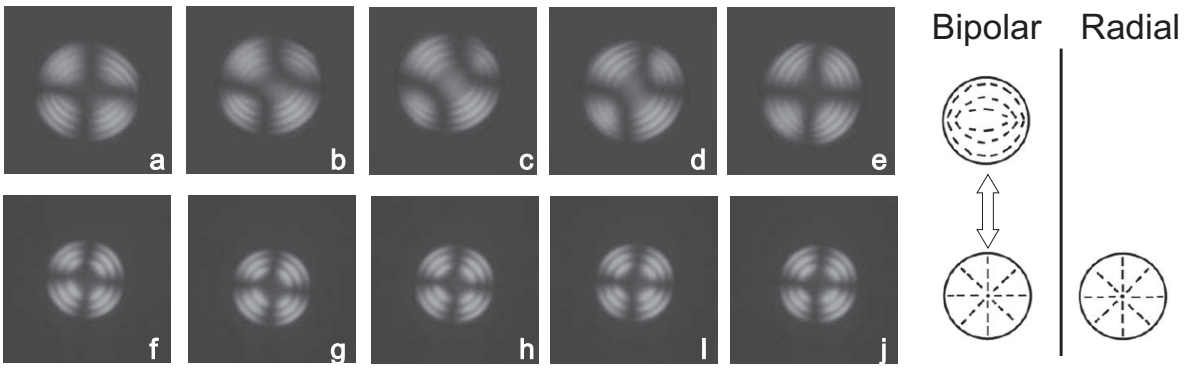

Figure 5.5: *Polarization pattern variations of droplets due to the rotation of the microscope sample stage. The pattern type of 'baseball' is shown in (a)-(e), and 'cross' in (f)-(j).*

The number of rings we observe, irrespective of the underlying pattern, depends on the size of droplet and the concentration of the *fd* virus. In Fig.5.6 we plot the combination of concentration and droplet size where a single ring is first observed (blue symbols), while the

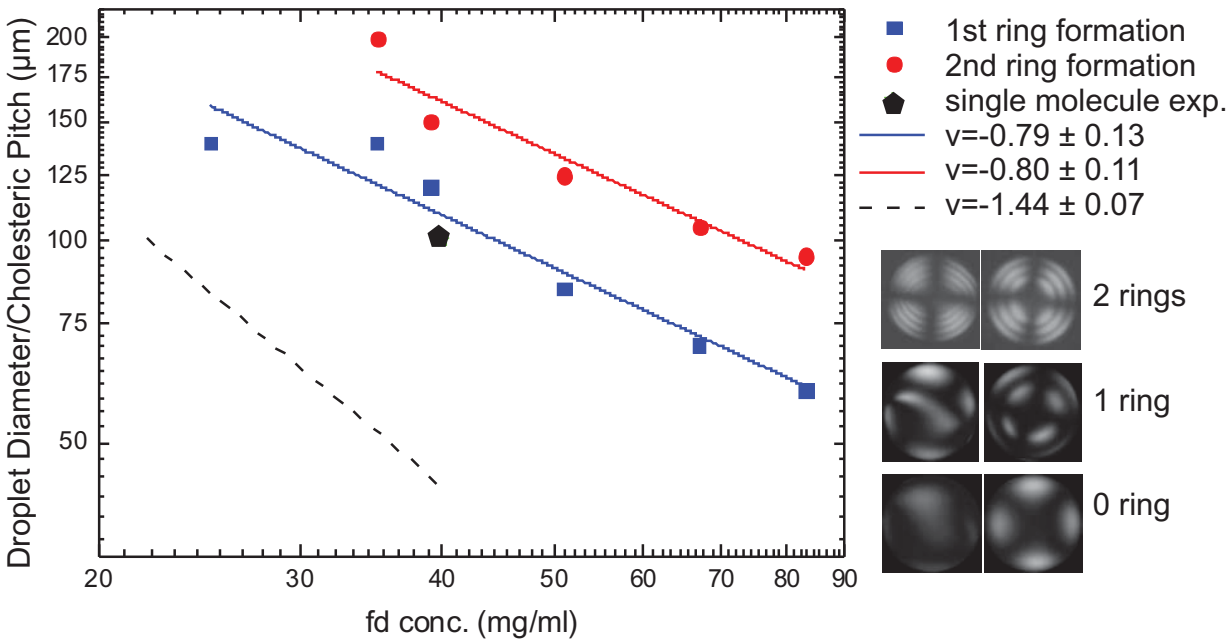

Figure 5.6: *The diagram of states of the polarization patterns formed by chiral nematic fd virus within droplets. The blue squares are experimentally determined transition line that separates polarization patterns with(on the right) and without (on the left) a single ring. The red dots set the crossing over from a single ring to two rings, from left to right. The linear fits v of these two can be compared to the cholesteric pitch size in the bulk phase, which is indicated by the black dashed line. The black polygon indicates the position of the later performed single particle experiment. The states of the mentioned classes are shown on the right.*

Abbreviation	Example	Description
Cross		cross- shape.
Baseball		baseball- shape.
Cross+		cross- shape with a ring.
Baseball+		baseball- shape with a ring.

‡ Notes: "+" here indicates number of discrete birefringent rings within the polarization patterns of the droplets.

Table 5.1: *Experimentally observed droplet birefringent patterns.*

red symbols indicate the boundary after which two rings are observe. The lines indicate a linear fit with a slope of $0.80\frac{\mu m}{mg/ml}$. Thus, all the droplets below the blue lines have simple structures, either cross-shaped or baseball-shaped, while droplet with one-ring are observed between the blue and red line, the so-called 'Cross+' and 'Baseball+'. We have to mention here that we also used higher concentrations of *fd* virus, where in bulk the formation of the smectic phases is expected. The ring formation for these droplets appeared at smaller size.

The relation between the concentration and the size of the droplet where the transitions are observed suggest that the ring formation is due to the cholesteric twist which is known to be present in the bulk phase of *fd*. In order to compare to the twist that is observed in bulk, we plot in Fig.5.6 also the relation between the cholesteric pitch of *fd* at a comparable ionic strength. Clearly, the twist is much stronger in bulk, which suggest that the twist is suppressed by the confinement in the droplet.

To summarize, the droplet size-related formation of the extra rings in the polarization patterns seems to suggest the twisting of the chiral nematic phase within the droplets. Moreover, we categorized the director-field configurations into two classes, but we assume that this is only due to the fact that we cannot control the orientation of the droplets and therefore we just view different projections of the droplet.

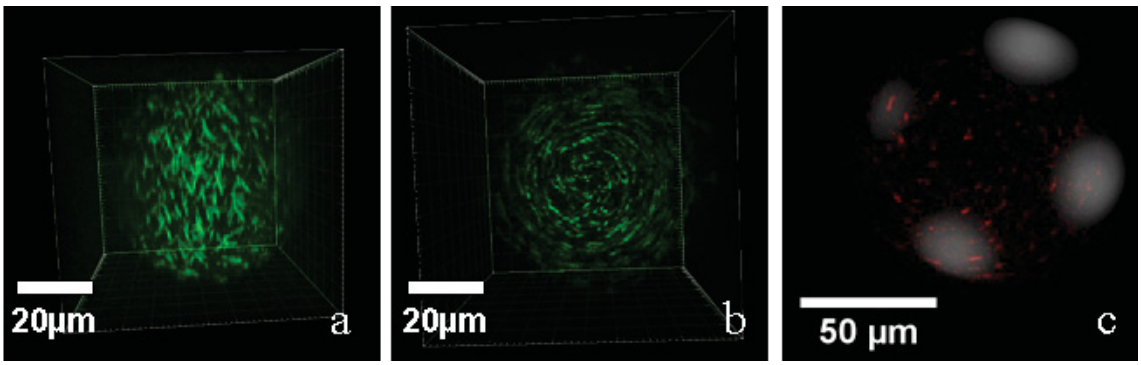

Figure 5.7: *The examples of three-dimensional view of fluorescence confocal microscope data of fd virus in a droplet:* ***a*** *and* ***b*** *from x-z and x-y planes perspectives respectively. The overlaid image of the polarization pattern and the confocal scan of a droplet at the equator* ***c****.*

5.3.2 Confocal Microscope Observations

A 3-D reconstruction of the traces of single labeled *fd* particles as obtained by confocal microscopy is presented in Fig.5.7a and b. In this example, the droplet is shown both from x-z and x-y perspectives. The overall shape of the trace-assembly is spherical from different perspectives, while there is an apparent ordering of the traces.

Clearly the director-field is not point symmetric, but has a symmetry axis which is found to point up in Fig.5.7a and to come out of the plane in Fig.5.7b. From this perspective, the traces form part of a circle around the middle of the axis. In this projection, traces in the middle of the droplet showed up as point-like objects, because one can only see the projection of the traces on the x-y plane. For the traces further away from the middle axis, their projections on the x-y plane are longer. This seems to be a common features of all droplets. From the other x-z perspective, Fig.5.7a, it is not easy to resolve the symmetry of the structures due to the overlaid information in the droplet. Fig.5.7c displays an overlay of a polarization pattern and fluorescent traces taken at the equator of the droplet. The fluorescent traces suggest a somewhat tilted symmetry axis that comes out of the plane. This is also what is expected for a cross-shape polarization pattern, as was suggested in section 5.3.1. We will further elaborate on this when we analyse the full 3-D structure of the director-field on the basis of the 3-D traces.

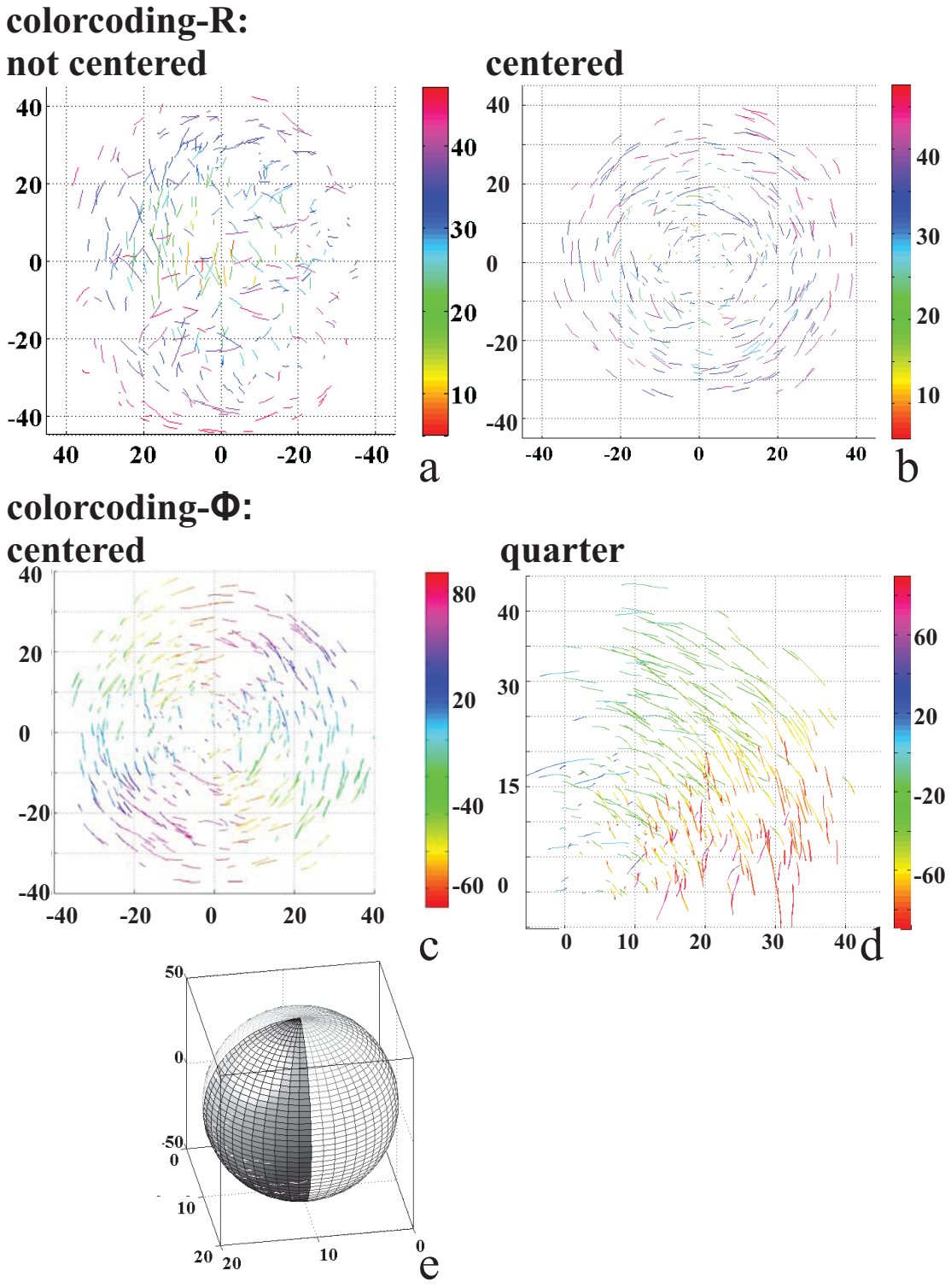

Figure 5.8: *Determination of the symmetry axis using projections of the traces of fd virus in the droplet. (a)-(d) and in a quarter-sphere (e) done by 3-d post-processing. The projection of the traces is done as sketched in (f). The traces are color coded by their azimuth angle ϕ in (d) and (e), r in (a) and (b), and θ in (c).*

5.3.3 Defining the Coordinate System

In order to perform a full 3-D analysis of the data, first the symmetry axis needs to be identified and the droplet needs to be reoriented such that this symmetry axis points up in the direction that we will then define as the z-direction. In order to do so, we placed the droplets at the origin of the spherical coordinate system and then performed different rotations until a rotation around the new z-axis does not give any distinguishable difference between the projections of the set of parameters that characterize the traces, as shown in Fig.5.8. The traces in this figure are visualized using a statistical color-coding according to the different parameters with the indicated colormaps.

Projections of the trajectories are displayed in Fig.5.8a and b, using a color-coding that reflects the r, which is defined as the distance to the origin of the droplet, see Fig.5.1. The director-field configuration can still not be identified for Fig.5.8a. The traces are found to have rotational symmetry around the z-axis, as shown in Fig.5.8b-c. The rotated coordinates of the traces result in a point symmetric distribution of the traces with a color that gradually changes from the inside to the outside, see Fig.5.8b. Clearly the symmetry axis is now pointing out of the plane. In Fig.5.8c traces are color-coded with their azimuth angle ϕ. The colors of the traces continuously change around the z-axis. To probe the axial symmetry of the director-field configuration, all the traces are superimposed to one quarter-sphere, as indicated in Fig.5.8. It is realized by rotation of the traces located within the other quarter-spheres by 90°, 180° and 270° around the z-axis, respectively. Judging from the homogeneous color distribution, which displays the gradient as expected for the azimuthal angle, the axis of symmetry was chosen correctly.

The symmetry axis was also confirmed by slicing the droplet into 10 slabs of about 8 μm along the z-axis and comparing the traces at equal distance from the equator. As an example, x-y projections of 6 slabs are shown in Fig.5.9 with traces that are color-coded by their polar angle θ. Indeed, the distribution and orientation of the traces are rotation symmetric around the origin within the slabs and are comparable to the slabs that have the same vertical distance away from the equator are comparable, e.g. (a)-(b),(c)-(d) and (e)-(f). With this information, the axis of symmetry of the director-field configuration around z-axis has been identified. In the analysis of the director-field we will use therefore the rotated coordinates and angles of the tangents of the traces.

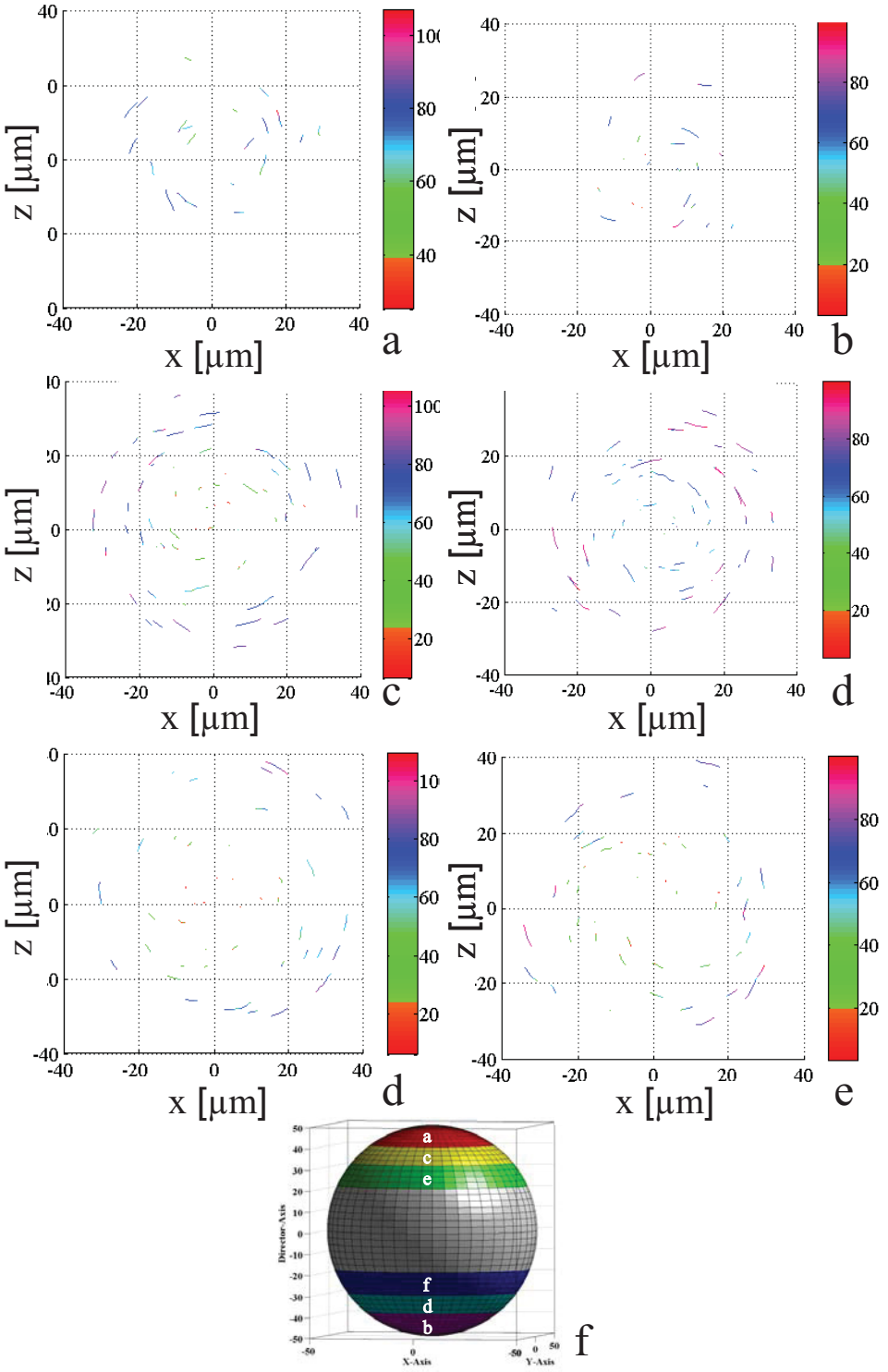

Figure 5.9: *Projections of traces of fd virus in slabs (thickness of 8 µm) taken at different heights as indicated in the cartoon on the left. The color code is given by θ.*

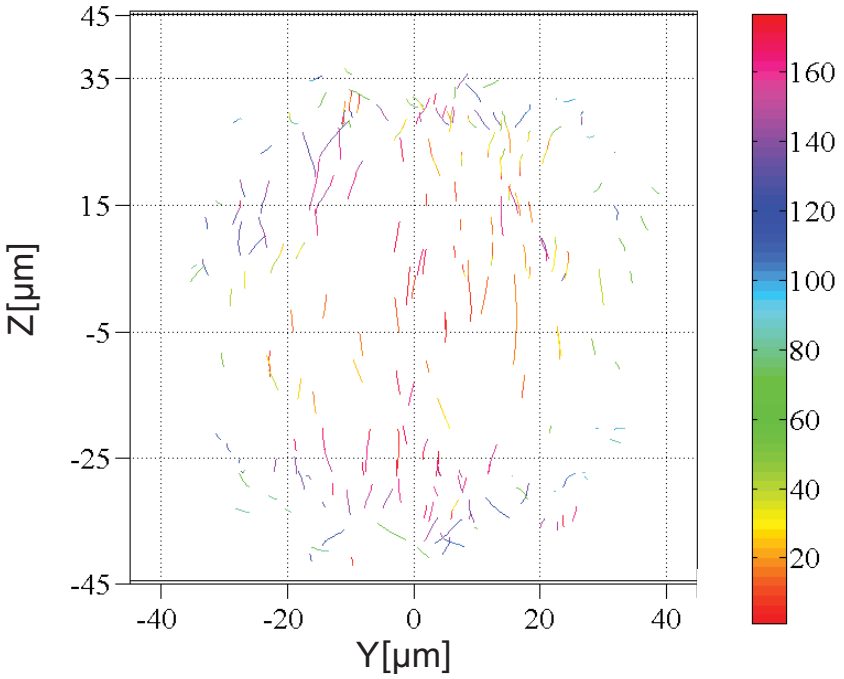

Figure 5.10: *Cross section of the droplet in the y-z plane. The traces are in the middle slab of the droplet, with a total number of 3 vertical slabs. The traces are color-coded by the polar angle θ, indicating the bipolar structure.*

5.3.4 The Director-field of a Confined *fd* Dispersion

The color-coding of the traces in the slabs depicted in Figs. 5.8, 5.9 and Fig.5.10 supplies valuable information on the structure of the director-field. First, the ϕ color-coding and the lines of the trajectories in Figs.5.8c and d show that the rods always align with the surface of the droplet as they follow the component $\hat{e}_\phi$, as defined in Fig.5.1. Thus, $f_3 = 0$, see Eq. 5.1. Second, Fig.5.10 clearly shows that the director field is bipolar, with two dislocations at the top and the bottom. Third, the colors of the traces change from the origin to the boundary in the according order. This color change reflects the change of the θ from 0° to values close to 90° for the slabs close to the equator, which is similar to a twist in the director-field in the bulk phase. The lengths of projected traces also shortens close to the origin, which is directly related to their polar angles θ which approaches 0 at the symmetry axis. With these observations we can qualify the structure of the director field as being a (twisted) bipolar (Fig. 5.1c) according to the definition of the group of Zůmer [21, 23, 97].

To quantify the latter observations, the polar angle θ is plotted as a function of the distance to the symmetry axis $r\sin\Theta$ for different slabs, see Fig.5.11. Here we use a binning of 4 μm along the radial direction and averaged over Φ. Graphs of slabs sharing the same vertical

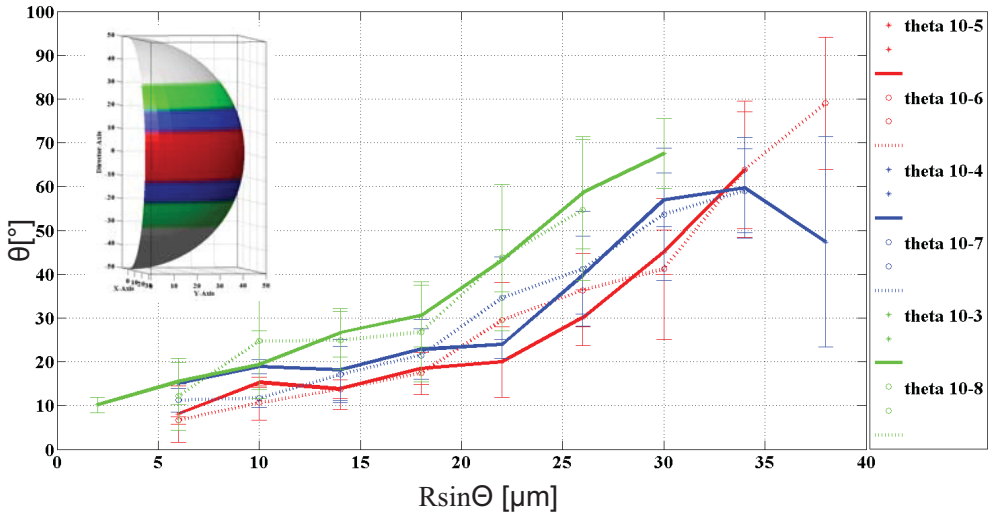

Figure 5.11: *The polar angle θ of the traces in the slab-views of the droplet with 10 slabs. The positions of the slabs in the droplet correspond to the line colors of the plots.*

distances away from the equator are labeled with the same color, where data from the upper part of the sphere is shown as dashed lines, and the lower part is shown as solid lines. The lines at equal distance to the equator overlap and therefore the θ values of the traces in the mirroring positions with respect to the equator can be summed up. It is important in order to improve the statistics.

The averaged graphs of θ of the traces vs $r\sin\Theta$ from the upper and lower parts of the droplet are depicted in Fig.5.12. Here, the droplet is sliced into 14 slabs of 3μm along the z-axis in order to obtain more details. The maximum value of $r\sin\Theta$ of the traces within slabs corresponds with the positions of the slabs. The colors of the graphs again correspond to the color of the slabs taken at the different positions of the droplet as indicated in the sphere sketch. The effect of the z-position is most obvious for the offset in the curves far away from the equator. This can be interpreted as a signature for a splay at the top of the droplet.

The increase of θ from the origin to the lateral boundary is observed for all slabs, as expected for a cholesteric pitch. There are, however, two important features that do not comply with a twist of the director driven by a intrinsic chiral twist of the dispersion. First, there is no constant slope, especially around the equator. This means that a constant rotation as it is assumed in the main theoretical approach, see Refs. [21, 23, 97], is not applicable. Second, the slope is much smaller than expected from the cholesteric pitch in bulk, as indicated by the black dashed lines in Fig. 5.12. Thus, confinement strongly suppresses the twist of the director, in stead of enhancing a twist, confirming the observation we already made for the

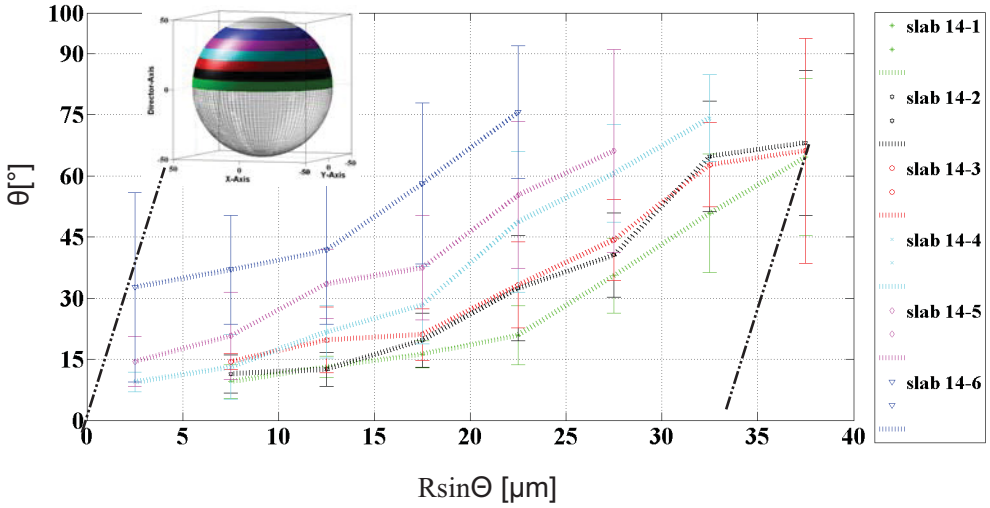

Figure 5.12: *The overall polar angle θ of the slabs with in a droplet. Total number of 14 slabs and the positions of the slabs are indicated in the 3d spherical image of the droplet. The colors of the line plot correspond to the positions of the slabs in the droplet.*

polarization images in Fig.5.6. Interestingly, it has been observed for achiral systems that confinement can induce a twist in the director field [25]. We speculate that the wall anchoring dominates the response of the director-field. The assumption that the oil-water interface can act as a hard wall can be inferred from the fact that the interfacial tension between the oil and water phase is so high that we did not observe any deviation from a spherical shape even for high concentrations and small droplets. Clearly the chiral twist strength is insufficient to counterbalance the confinement induced structure. This can also be concluded from the fact that for lower concentrations, which have a significantly lower twist constant [82], the slope in θ is even smaller, see Fig.5.13.

5.4 Conclusion

We characterized the director-field of a cholesteric *fd* dispersion in droplets surrounded by the oil phase, which were produced using a microfluidic device. Polarization images already suggested that the cholesteric twist in the director-field is suppressed by the confinement. Single-particle experiments, using confocal microscopy, show unambiguously and independent of the orientation of the droplet that a twisted bipolar structures is formed. More importantly, with this approach important details on the structure are obtained. The fact that the twist is non-monotonous and indeed much suppressed by the confinement hints to adjustments that

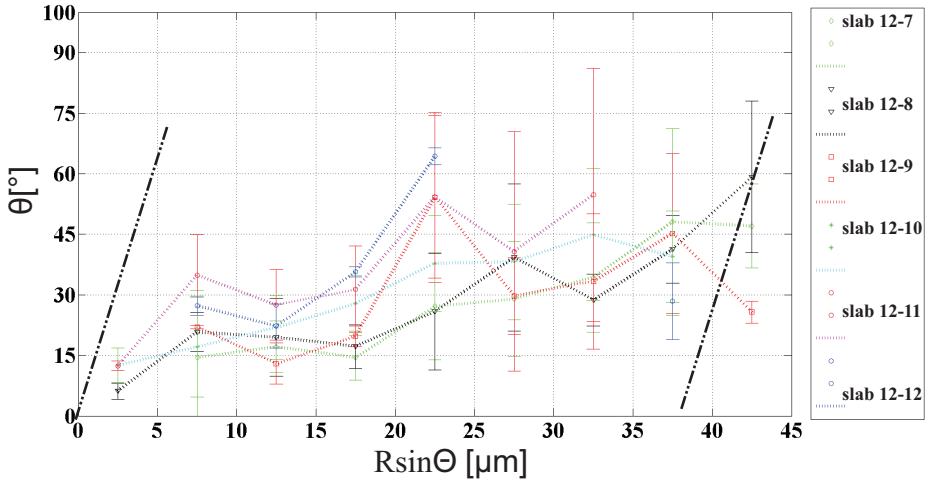

Figure 5.13: *The overall polar angle θ of the slabs, total number of 12 slabs within a droplet. The colors of the line plot correspond to the positions of the slabs in the droplet. The lines present the θ of the traces in the six slabs of the lower hemisphere. The thickness of the slabs is 8μm.*

will need to be made in the theory. In addition, a 3-D fitting routine of the Franck free energy needs to be developed to fit the fractions of the 3-D director field that we presented here.

6 Manipulating Nematic Droplets

In this exploratory chapter, we present the potential applications of the experimental model, the mesoscopic *fd* droplets in chapter 4. We observe the reversible response of the director-field to the magnetic field and the deform of the droplets via polarization microscope. We also observe that shrinkage of nematic droplets due the mass transfer as discussed in chapter 2, results in a phase transition and droplet deformation.

6.1 Introduction

The initial goal of this thesis was to study the competition between the elastic deformation of the nematic director-field and the interfacial tension of water-in-oil mesoscopic droplets and to study the effect of external fields on the behavior of nematic droplets. In chapter 5 we saw that the elastic stress was not sufficient to deform the droplet. Here we used, however, the commercial available surfactant Pico-surf with the FC-40 as the carrier oil which guaranteed no shrinking nor coalescence of the droplets. In this chapter we explore what happens with the nematic droplets when we use combinations of oil and surfactant which are non-ideal such that both phenomena can take place. We expect that two nematic droplets which coalesce will form structures according to the diagram of states given in chapter 5. The question is if the coalescence is so smooth that indeed the expected structures are formed. The mass transfer, where water is removed from the droplet would be of potential interest if it only involves water and not the mesogens that are incorporated in the water droplet. This would lead to a shrinkage of the droplet and potentially a phase transition due to the increase in the particle density.

Another interesting question is how the nematic droplets are affected by external fields. The study of the dependence of the director-field in confinement on external electric or magnetic field is studied by several groups [10,23,28,40,100]. One feature of the *fd* droplets that could be directly affected by an external field is the twist in the director-field. The unwinding of the cholesteric pitch by a magnetic field in bulk phase was demonstrated by [82]. Therefore it is to be expected that similar transitions are also observed in confinement. We aim to probe the states of the director-field in spherical confinements after imposing strong external field. Indeed, the transition of director fields from the 'twisted bipolar' state to the planner bipolar state in response to the field was reported by Bajc *et al*, for chiral nematic droplets with tangential anchoring conditions [23].

This chapter is organized as follows: we first discuss director structure within the *fd* droplets after forced coalescence, followed by the effect of shrinkage on the shape and internal structure. We end with the effect of the magnetic field in the structure of the droplets. All the materials and experimental details were discussed in chapter 2 and 5.

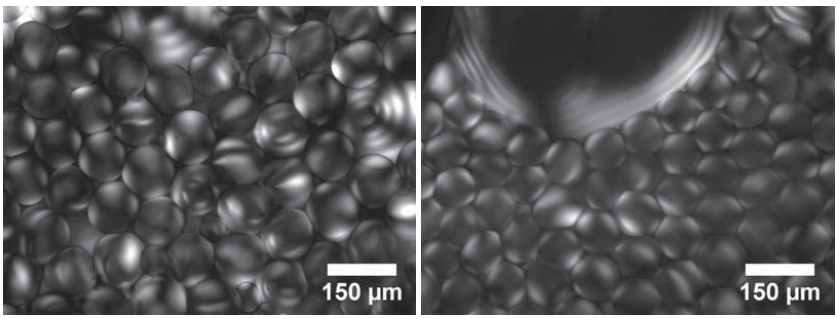

Figure 6.1: *Droplets are compressed horizontally. The deformation happened to certain degree before the eventual rupture of droplets .*

6.2 Deformation and Coalescence of the *fd* droplets

In Fig.6.1 we display an example of droplets under some mechanical compression. The original diameter of droplets was about 100 μm and the thickness of the capillary was about 300 μm. The droplets gathered on the upper layer of the capillary, owning to the density difference between the aqueous droplets and the carrier oil phase, see section 2.2.1. The mechanical compression of the droplets was introduced by evaporation of the carrier oil phase from two lateral directions, when the capillary was not properly sealed. It is well known that the maximum packing density of 74% is considered to be appropriate for a stable microemulsion system.

Here, the packing density was approaching the limit. The deformation of the droplets was observed, but the droplets still retained their volumes and internal structures, as can be inferred from the similarity of the polarization patterns. A huge disk-like droplet was also observed in the upper part of Fig.6.1b, due to the merging of many droplets.

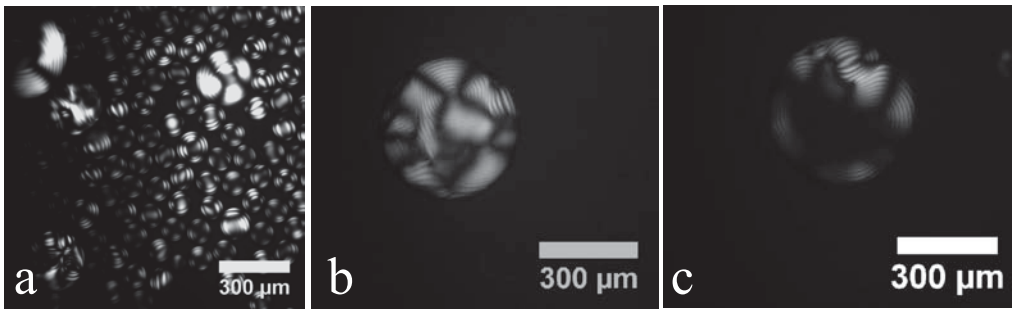

Figure 6.2: *Droplets as produced by microfluidics (a) merged into bigger droplets with spherical shape (b and c).*

We also observed the merging of droplets droplets, as shown in Fig.6.2. The resulting droplets either possess the common polarization patterns or display the mosaic of each compositional droplet patterns. In this example, the major population of droplets produced at the microfluidic chip junction have a diameter of 120 μm, see in Fig.6.2.(a). The bigger droplets at the upper left and right corners of this image show, however, the common polarization patterns, which suggest the 'fusion' of the internal director-field. Another type of merged droplets is shown in Fig.6.2 (b) and (c). Both droplets result from the coalescence of a few small droplets based on their polarization patterns. The boundaries of each constitute(droplet) are well preserved, but the internal structure is complex and suggests that the original director fields of the merged droplets survived the coalescence. Presumably, the arrangement of the *fd* viruses at the contact regions are vital during the droplet merging process. The director-fields of the separate droplets might melt into one director-field, if the *fd* viruses at the interface happen to have the same orientation or when in both droplets it was not yet unsettled (Fig.6.2a). This behavior might be linked to the merging of the nematic tactoids during I-N phase separation.

6.3 Shrinking of the *fd* droplets

We applied the mass transfer effect which we described in chapter 2, to the *fd* droplets, starting at a concentration of fd virus of 78 mg/ml using parafin oil as the continuous phase and a surfactant concentration of $2\%wt$. The initial droplet size is at the lower limit of the droplets

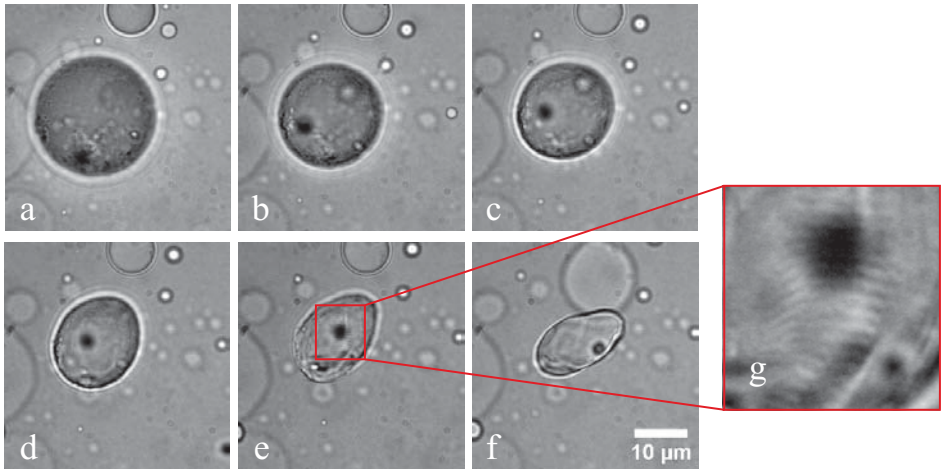

Figure 6.3: *Shrinking process due to the mass transfer of fd droplets with a starting concentration of 78 mg/ml in (a) and a final concentration where the dispersion is probably in a highly ordered state. The local zoom-in of the central part of the droplet is displayed in (g), in which smectic layering can be observed.*

that we studied in chapter 5, see also the diagram of states in Fig. 5.6. We observed a clear shrinking of the nematic droplet from an initial spherical shape to a 'potato' shape, from Fig.6.3a to f. Already after slight shrinkage we saw a deformation to an ellipsoidal shape, see Fig.6.3b, see Supplementary info. In Fig.6.3d, when the shape is already quite irregular, we observe the formation of a regular layering of approximately the length of the rod in the central part of the droplet. This strongly suggests the formation of the smectic phase. At this point in the shrinkage the droplet is still relatively smooth. In the later stage the structure becomes more irregular, see Fig.6.3g. Note that this shrinking process is very non-linear. It takes a long time ($\approx 10h$) to see the first deformation, but ones the deformation sets in, the final potato shaped structure is quickly obtained. This final structure is however stable, suggesting a highly dense packing of colloidal rods.

This sequence of images has two important implications. First, it suggests that the mass transfer can be used to concentrate colloidal dispersions in the droplets. This is a nice way to continuously scan through the phase diagram of colloids. Second, it shows that indeed water droplets can be deformed by the presence of a liquid crystalline dispersion and thus that Frank elasticity can be stronger than the interfacial tension. The reason that we did not observe it in chapter 5 is just due to the fact that very small droplets, with a diameter of the order of 20 rods or less, and an extremely high volume fraction are needed. We speculate that deformation will set in earlier with really much stiffer viruses, which in principle are recently available.

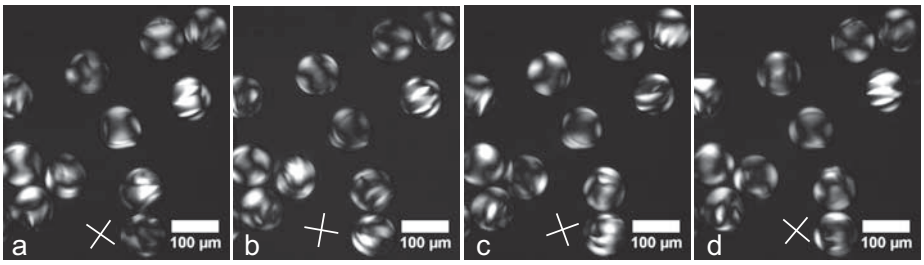

Figure 6.4: *Nematic droplets in an external magnetic field. The images (a)-(d) were taken during rotation of the polarizer and analyzer of $\pi/2$ gradually. The orientations of the polarizer and analyzer are marked at the lower part of these figures. These are monodisperse droplets with a diameter of 100μm.*

6.4 *fd* Droplet under Magnetic Field

In our experiment, we observe the influence of magnetic field (2T) on the alignment of *fd* virus confined in spherical droplets. The settled director-field displays clearly distinct features of the polarization pattern. The gradual variations of the patterns during the rotation of the polarizer and analyzer over $\pi/2$ are shown in Fig.6.4, from (a) to (d). Most droplets have no 'rings' in their polarization patterns, although they should have one 'ring' formed according to the experimental conditions, see Fig.5.6. This could be due to the orientation of the droplet: the unwinding of the twisted director-field could depend on the orientation of the symmetry axis with respect to the magnetic field. The response of the director-field to the magnetic field is found to be reversible: the rings will return after a couple of hours when the field is removed. Otherwise the orientation of the droplets does not seem to be affected by the field while the droplets retain their spherical shape.

6.5 Conclusions and outlook

We showed here with three examples that mesoscopic droplets of *fd* virus dispersions in the oil phase form a model system to study various aspects of liquid crystals and in soft matter in general. The *fd* droplets can be stable under certain mechanical compression and sustain some degree of deformation. The elasticity of these droplets will depend on the way the droplet is deformed due to the anisotropy of the internal structure which would be a model for e.g. cells. Merging of droplets occurs with and without the melting of director-field of the separate droplets into a single director field. It shows that structures can survive when brought in contact even if they have exactly the same phase.

The shrinking of the droplets due to the budding effect resulted in a deformation as well as a phase transition from nematic to smectic. This observation has many implications. It means that water can be extracted from the droplet while the colloids sty in the droplet. It is of course not known how big the colloids need to be in order to remain in the droplet, but in principle it supplies a nice to manipulate and study phase transitions. Moreover, it showed that Frank elasticity can indeed overcome the water-oil interfacial tension.

All process described above can in principle be manipulated by using a magnetic field, as we showed that a reversible rearrangement of the internal ordering within the droplets could be achieved. Thus, we now have an extended toolbox to manipulate and shape complex mesoscale droplets.

Acknowledgment

First of all, I would like to express my gratitude to Prof.Dr.Pavlik Lettinga, who has spent lots of efforts in introducing me to the interesting project in the field of soft matter. He found time to help me with my experimental work and spent hours on the in-depth discussions. For all the guidance and the cheerful attitude, I will keep Pavlik in mind, as an excellent supervisor and a brilliant artist. I am very grateful and appreciative of Dr. Manolis Stiakakis, for his countless help during the last years and the enjoyable moments in our office. I also want to thank Manolis for being considerate of feelings and for his help of speeding up my work. I am very appreciative of Prof.Dr.Jan Dhont for the opportunity to work in his group, and for his kind suggestions when I encountered problems. I will also remember the excellent lectures he gave in Biosoft. I thank Prof.Dr.Stefan Egelhaaf for taking over the co-supervision of my thesis.

I appreciate the grateful working atmosphere in ICS-3 and thank people who supported me during my work in Jülich. I would like to thank Marie, who saved me many times from getting into troubles with paperwork. I thank Simone and Hartmut for their warm words and help. I thank Peter for the questions I got from my seminar talk and the helpful discussions about the FBMA particles. I am grateful to Jonas for translating the abstract of my dissertation into German language, to Karin and Sylvia for their help in the laboratory, to Christoph, Bastian, Marco, Jing, Donald, Simon and Hu for the discussions and the help. I thank Zilin, Wei, Silvia, Yi and Olivera for their accompany, and thank Rafaelfor their sense of humor at the later stage.

I thank Oliver Dammone (Uni. Oxford) and José Alvarado (FOM Institute AMOLF), and Dirk Aarts (Uni. Oxford) for the collaborating experimental work in chapter 4. I thank Prof.Dr.R. Merkel and Prof.Dr. D. Willbold for allowing me to conduct part of the confocal measurements and analyze the data by IMARIS software. I thank Dr.R.Springer for his help to start the analytical work based on Matlab. I am very grateful for the practical support from the colleagues and discussions with Dr. I.Kirchenbuchler, Dr. E.Jaschinski, and K. Wang. I am grateful to Y. Zhang for the collaboration in the experimental work of chapter 3.

Last but not least, I would like to thank my parents and Zhirong for their love and support.

Erklärung

Ich versichere, dass ich die von mir vorgelegte Dissertation selbständig angefertigt, die benutzten Quellen und Hilfsmittel vollständig angegeben und die Stellen der Arbeit - einschließlich Tabellen, Karten und Abbildungen -, die anderen Werken im Wortlaut oder dem Sinn nach entnommen sind, in jedem Einzelfall als Entlehnung kenntlich gemacht habe; dass diese Dissertation noch keiner anderen Fakultät oder Universität zur Prüfung vorgelegen hat; dass sie - abgesehen von angegebenen Teilpublikationen - noch nicht veröffentlicht worden ist sowie, dass ich eine solche Veröffentlichung vor Abschluß des Promotionsverfahrens nicht vornehmen werde. Die Bestimmungen dieser Promotionsordnung sind mir bekannt. Die von mir vorgelegte Dissertation ist von Prof. Dr. M.P.Lettinga betreut worden.

Ich versichere an Eides Statt, dass die Dissertation von mir selbständig und ohne unzulässige fremde Hilfe unter Beachtung der "Grundsätze zur Sicherung guter wissenschaftlicher Praxis an der Heinrich-Heine-Universität Düsseldorf" erstellt worden ist.

Yunfei Jia

List of Figures

List of Tables

Bibliography

[1] R.A.Kyle. Jean baptiste perrin. *JAMA*, 242(8):744–741, 1979.

[2] W.Van Megen P.N.Pusey. Phase behavior of concentrated suspensions of nearly hard colloidal spheres. *Nature*, 320:340–342, Mar 1986.

[3] J.Prost P.G.de Gennes. *The physics of liquid crystals*. ISBN: 9780198517856. Oxford University Press, Clarendon, Oxford, 1993.

[4] V.Tsvetkov. *Acta Physicochim*, (USSR)16:132, 1942.

[5] I-C.Khoo. *Liquid crystals*. John Wiley & Sons, Inc., 2nd edition, 2007.

[6] C.Imrie and M.Gagan. *The molecular world*, chapter Chirality and liquid crystals. Open University course, 2002.

[7] L.Onsager. The effects of shape on the interaction of colloidal particles. *Annals of the New York Academy of Sciences*, 51(4):627–659, 1949.

[8] J.D.Bernal I.Fankuchen F.C.Bawden, N.W.Pirie. Liquid crystalline substances from virus-infected plants. *Nature*, 138(1051-1052), 1936.

[9] H.Zocher. Über freiwillige structurbildung in solen. *Ztschr.anorg.Chem.*, 1925.

[10] S.A.Taraskin A.V.Kaznacheev, M.M.Bogdanov. The nature of prolate shape of tactoids in lyotropic inorganic liquid crystals. *J.Exp.Theor.Phys*, 95:57–63, 2002.

[11] J.X.Tang J.Viamontes, P.W.Oakes. Isotropic to nematic liquid crystalline phase transition of f-actin varies from continuous to first order. *Phys.Rev.Lett.*, 97:118103, 2006.

[12] J.X.Tang P.W.Oakes, J.Viamontes. Growth of tactoidal droplets during the first-order isotropic to nematic phase transition of f-actin. *Phys.Rev.E*, 75:061902, 2007.

[13] P.Poulin C.Blanc P.van der Schoot N.Puech, E.Grelet. Nematic droplets in aqueous dispersions of carbon nanotubes. *Phys.Rev.E*, 82:020702, 2010.

[14] J.X.Tang J.Viamontes. Continuous isotropic-nematic liquid crystalline transition of f-actin solutions. *Phys.Rev.E*, 67:040701, 2003.

[15] E.G.Virga. *Variational Theories for Liquid Crystals*. Chapman and Hall, 1994.

[16] J.P.F.Lagerwall. *Soft materials-generation, physical properties and fundamental applications*, chapter An introduction to the Physics of Liquid Crystals. John Wiley & Sons, 2013.

[17] P.van der Schoot P.Prinsen. Shape and director-field transformation of tactoids. *Phys.Rev.E*, 68:021701, 2003.

[18] P.van der Schoot P.Prinsen. Continuous director-field transformation of nematic tactoids. *Eur.Phys.J.E*, 13:35–41, 2004.

[19] *The static and dynamic continuum theory of liquid crystals-A mathematical introduction*. Taylor&Francis, 2004.

[20] *Physical properties of liquid crystals*. Wiley-VCH, 1999.

[21] M.Ravnik S.Zŭmer D.Sec, T.Porenta. Geometrical frustration of chiral ordering in cholesteric droplets. *Soft Matter*, 8:11982–11988, 2012.

[22] P.J.Collings T.C. Lubensky A.G.Yodh J.Jeong, Z.S.Davidson. Chiral symmetry breaking and surface faceting in chromonic liquid crystal droplets with giant elastic anisotropy. *PNAS*, 111(5):1742–1747, 2013.

[23] J.Bajc and S.Zŭmer. Structural transition in chiral nematic liquid crystal droplets in an electric field. *Phys.Rev.E*, 55:2925–2937, 1997.

[24] J.W.Doane J.H.Erdmann, S.Zŭmer. Configuration transition in a nematic liquid crystal confined to a small spherical cavity. *Phys.Rev.Lett.*, 64:1907–1910, 1990.

[25] O.D.Lavrentovich L.Tortora. Chiral symmetry breaking by spatial confinement in tactoidal droplets of lyotropic chromonic liquid crystals. *PNAS*, 108:5163–5168, 2011.

[26] J.Z.Y.Chen W.Zhang, Y.Jiang. Onsager model for the structure of rigid rods confined on a spherical surface. *Phys.Rev.Lett.*, 108:057801, 2012.

[27] M.W.Kim J.Jeong. Confinement-induced transition of topological defects in smectic liquid crystals: From a point to a line and pearls. *Phys.Rev.Lett*, 108:207802, 2012.

[28] F.Debeauvails S.Candau, P.le Roy. Magnetic field effects in nematic and cholesteric droplets suspended in an isotropic liquid. *Molecular Crystals and Liquid Crystals*, 23:283–297, 1973.

[29] D.Levy E.Castellón, M.Zayat. Molecular configuration transitions of a nematic liquid crystal encapsulated in organically modified silicas. *Phys.Chem.Chem.Phys.*, 11:6234–6241, 2009.

[30] P.S.Drzaic. *Liquid Crystal Dispersions*. World Scientific, 1995.

[31] S.Fraden Z.Dogic. Smectic phase in a colloidal suspension of semiflexible virus particles. *PRL*, 78(12):2417–2420, 1997.

[32] E.Grelet M.Aadams S.Fraden Z.Dogic, K.R.Purdy. Isotropic-nematic phase transition in suspensions of filamentous virus and the neutral polymer dextran. *PRE*, 69:051702, 2004.

[33] E.Grelet. Hexagonal order in crystalline and columnar phases of hard rods. *PRL*, 100:168301, 2008.

[34] A.Imhof D.Derks J.K.G.Dhont M.P.Lettinga, K.Kang. Kinetic pathways of the nematic-isotropic phase transition as studied by confocal microscopy on rod-like viruses. *J.Phys.:Condens.Matter*, 17:S3609–3618, 2005.

[35] P.Holmqvist A.Imhof D.Derks J.K.G.Dhont M.P.Lettinga, K.Kang. Nematic-isotropic spinodal decomposition kinetics of rodlike viruses. *PRE*, 73:011412, 2006.

[36] S.Fraden E.Grelet. What is the origin of chirality in the cholesteric phase of virus suspensions? *Phys.Rev.E*, 2003.

[37] S.Fraden Z.Dogic. Ordered phases of filamentous viruses. *Current opinion in colloidal and interface science*, 2006.

[38] K.R.Purdy. *Liquid Crystal Phase Transitions of Monodisperse and Bidisperse Suspensions of Rodlike Colloidal Virus*. PhD thesis, Department of Physics, Brandeis University, 2004.

[39] S.Fraden A.Rühm L.Lurio S.G.J.Mochrie K.R.Purdy, Z.Dogic. Measuring the nematic order of colloidal fd virus by x-ray diffraction. *PRE*, 2003.

[40] P.van der Schoot H.N.W.Lekkerkerker A.A.Verhoeff, R.H.J.Otten. Magnetic field effects on tactoids of plate-like colloids. *The Journal of Chemical Physics*, 13:044904, 2011.

[41] J.Bibette F.Leal-Calderon, V.Schmitt. *Emulsion Science, Basic Principles*. Springer, 2007.

[42] G.M.Whitesides. The origins and the future of microfluidics. *Nature Protocols*, 442:368, 2006.

[43] J.R.Anderson D.T.Chiu H.Wu O.J.Schueller G.M.Whitesides J.C.McDonald, D.C.Duffy. Fabrication of microfluidic systems in poly(dimethylsiloxane). *Electrophoresis*, 21:27–40, 2000.

[44] S.R.Quake T.M.Squires. Microfluidics: Fluid physics at the nanoliter scale. *Rev.Mod.Phys.*, 77:977–1026, 2005.

[45] A.R.Abate and D.A.Weitz. Faster multiple emulsification with drop splitting. *Lab Chip*, 11:1911–1915, 2011.

[46] N.Berton L.Prat G.Hadziioannou M.Bouquey, C.Serra. Microfluidic synthesis and assembly of reactive polymer biads to form new structured polymer materials. *Chemical Engineering Journey*, 135(1):S93–98, 2008.

[47] D.A.Weitz S.Seiffert. Controlled fabrication of polymer microgels by polymer-analogous gelation in droplet microfluidics. *Soft Matter*, 6, 2010.

[48] J.Leng A.Merlin, J-B.Salmon. Microfluidic-assisted growth of colloidal crystlas. *Soft Matter*, 8:3526–3537, 2012.

[49] M.Jain M.Nilsson EA.Namsaraev GA.Karlin-Neumann H.Fakhrai-Red M.Ronaghi TD.Willis U.Landegren RW.Davis P.Hardenbol, J.Baner. Multiplexed genotyping with sequence-tagged molecular inversion probes. *Nat.Biotechnol.*, 21(6):673–678, 2003.

[50] J.Gobom L.Nyarsik H.Seitz H.Lehrach S.Sauer, B.M.H.Lange. Miniaturization in functional genomics and proteomics. *Nature Reviews Genetics*, 6:465–476, 2005.

[51] Q.Fu V.Tereshko D.L.Chen J.D.Tice-R.F.Ismagilov L.Li, D.Mustafi. Nanoliter microfluidic hybrid method for simultaneous screening and optimization validated with crystallization of membrane proteins. *PNAS*, 103(51):19243–19248, 2006.

[52] W.L.Ung D.A.Weitz A.D.Griffiths J.A.Heyman L.Mazutis, J.Gilbert. Single-cell analysis and sorting using droplet-based microfluidics. *Nature Protocols*, 8:870–891, 2013.

[53] D.S.Tawfik A.D.Griffiths. Miniaturising the laboratory in emulsion droplets. *TRENDS in Biotechnology*, 24:9, 2006.

[54] D.Bartolo and D.G.A.L.Aarts. Microfluidics and soft matter: small is useful. *Soft Matter*, 8:10530–10535, 2012.

[55] P.S.Doyle D.Dendukuri. The synthesis and assembly of polymeric microparticles using microfluidics. *Advanced Materials*, 21:4071–4086, 2009.

[56] L.-H.Hung A.P.Lee S.-Y.Teh, R.Lin. Droplet microfluidics. *Lab Chip*, 8:198–220, 2008.

[57] K.B.S.Devaiah-V.Vitelli A.Fernandez-Nieves T.Lopez-Leon, V.Koning. Frustrated nematic order in spherical geometries. *Nature Physics*, 7:391–394, 2011.

[58] P.Rudquist J.Lagerwall H-L Liang, R.Zentel. Towards tunable defect arrangements in smectic liquid crystla shells utilizing the nematic-smectic transition in hybrid-alighned geometries. *Soft Matter*, 2012.

[59] C.L.Ren T.Glawdel. Droplet formation in microfluidic t-junction generators operating in the transitional regime. iii. dynamic surfactant effects. *Phys.Rev.E*, 86:026308, 2012.

[60] Y.Zhang H.Liu. Droplet formation in a t-shaped microfluidic junction. *J.Appl.Phys.*, 106:034906, 2009.

[61] G.F.Christopher, N.N.Noharuddin, J.A.Taylor, and S.L.Anna. Experimental observations of the squeezing-to-dripping transition in t-shaped microfluidic junctions. *Phys.Rev.E*, 78:036317, 2008.

[62] Y.Zhang H.Liu. Droplet formation in microfluidic cross-junctions. *Phys.Fluids*, 23:082101, 2011.

[63] J.Bibette N.Bremond. Exploring emulsion science with microfluidics. *Soft Matter*, 8:10549–10559, 2012.

[64] S.L.Anna G.F.Christopher. Microfluidic methods for generating continuous droplet streams. *J.Phys.D:Appl.Phys.*, 40:R319.

[65] E.Windhab C.Cramer, P.Fisher. Drop formation in a co-flowing ambient fluid. *Chem.Eng.Sci.*, 2004.

[66] H.A.Stone D.F.Zhang. Drop formation in viscous flows at a vertical capillary tube. *Phys.Fluids*, 1997.

[67] A.S.Utada A.Ajdari P.Guillot, A.Colin. Stability of a jet in confined pressure-driven biphasic flows at low reynolds numbers. *Phys.Rev.Lett.*, 2007.

[68] R.Mathey A.Novelli-Rousseau V.Heran-S.Morales F.Rivera-P.L.Loly J-P.Moy F.Maallard P.R.Marcoux, M.Dupoy. Micro-confinement of bacteria into w/o emulsion droplets for rapid detection and enumeration. *Colloids and Surfaces A:Physicochem.Eng.Aspects*, 2011.

[69] J.Weers A.Kabalnov. Kinetic of mass tranfer in micellar systems:surfactant adsorption,solubilization kinetics,and ripening. *Langmuir*, 1996.

[70] P.D.I.Fletcher S.Rippon B.P.Binks, J.H.Clint. Kinetics of swelling of oil-in-water emulsions stabilized by different surfactants. *Langmuir*, 1999.

[71] D.T.Chiu M.He, C.Sun. Concentration solutes and nanoparticles within individual aqueous microdroplets. *Anal.Chem.*, 2004.

[72] P.T.Spicer A.Q.Schen, D.Wang. Kinetics of colloidal templating using emulsion drop consolidation. *Langmuir*, 2007.

[73] *Colloid and Interface Chemistry for Nanotechnology*, chapter Particle-surfactant interaction at liquid interfaces. CRC Press, 2013.

[74] S.U.Pickering. Emulsions. *J.Chem.Soc.*, 1907.

[75] B.P.Binks T.S.Horozov. Particle-stabilized emulsions:a bilayer or a bridging monolayer. *Angew.Chem.Int.Ed.*, 45:773–776, 2006.

[76] B.L.Holt P.Beaussoubre-K.Wong B.P.Binks, P.D.I.Fletcher. Phase inversion of particle-stabilised perfume oil-water emulsions:experiment and theory. *Phys.Chem.Chem.Phys.*, 2010.

[77] A.T.Tyowua B.P.Binks. Influence of the degree of fluorination on the behaviour of silica particles at air-oil surfaces. *Soft Matter*, 9:834, 2013.

[78] *Colloidal particles at liquid interface*, chapter Solid-stabilized emulsions:a review. Cambridge University Press, 2006.

[79] E.Vignati and R.Piazza. Pickering emulsions:€‰ interfacial tension, colloidal layer morphology, and trapped-particle motion. *Langmuir*, 19(17):6650–6656, 2003.

[80] B.P.Binks V.Schmitt-F.Leal-Calderon S.Arditty, C.P.Whitby. Some general features of limited coalescence in solid-stabilized emulsions. *Eur.Phys.J.E*, 11:273–281, 2003.

[81] C.Pathmamanoharan M.Rasa-A.P.Philipse G.H.Koenderink, S.Sacanna. Preparation and properties of optically tranparent aqueous dispersions of monodisper fluorinated colloids. *Langmuir*, 17:6086–6093, 2001.

[82] S.Fraden Z.Dogic. Cholesteric phase in virus suspensions. *Langmuir*, 16:7820–7824, 2000.

[83] D.A.Weitz P.Poulin. Inverted and multiple nematic emulsions. *Phys.Rev.E*, 57(1):626–636, Jan 1998.

[84] R.Evans M.Dijkstra, R.van Roij. Wetting and capillary nematization of a hard-rod fluids: a simulation study. *PRE*, 2001.

[85] A.S.Sonin A.V.Kaznacheev, M.M.Bogdanov. The influence of anchoring energy on the prolate shape of tactoids in lyotropic inorganic liquid crystals. *J.Exp.Theor.Phys*, 97d:1159–1167, 2003.

[86] A.Fernandez-Nieves L.F.Rull, J.M.Romero-Enrique. Computer simulations of nematic drops: Coupling between drop shape and nematic order. *J.Chem.Phys.*, 2012.

[87] J.Nguyen-N.Georgoulia-B.M.Mulder G.H.Koenderink M.Soares e Silva, J.Alvarado. Self-organized patterns of actin filaments in cell-sized confinement. *Soft Matter*, 7:10631–10641, 2011.

[88] E.Velasco D.de las Heras. Domain walls in two-dimensional nematics confined in a small circular cavity. *Soft Matter*, 10:1758–1766, 2013.

[89] J.Alvarado O.J.Dammone P.D.Howell-A.Majumdar-B.M.Mulder M.P.Lettinga-G.H.Koenderink D.G.A.L.Aarts A.H.Lewis, I.Garlea. Colloidal liquid crystals in rectangular confinement:theory and experiment. *Soft Matter*, 10:7865, 2004.

[90] R.P.A.Dullens J.M.Yeomans M.P.Lettinga-D.A.L.Aarts O.J.Dammone, I.Zacharoudiou. Confinement induced splay-to-bend transition of colloidal rods. *Phys.Rev.Lett.*, 109:108303, 2012.

[91] O.J.Dammone. *Confinement of Colloidal Liquid Crystals*. PhD thesis, University College, University of Oxford, 2013.

[92] J.R.Alvarado. *Biological Polymers: Confined, Bent, and Driven*. PhD thesis, FOM Institute, AMOLF, 2013.

[93] D.G.Grier J.C.Crocker. Methods of digital video microscopy for colloidal studies. *J.Colloid Interface Sci.*, 179:298, 1996.

[94] J.T.C.Schrauwen A.Griffa D.Sage-C.V.C.Bouten-F.N.van de Vosse M.Unser-N.Stergiopulos R.Rezakhaniha, A.Agianniotis. Experimental investigation of collagen waviness and orientation in the arterial adventitia using confocal laser scanning microscopy. *Biomechanics and Modeling in Mechanobiology*, 11(3-4):461–473, 2012.

[95] Z.Dogic. Unpublished.

[96] B.M.Mulder I.Garlea. Unpublished work.

[97] Zŭmer J.Bezi ć. Structures of the cholesteric liquid crystal droplets with parallel surface anchoring. *Liquid crystals*, 11(4):593–619, 1992.

[98] J.Watanabe T.Furukawa H.Takezoe T.Niori, T.Sekine. Distinct ferroelectric smectic liquid crystals consisting of banana shaped achiral molecules. *J.Mater.Chem.*, 6:1231–1233, 1996.

[99] D.Krueerke M.S.Heberling M.Nakata-C.D.Jones-D.Chen D.R.Link J.Zasadzinski G.Heppke-J.P.Rabe W.Stocker E.Koerblova D.M.Walba M.A.Glaser N.A.Clark L.E.Hough, H.T.Jung. Helical nanofilament phases. *Science*, 24:456–460, 2009.

[100] F.Lonberg R.B.Meyer A.J.Hurd, S.Fraden. Field-induced transient periodic structures in nematic liquid crystals : the splay frederiks transition. *J.Phys.France*, 46:905, 1985.